



HAL
open science

Modelling and simulation of gust and atmospheric turbulence effects on flexible aircraft flight dynamics

Pau Castells Marin

► **To cite this version:**

Pau Castells Marin. Modelling and simulation of gust and atmospheric turbulence effects on flexible aircraft flight dynamics. Fluid Dynamics [physics.flu-dyn]. Institut National Polytechnique de Toulouse - INPT, 2020. English. NNT : 2020INPT0061 . tel-04167434

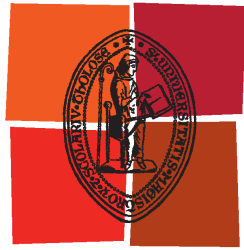
HAL Id: tel-04167434

<https://theses.hal.science/tel-04167434>

Submitted on 20 Jul 2023

HAL is a multi-disciplinary open access archive for the deposit and dissemination of scientific research documents, whether they are published or not. The documents may come from teaching and research institutions in France or abroad, or from public or private research centers.

L'archive ouverte pluridisciplinaire **HAL**, est destinée au dépôt et à la diffusion de documents scientifiques de niveau recherche, publiés ou non, émanant des établissements d'enseignement et de recherche français ou étrangers, des laboratoires publics ou privés.



Université
de Toulouse

THÈSE

En vue de l'obtention du

DOCTORAT DE L'UNIVERSITÉ DE TOULOUSE

Délivré par :

Institut National Polytechnique de Toulouse (Toulouse INP)

Discipline ou spécialité :

Dynamique des fluides

Présentée et soutenue par :

M. PAU CASTELLS MARIN

le mercredi 8 juillet 2020

Titre :

Modelling and simulation of gust and atmospheric turbulence effects on
flexible aircraft flight dynamics

Ecole doctorale :

Mécanique, Energétique, Génie civil, Procédés (MEGeP)

Unité de recherche :

Institut de Mécanique des Fluides de Toulouse (IMFT)

Directeur(s) de Thèse :

MME MARIANNA BRAZA

Rapporteurs :

M. HORIA HANGAN, WINDEE RESEARCH INSTITUTE - U. W ONTARIO

M. YANNICK HOARAU, UNIVERSITE DE STRASBOURG

Membre(s) du jury :

M. YANNICK HOARAU, UNIVERSITE DE STRASBOURG, Président

M. BENOIT CALMELS, AIRBUS FRANCE, Membre

M. GEORGE BARAKOS, UNIVERSITY OF GLASGOW, Membre

M. JOSEPH MORLIER, ISAE-SUPAERO, Membre

Mme MARIANNA BRAZA, TOULOUSE INP, Membre

M. PHILIPP BEKEMEYER, DLR Brunswick, Membre

Acknowledgements

I would like to sincerely thank everyone who has contributed and helped in different ways to achieve this work and make the experience of the last three years strongly enriching for both my personal and professional development.

I first want to thank Benoît Calmels and Jean Baptiste Leterrier for giving me the opportunity to work on this topic, having trusted me and being there when needed. I would also like to extend my sincere gratitude to Christophe Poetsch for all his advices and help along the last three years. I sincerely thank Marianna Braza for welcoming me to the IMFT, providing interesting insight on the topic and helping whenever it has been required. I must also thank Alexander Bremridge for his support during these last months.

I had the opportunity to work and learn with a lot of people from very different departments and backgrounds. I would like to thank to Giovannantonio Soru for inviting me to Hamburg and introducing me to Wolfgang Weigold, whom I also wish to sincerely thank for his interesting ideas, suggestions and technical discussions. I would also like to extend my gratitude to John Pattinson for showing me part of his work in Filton and providing valuable advices. Many thanks also to Bernd Stickan for his work, help and support. I would like to thank David Quero from the DLR for his view on the topic and meaningful advices. Part of this work would not have been possible without Stéphane Marcy, whom I am also grateful for his trust and having helped when needed. I have very much appreciated working with Andrew Chim and Anna Gebhardt. I must thank them for their work, their point of view and support on the topic. I would also like to thank Manuel Gonzalez and Luis Barrera for the interesting as well as constructive discussions and guidance. Many thanks to Thierry Duchamp, Bertrand Soucheleau and Michel Mazet for their interesting technical point of view on the topic. I would like to extend my gratitude to Xavier Bertrand and Jean-Jacques Degeilh for the support and helpful advice in different situations. I am also grateful to Florian Blanc for the insightful point of view and suggestions when necessary. Special thanks to Sebastien Blanc, Robin Vernay, Christophe Le Garrec, Veronique Blanc and Olivier Regis for providing invaluable insight into the topic and help when required as well as Luca Bagnoli and Davide Cantiani for their trust and for everything I have learnt with them. I would like to mention as well Frank Weiss, Christian Mias, Steve Champagneaux, Carole Despré-Flachard, Cyril Boureau, Bruno Marchal, Arnaud

Glin, Moriz Scharpenberg, Olaf Lindenau, Mathieu Reguerre, Jonathan Beck, Matthieu Barba, Yacine Vigourel, Myrtille Faucon, Alessandro Savarese, Emilie Pauchard, Fabien Ayme and Emmanuel Corratgé for the help, support and being available when needed.

I also want to express my gratitude to all the different colleagues from IGAAT for the nice environment and willingness to help. Working until late some evenings, in particular on Friday, would not have been the same without Johan Degriigny, Pierre Aumoite, Fred Tost, Matthieu Scherrer, Vincent Colman or Alejandro Moyano. Thanks also to Oriol Chandre Vila for having read this document and providing feedback. I also want to thank Luis Lopez de Vega for the help in different situations as well as the good moments during the experience.

Many thanks to my closest friends for being there and comprehensive even if I see some of them once in a year. Special thanks to Xavi for the necessary weekly meals together, Coline and Olmo for many invitations that allowed me to switch off and my old roommates and friends, Albert, Eli, Josep and Iván for the great moments shared together in Toulouse and back in the university.

M'agradaria agrair la meva família, els meus pares i el meu germà Oriol per haver-me donat tot el suport i ànims quan ha estat necessari.

Finalement, un grand merci à Coline pour sa patience, son soutien et son aide précieuse tout au long de cette aventure.

Abstract

The prediction of the aircraft response to gust and turbulence is of major importance for different purposes. Gust load analysis is an essential part of aircraft design and certification. The effect of gust and turbulence on aircraft flight dynamics is also of interest. Models able to capture relevant effects at these conditions in early design phases are essential in order to anticipate and assess the aircraft response and flight control laws in realistic atmospheric disturbances before flight test.

This work proposes a modelling strategy to capture relevant physics when simulating the aircraft response to gust and turbulence for flight dynamics investigations. The model provides accuracy at a low computational cost as well as consistency with gust loads analysis enabling multidisciplinary design. The approach is based on the integration of a nonlinear quasi-steady flexible flight dynamics model with an unsteady aeroelastic model linearized around a nonlinear steady state.

The gust-induced forces have a significant impact on aircraft flight dynamics. Low computing times are required to cover several flight conditions and aircraft parameters. A computationally efficient multipoint aerodynamic model, which captures both unsteady aerodynamic and gust propagation effects, is generated from linearized Computational Fluid Dynamics (CFD) simulations in the frequency domain. The model is identified through a rational function approximation allowing for time domain simulations. A reduced number of additional aerodynamic states is sufficient to capture the main effects at low frequencies for flight dynamics analysis. The impact of dynamic flexibility on the response is also evaluated. Only the most energetic flexible modes are retained to reduce the number of states and ensure a low computation time.

The approach is applied to simulate the vertical and lateral response of a passenger aircraft to theoretical disturbance profiles as well as realistic atmospheric turbulence at different flight conditions. Aerodynamic nonlinear effects, such as local stalls due to shock motion, in transonic conditions may appear. The linearized model is able to capture the global aircraft response at these conditions with low amplitude shock motions. Results are compared and validated with a CFD simulation based approach, coupled with a structural dynamics and flight mechanics solver. Measures from flight test are also used to assess the modelling approach. The effect of uncertainties on the response is analysed, in terms of the turbulence variation along the wingspan. Simulation results show that relevant aerodynamic effects due to gust and turbulence are captured in the frequency range of interest for flight dynamics investigations.

Keywords: Gust, Atmospheric Turbulence, Flight Dynamics, Handling Qualities, Aeroelasticity, Unsteady Aerodynamics, DLM, CFD

Résumé

La prédiction de la réponse de l'avion aux rafales et turbulence a un rôle primordial dans différentes applications. L'analyse des charges en rafale est un élément essentiel de la conception et certification des avions. L'effet des rafales et turbulence sur la dynamique de vol est également important. Avoir des modèles capables de capturer des effets significatifs dans ces conditions et pendant la phase initiale de conception permet d'anticiper et d'évaluer la réponse de l'avion et les lois de contrôle face à des perturbations atmosphériques réalistes avant des essais en vol.

Ce travail propose une stratégie de modélisation afin de capturer des effets physiques pertinents lors de la simulation de la réponse de l'avion face à la rafale et la turbulence pour des analyses de dynamique de vol. Le modèle apporte de la précision pour un faible coût de calcul, ainsi qu'une cohérence avec des analyses de charges en rafales permettant une conception multidisciplinaire. L'approche est basée sur l'intégration d'un modèle non-linéaire de dynamique de vol quasi-stationnaire souple et un modèle aéroélastique instationnaire linéarisé autour d'un état stationnaire non-linéaire.

Les forces induites par les rafales ont un impact significatif sur la dynamique de vol des avions. Des faibles temps de calcul sont nécessaires afin de couvrir plusieurs conditions de vol et paramètres de l'avion. Un modèle aérodynamique multipoint à faible coût de calcul, qui capture des effets instationnaires et de propagation des rafales, est généré à partir de calculs CFD linéarisés dans le domaine fréquentiel. Le modèle est identifié par une fonction rationnelle permettant des simulations dans le domaine temporel. Un nombre réduit d'états aérodynamiques supplémentaires est suffisant afin de capturer les principaux effets à basses fréquences pour les analyses de dynamique de vol. L'impact de la flexibilité dynamique sur la réponse est également évalué. Seuls les modes souples le plus énergétiques sont conservés afin de réduire le nombre d'états et d'assurer un faible temps de calcul.

L'approche est appliquée afin de simuler la réponse verticale et latérale d'un avion de passagers face à des profils de perturbation théoriques ainsi qu'à de la turbulence atmosphérique réaliste dans différentes conditions de vol. Des effets aérodynamiques nonlinéaires, tels que des décollements locaux dus aux mouvements des ondes de choc, peuvent apparaître en conditions transsoniques. Le modèle linéarisé est capable, dans ces conditions, de capturer la réponse globale de l'avion avec des mouvements des ondes de choc à faible amplitude. Les résultats sont comparés et validés avec des simulations CFD couplées à un solveur de dynamique structurelle et de mécanique de vol. Des mesures des essais en vol sont également utilisées afin d'évaluer l'approche de modélisation. L'effet des incertitudes de la variation de turbulence en envergure de l'aile sur la réponse est analysé. Les résultats de simulation montrent que des effets aérodynamiques significatifs sont capturés dans la plage de fréquence d'intérêt pour les investigations de dynamique de vol.

Mots clés : Rafales, Turbulence atmosphérique, Dynamique de vol, Qualités de vol, Aéroélasticité, Aerodynamique instationnaire, DLM, CFD

Contents

| | |
|---|-----------|
| Introduction | 1 |
| Context | 1 |
| Previous work | 3 |
| Objectives | 9 |
| Outline | 9 |
| | |
| I Theory | 11 |
| | |
| 1 Simulation and Modelling of Aircraft Dynamic Response | 13 |
| 1.1 Aerodynamic Formulation | 13 |
| 1.1.1 Reynolds Averaged Navier Stokes (RANS) Equations | 13 |
| 1.1.2 Linearized Reynolds Averaged Navier Stokes (RANS) Equations | 16 |
| 1.1.3 Doublet Lattice Method (DLM) | 20 |
| 1.2 Flight Dynamics Response | 23 |
| 1.2.1 Equations of Motion | 23 |
| 1.2.2 Quasi-steady Flexible Aerodynamic Model | 25 |
| 1.3 Aeroelastic Response | 27 |
| 1.3.1 Equations of Motion | 27 |
| 1.3.2 Unsteady Aerodynamic Model | 30 |
| 1.3.3 State-space Model | 33 |
| | |
| 2 Integrated Aircraft Model | 35 |
| 2.1 Modelling Assumptions | 35 |
| 2.2 Equations of Motion | 36 |
| 2.3 Gust-induced Effect | 38 |
| 2.3.1 Aerodynamic Derivatives | 39 |
| 2.3.2 Quasi-steady Correction | 46 |
| 2.4 Dynamic Flexibility Effect | 47 |
| 2.4.1 Residualized Model Approach | 48 |
| 2.4.2 Integrated State-space Model | 49 |

| | | |
|-----------|---|------------|
| II | Results | 51 |
| 3 | Theoretical Gust | 53 |
| 3.1 | Gust Definition | 53 |
| 3.2 | Fixed Rigid Aircraft | 54 |
| 3.3 | Free Flying Quasi-steady Flexible Aircraft | 64 |
| 3.4 | Free Flying Flexible Aircraft | 71 |
| 3.5 | Transonic Conditions | 80 |
| 4 | Atmospheric Turbulence | 93 |
| 4.1 | Theoretical Turbulence | 93 |
| 4.2 | Realistic Atmospheric Turbulence | 100 |
| 4.3 | Effect of Turbulence Variation Along the Wingspan | 102 |
| | Conclusions and perspectives | 109 |
| | Bibliography | 113 |

List of Figures

| | | |
|------|---|----|
| 1 | Illustration of the simulation of the aircraft response due to a vertical gust | 2 |
| 1.1 | CFD surface mesh | 16 |
| 1.2 | Vertical gust mode shape over the CFD mesh | 18 |
| 1.3 | DLM panel discretisation of a generic aircraft | 22 |
| 1.4 | Geodetic and body reference frames | 24 |
| 1.5 | Euler angles defining the orientation of the body frame (b) with respect to the geodetic frame (E). Intermediate axes (1, 2) are defined for the rotation sequence. | 24 |
| 1.6 | Angle of attack (α) and sideslip (β) defining the orientation of the aerodynamic reference system (a) with respect to the body frame (b). Intermediate axes (i) are defined for the rotation sequence. | 26 |
| 1.7 | Global FEM model | 28 |
| 1.8 | Condensed FEM model with structural reference frame | 28 |
| 2.1 | Integration approach between nonlinear flight dynamics and linear aeroelastic equations of motion | 38 |
| 2.2 | Illustration vertical gust effect and downwash on the aircraft | 40 |
| 2.3 | Illustration lateral gust effect and sidewash on the aircraft | 44 |
| 3.1 | Gust profiles in time domain | 53 |
| 3.2 | Gust profiles in frequency domain | 53 |
| 3.3 | GAF in lift due to vertical gust | 54 |
| 3.4 | GAF in pitch due to vertical gust | 55 |
| 3.5 | Heave, pitch and vertical gust modes at a frequency close to zero (source:[17]) | 55 |
| 3.6 | Comparison of GAF in lift due to heave motion, pitch rotation and vertical gust | 55 |
| 3.7 | Lift coefficient of fixed rigid A/C due to vertical gust (H=150ft) | 56 |
| 3.8 | Pitching moment coefficient of fixed rigid A/C due to vertical gust (H=150ft) | 56 |
| 3.9 | GAF in lift due to vertical gust | 56 |
| 3.10 | GAF in pitch due to vertical gust | 57 |
| 3.11 | GAF in roll due to lateral gust | 57 |
| 3.12 | GAF in yaw due to lateral gust | 58 |
| 3.13 | Rolling moment coefficient of fixed rigid A/C due to lateral gust (H=150ft) | 58 |

| | | |
|------|--|----|
| 3.14 | Yawing moment coefficient of fixed rigid A/C due to lateral gust (H=150ft) | 58 |
| 3.15 | GAF in lift due to vertical gust | 59 |
| 3.16 | GAF in pitch due to vertical gust | 59 |
| 3.17 | Lift coefficient of fixed rigid A/C due to vertical gust (H=300ft) | 60 |
| 3.18 | Pitching moment coefficient of fixed rigid A/C due to vertical gust (H=300ft) | 60 |
| 3.19 | GAF in roll due to lateral gust | 60 |
| 3.20 | GAF in yaw due to lateral gust | 61 |
| 3.21 | Rolling moment coefficient of fixed rigid A/C due to lateral gust (H=300ft) | 61 |
| 3.22 | Yawing moment coefficient of fixed rigid A/C due to lateral gust (H=300ft) | 61 |
| 3.23 | GAF in lift due to vertical gust | 62 |
| 3.24 | GAF in pitch due to vertical gust | 62 |
| 3.25 | Lift coefficient of fixed rigid A/C due to vertical gust (H=300ft) | 63 |
| 3.26 | Pitching moment coefficient of fixed rigid A/C due to vertical gust (H=300ft) | 63 |
| 3.27 | GAF in roll due to lateral gust | 63 |
| 3.28 | GAF in yaw due to lateral gust | 64 |
| 3.29 | Rolling moment coefficient of fixed rigid A/C due to lateral gust (H=300ft) | 64 |
| 3.30 | Yawing moment coefficient of fixed rigid A/C due to lateral gust (H=300ft) | 64 |
| 3.31 | Lift coefficient of quasi-steady flexible A/C due to vertical gust (H=300ft) | 65 |
| 3.32 | Pitching moment coefficient of quasi-steady flexible A/C due to vertical gust (H=300ft) | 65 |
| 3.33 | Lift coefficient of quasi-steady flexible A/C due to vertical gust (H=300ft) | 65 |
| 3.34 | Pitching moment coefficient of quasi-steady flexible A/C due to vertical gust (H=300ft) | 65 |
| 3.35 | Rolling moment coefficient of quasi-steady flexible A/C due to lateral gust (H=300ft) | 66 |
| 3.36 | Yawing moment coefficient of quasi-steady flexible A/C due to lateral gust (H=300ft) | 66 |
| 3.37 | Rolling moment coefficient of quasi-steady flexible A/C due to lateral gust (H=300ft) | 66 |
| 3.38 | Yawing moment coefficient of quasi-steady flexible A/C due to lateral gust (H=300ft) | 66 |
| 3.39 | Lift coefficient of quasi-steady flexible A/C due to vertical gust (H=300ft) for different CG | 67 |
| 3.40 | Pitching moment coefficient of quasi-steady flexible A/C due to vertical gust (H=300ft) for different CG | 67 |
| 3.41 | Illustration of the effect at different centre of gravity positions in vertical | 68 |
| 3.42 | Rolling moment coefficient of quasi-steady flexible A/C due to vertical gust (H=300ft) for different CG | 68 |
| 3.43 | Yawing moment coefficient of quasi-steady flexible A/C due to vertical gust (H=300ft) for different CG | 68 |

| | | |
|------|--|----|
| 3.44 | Illustration of the effect at different centre of gravity positions in lateral . | 69 |
| 3.45 | Illustration of the roll damping | 69 |
| 3.46 | Rolling moment coefficient of free flying rigid A/C due to vertical gust (H=300ft) for different wing dihedral | 70 |
| 3.47 | Yawing moment coefficient of free flying rigid A/C due to vertical gust (H=300ft) for different wing dihedral | 70 |
| 3.48 | Illustration of the dihedral effect with and without static deformation . . | 70 |
| 3.49 | Lift coefficient of free flying rigid and quasi-steady flexible A/C due to vertical gust (H=300ft) | 71 |
| 3.50 | Pitching moment coefficient of free flying rigid and quasi-steady A/C due to vertical gust (H=300ft) | 71 |
| 3.51 | Rolling moment coefficient of free flying rigid and quasi-steady flexible A/C due to lateral gust (H=300ft) | 71 |
| 3.52 | Yawing moment coefficient of free flying rigid and quasi-steady A/C due to lateral gust (H=300ft) | 71 |
| 3.53 | Lift coefficient of free flexible A/C due to vertical gust (H=300ft) | 72 |
| 3.54 | Pitching moment coefficient of free flexible A/C due to vertical gust (H=300ft) | 72 |
| 3.55 | Lift coefficient of free flexible A/C due to vertical gust (H=150ft) | 73 |
| 3.56 | Pitching moment coefficient of free flexible A/C due to vertical gust (H=150ft) | 73 |
| 3.57 | Low frequency modes which impact lift force and pitching moment coefficients (Wing and fuselage bending and symmetric engine modes with amplification factor) | 73 |
| 3.58 | Lift coefficient of free flexible A/C due to vertical gust (H=150ft) | 74 |
| 3.59 | Pitching moment coefficient of free flexible A/C due to vertical gust (H=150ft) | 74 |
| 3.60 | Rolling moment coefficient of free flexible A/C due to lateral gust (H=300ft) | 74 |
| 3.61 | Yawing moment coefficient of free flexible A/C due to lateral gust (H=300ft) | 74 |
| 3.62 | Rolling moment coefficient of free flexible A/C due to lateral gust (H=150ft) | 75 |
| 3.63 | Yawing moment coefficient of free flexible A/C due to lateral gust (H=150ft) | 75 |
| 3.64 | Low frequency modes which impact rolling and yawing moment coefficients (Wing and fuselage antisymmetric bending and engine antisymmetric modes with amplification factor) | 75 |
| 3.65 | Rolling moment coefficient of free flexible A/C due to lateral gust (H=150ft) | 76 |
| 3.66 | Yawing moment coefficient of free flexible A/C due to lateral gust (H=150ft) | 76 |
| 3.67 | Gust profiles in time domain | 76 |
| 3.68 | Gust profiles in frequency domain | 76 |
| 3.69 | Lift coefficient of quasi-steady flexible A/C due to different vertical gust profiles | 77 |
| 3.70 | Pitching moment coefficient of quasi-steady flexible A/C due to different vertical gust profiles | 77 |

| | | |
|-------|--|----|
| 3.71 | Vertical load factor of quasi-steady flexible A/C due to different vertical gust profiles | 78 |
| 3.72 | Pitch angle of quasi-steady flexible A/C due to different vertical gust profiles | 78 |
| 3.73 | Lateral load factor of quasi-steady flexible A/C due to different lateral gust profiles | 78 |
| 3.74 | Roll angle of quasi-steady flexible A/C due to different lateral gust profiles | 78 |
| 3.75 | Roll rate of quasi-steady flexible A/C due to different vertical gust profile | 79 |
| 3.76 | Yaw rate of quasi-steady flexible A/C due to different vertical gust profile | 79 |
| 3.77 | Gust profiles in time domain | 79 |
| 3.78 | Gust profiles in frequency domain | 79 |
| 3.79 | Lift coefficient of free flexible A/C due to vertical gust (H=100ft) | 80 |
| 3.80 | Pitching moment coefficient of free flexible A/C due to vertical gust (H=100ft) | 80 |
| 3.81 | Rolling moment coefficient of free flexible A/C due to lateral gust (H=100ft) | 80 |
| 3.82 | Yawing moment coefficient of free flexible A/C due to lateral gust (H=100ft) | 80 |
| 3.83 | GAF in lift due to vertical gust | 81 |
| 3.84 | GAF in pitch due to vertical gust | 81 |
| 3.85 | Lift coefficient of fixed rigid A/C due to vertical gust (H=300ft) | 82 |
| 3.86 | Pitching moment coefficient of fixed rigid A/C due to vertical gust (H=300ft) | 82 |
| 3.87 | Wing station at which the increment of pressure coefficient (ΔC_p) is calculated | 82 |
| 3.88 | Increment of C_p distribution due to a low amplitude gust profile (scaled) with respect to the steady condition at different time steps for a fixed rigid A/C (M=0.836, h=27000ft) | 83 |
| 3.89 | Increment of C_p distribution with respect to the steady condition at different time steps for a fixed rigid A/C (M=0.5, h=0ft) | 83 |
| 3.90 | Increment of C_p distribution with respect to the steady condition at different time steps for a fixed rigid A/C (M=0.836, h=27000ft) | 84 |
| 3.91 | Lift coefficient of fixed rigid A/C due to vertical gust (H=300ft) | 84 |
| 3.92 | Pitching moment coefficient of fixed rigid A/C due to vertical gust (H=300ft) | 84 |
| 3.93 | Pressure distribution when the maximum amplitude of the gust disturbance reaches the wing and zoom to the outer wing region where flow weakens | 85 |
| 3.94 | Lift force coefficient as a function of the steady angle of attack (M=0.836, h=27000ft) | 85 |
| 3.95 | Pressure distribution when the maximum amplitude of the gust disturbance reaches the wing and zoom to the outer wing region where local stall appears | 86 |
| 3.96 | Lift coefficient of fixed rigid A/C due to vertical gust (H=300ft) | 87 |
| 3.97 | Pitching moment coefficient of fixed rigid A/C due to vertical gust (H=300ft) | 87 |
| 3.98 | Lift coefficient of fixed rigid A/C due to vertical gust (H=150ft) | 87 |
| 3.99 | Pitching moment coefficient of fixed rigid A/C due to vertical gust (H=150ft) | 87 |
| 3.100 | Lift coefficient of free flexible A/C due to vertical gust (H=300ft) | 88 |

| | | |
|-------|---|-----|
| 3.101 | Pitching moment coefficient of free flexible A/C due to vertical gust (H=300ft) | 88 |
| 3.102 | Increment of Cp distribution with respect to the steady condition at different time steps for a free flexible A/C (M=0.836, h=27000ft) | 89 |
| 3.103 | Increment of Cp distribution due to a low amplitude gust profile (scaled) with respect to the steady condition at different time steps for a free flexible A/C (M=0.836, h=27000ft) | 89 |
| 3.104 | Lift coefficient of free flexible A/C due to vertical gust (H=150ft) | 89 |
| 3.105 | Pitching moment coefficient of free flexible A/C due to vertical gust (H=150ft) | 89 |
| 3.106 | GAF in lift due to vertical gust for different Mach | 90 |
| 3.107 | GAF in lift due to vertical gust for different Mach | 90 |
| 3.108 | GAF in pitch due to vertical gust for different Mach | 91 |
| 4.1 | PSD Von Karman turbulence spectrum | 94 |
| 4.2 | Continuous wind turbulence in the time domain given by the Von Karman spectrum | 94 |
| 4.3 | Pitch rate due to Von Karman turbulence spectrum (L=2500ft, $\sigma_t=3$) | 96 |
| 4.4 | PSD pitch rate due to Von Karman turbulence spectrum (L=2500ft, $\sigma_t=3$) | 96 |
| 4.5 | Vertical load factor due to Von Karman turbulence spectrum (L=2500ft, $\sigma_t=3$) | 96 |
| 4.6 | Yaw rate due to Von Karman turbulence spectrum (L=2500ft, $\sigma_t=3$) | 97 |
| 4.7 | PSD yaw rate due to Von Karman turbulence spectrum (L=2500ft, $\sigma_t=3$) | 97 |
| 4.8 | Roll rate due to Von Karman turbulence spectrum (L=2500ft, $\sigma_t=3$) | 97 |
| 4.9 | PSD Von Karman turbulence spectrum | 98 |
| 4.10 | Continuous wind turbulence in the time domain given by the Von Karman spectrum | 98 |
| 4.11 | Pitch rate due to Von Karman turbulence spectrum (L=50ft, $\sigma_t=3$) | 99 |
| 4.12 | Vertical load factor due to Von Karman turbulence spectrum (L=50ft, $\sigma_t=3$) | 99 |
| 4.13 | Roll rate due to Von Karman turbulence spectrum (L=50ft, $\sigma_t=3$) | 99 |
| 4.14 | Yaw rate due to Von Karman turbulence spectrum (L=50ft, $\sigma_t=3$) | 99 |
| 4.15 | PSD vertical measured turbulence spectrum | 100 |
| 4.16 | Vertical measured turbulence in the time domain | 100 |
| 4.17 | Pitch rate due to turbulence | 101 |
| 4.18 | PSD pitch rate due to turbulence | 101 |
| 4.19 | Vertical load factor at CG due to turbulence | 101 |
| 4.20 | Yaw rate due to turbulence | 102 |
| 4.21 | PSD yaw rate due to turbulence | 102 |
| 4.22 | Illustration of gust angular speed induced by variations along the wingspan | 103 |
| 4.23 | Gust angular speed in roll and difference of vertical load factor between both wingtips | 104 |

| | | |
|------|---|-----|
| 4.24 | Cross-power spectral density estimate between Pwind and measured roll rate | 104 |
| 4.25 | Cross-power spectral density estimate between Pwind and vertical turbulence measure | 105 |
| 4.26 | Magnitude-squared coherence estimate between Pwind and vertical turbulence measure | 105 |
| 4.27 | Cross-power spectral density estimate between Pwind and lateral turbulence measure | 105 |
| 4.28 | Magnitude-squared coherence estimate between Pwind and lateral turbulence measure | 105 |
| 4.29 | Roll rate due to turbulence | 106 |
| 4.30 | PSD roll rate due to turbulence | 106 |
| 4.31 | Yaw rate due to turbulence | 106 |
| 4.32 | PSD yaw rate due to turbulence | 106 |
| 4.33 | Vertical load factor at CG due to turbulence | 106 |
| 4.34 | Pitch rate due to turbulence | 106 |

Nomenclature

Abbreviations

| | |
|--------|---|
| A/C | Aircraft |
| AIC | Aerodynamic Influence Coefficient |
| CFD | Computational Fluid Dynamics |
| CG | Centre of Gravity |
| CSM | Computational Structural Mechanics |
| DES | Detached Eddy Simulation |
| DLM | Doublet Lattice Method |
| DLR | Deutsches Luft- und Raumfahrt Zentrum (German Aerospace Center) |
| DVA | Disturbance Velocity Approach |
| FEM | Finite Element Method |
| FM | Flight Mechanics |
| FRF | Frequency Response Function |
| GAF | Generalized Aerodynamic Force |
| GMRes | Generalized Minimal Residual |
| HTP | Horizontal Tail Plane |
| LES | Large Eddy Simulations |
| LFD | Linearized Frequency Domain |
| LIDAR | Light Detection and Ranging |
| LU-SGS | Lower-Upper Symmetric-Gauss-Seidel |
| MAC | Mean Aerodynamic Chord |
| ODE | Ordinary Differential Equation |
| PDEs | Partial Differential Equations |
| PSD | Power Spectral Density |
| RANS | Reynolds Averaged Navier Stokes |
| RBF | Radial Basis Function |
| RFA | Rational Function Approximation |
| ROM | Reduced Order Model |
| VTP | Vertical Tail Plane |
| VLM | Vortex Lattice Method |

Greek Symbols

| | |
|---------------|---|
| α | Angle of attack |
| α_G | Angle of attack due to a vertical gust or turbulence disturbance |
| β | Sideslip |
| β_G | Sideslip due to a lateral gust or turbulence disturbance |
| γ | Heat capacity ratio |
| δ | Finite-difference step size |
| Δ | Increment |
| ε | Downwash |
| θ | Pitch attitude angle |
| Θ | Euler angles |
| λ | Gust wavelength |
| ν | Mesh cell volumes in a matrix |
| ρ | Airflow density |
| σ | Sidewash |
| σ_t | Root-mean-square turbulence velocity |
| σ_y | Root-mean-square value of the aircraft response to turbulence |
| τ | Viscous stress tensor |
| τ_G | Time constant of a first order filter associated with the gust-induced effect |
| $\tau_{n/w}$ | Time delay from the aircraft nose section to the aerodynamic centre of the wing |
| $\tau_{n/H}$ | Time delay from the aircraft nose section to the HTP |
| $\tau_{w/H}$ | Time delay from the aerodynamic centre of the wing to the HTP |
| $\tau_{w/V}$ | Time delay from the aerodynamic centre of the wing to the VTP |
| φ | Gust phase shift |
| ϕ | Roll attitude angle |
| ϕ_p | Total velocity potential |
| ϕ_k | Power spectral density of the Von Karman turbulence velocity profile |
| ϕ_v | Perturbation velocity potential |
| ϕ_y | Power spectral density of the aircraft response to turbulence |
| ϕ_{xz} | Cross power spectral density between measures x and z |
| Φ | Modal matrix |
| ψ | Heading angle |
| Ψ | Acceleration potential |
| ω | Angular frequency |
| Ω | Spatial frequency |
| Ω_b | Angular velocity (body axes) |

Latin Symbols

| | |
|--------------|---------------------------|
| a_∞ | Freestream speed of sound |
| \mathbf{B} | Damping matrix |
| b | Aircraft wingspan |

| | |
|--|--|
| C_l | Rolling moment coefficient |
| $C_{l\beta}$ | Rolling moment gradient due to a sideslip variation |
| $C_{l\dot{\beta}_G}$ | Dynamic rolling moment gradient due to lateral atmospheric disturbance |
| C_{lp} | Rolling moment gradient due to a roll rate variation |
| C_{lpwind} | Rolling moment gradient due to gust or turbulence variation along wingspan |
| C_m | Pitching moment coefficient |
| $C_{m\alpha}$ | Pitching moment gradient due to an angle of attack variation |
| $C_{m\dot{\alpha}_G}$ | Dynamic pitching moment gradient due to vertical atmospheric disturbance |
| C_n | Yawing moment coefficient |
| $C_{n\beta}$ | Yawing moment gradient due to a sideslip variation |
| $C_{n\dot{\beta}_G}$ | Dynamic yawing moment gradient due to lateral atmospheric disturbance |
| C_p | Pressure coefficient |
| C_x | Drag coefficient |
| C_y | Side-force coefficient |
| $C_{y\beta}$ | Side-force gradient due to a sideslip variation |
| $C_{y\dot{\beta}_G}$ | Dynamic side-force gradient due to lateral atmospheric disturbance |
| C_z | Lift force coefficient |
| $C_{z\alpha}$ | Lift force gradient due to an angle of attack variation |
| $C_{z\dot{\alpha}_G}$ | Dynamic lift force gradient due to vertical atmospheric disturbance |
| C_{xz} | Coherence between measures x and z |
| \mathbf{D} | Transformation matrix relating body and Euler angular rates |
| \mathbf{d} | Viscous fluxes |
| d_i | Delay coefficients of the rational function approximation |
| E | Energy per unit volume |
| \mathbf{F}_b | External (aerodynamic) forces (body axes) |
| \mathbf{F}_g | Forces applied to the structural grid |
| \mathbf{F}_h | Modal forces |
| $\mathbf{F}_i, \mathbf{F}_{hhi}, \mathbf{F}_{hGi}$ | Coefficients of the rational function approximation |
| \mathbf{f} | Inviscid fluxes |
| f | Frequency |
| \mathbf{G}_E | Gravitational vector (geodetic axes) |
| \mathbf{G}_{gj} | Spline to project forces from aerodynamic to structural grid |
| g | Gravity |
| H | Half of the gust wavelength |
| H_y | Aircraft frequency response in turbulence |
| h | Altitude |
| \mathbf{I} | Identity matrix |
| \mathbf{J}_b | Total inertia tensor |
| j | Complex imaginary unit ($\sqrt{-1}$) |
| \mathbf{K} | Stiffness matrix |

| | |
|------------------------|---|
| k | Reduced frequency |
| L | Turbulence scale wavelength |
| \mathbf{L}_E | Position vector of aircraft centre of gravity in geodetic reference frame |
| l_{ref} | Reference chord length |
| $l_{n/w}$ | Distance from the aircraft nose section to the aerodynamic centre of the wing |
| $l_{n/H}$ | Distance from the aircraft nose section to the HTP |
| $l_{w/H}$ | Distance from the aerodynamic centre of the wing to the HTP |
| $l_{w/V}$ | Distance from the aerodynamic centre of the wing to the VTP |
| \mathbf{M} | Mass matrix |
| M | Mach number |
| \mathbf{M}_b | External (aerodynamic) moments (body axes) |
| m | Total aircraft mass |
| N_d | Number of delay coefficients of the rational function approximaton |
| N_y | Lateral load factor |
| N_z | Vertical load factor |
| P | Pressure |
| P_{wind} | Gust angular speed (roll) |
| p | Roll rate |
| Q | Aerodynamic influence coefficient |
| \mathbf{Q}_{hh} | Motion-induced generalized aerodynamic force |
| \mathbf{Q}_{hG} | Gust-induced generalized aerodynamic force |
| q | Power exchanged by conduction |
| q | Pitch rate |
| \bar{q} | Dynamic pressure |
| \mathbf{R} | Non-linear fluid residual |
| r | Yaw rate |
| $\mathbf{r}_{CG-25\%}$ | Position vector between aircraft CG and origin of aerodynamic reference frame |
| s | Laplace variable |
| S_{ref} | Reference area (wing surface) |
| S_H | HTP surface |
| S_V | VTP surface |
| \mathbf{T}_{bE} | Transformation matrix from geodetic frame to body axis |
| \mathbf{T}_{ba} | Transformation matrix from aerodynamic frame to body axis |
| t | Time |
| \mathbf{U} | Model inputs (state-space model) |
| u_b | x-component of velocity of aircraft centre of gravity in body axes |
| \mathbf{u}_h | Generalized coordinate |
| \mathbf{u}_e | Flexible generalized displacement |
| \mathbf{u}_{e0} | Quasi-static flexible generalized displacement |
| \mathbf{u}_r | Rigid body generalized displacement |

| | |
|----------------|--|
| V_∞ | Freestream true airspeed |
| V_H | True airspeed at HTP aerodynamic centre |
| V_V | True airspeed at VTP aerodynamic centre |
| \mathbf{V}_b | Translational velocity (body axes) |
| \mathbf{v} | Flow velocity |
| v_b | y-component of velocity of aircraft centre of gravity in body axes |
| w_b | z-component of velocity of aircraft centre of gravity in body axes |
| \mathbf{w}_G | Gust or turbulence disturbance |
| w_{yG} | Lateral component of gust or turbulence disturbance |
| w_{zG} | Vertical component of gust or turbulence disturbance |
| \mathbf{X} | Aircraft states (state-space model) |
| \mathbf{x} | Spatial position |
| \mathbf{x}_r | Rigid aircraft states (state-space model) |
| \mathbf{x}_e | Flexible aircraft states (state-space model) |
| \mathbf{x}_L | States associated with delays due to gust or turbulence inputs (state-space model) |
| x_{cg} | x-component of aircraft centre of gravity |
| \mathbf{x}_g | Structural displacement |
| \mathbf{Y} | Model outputs (state-space model) |
| \mathbf{y}_f | Conservative flow variable |

Operators

| | |
|-----------------------------------|--|
| \times | Vector cross product |
| $()^T$ | Transpose |
| $()^{-1}$ | Inverse |
| $\frac{\partial ()}{\partial ()}$ | Partial derivative |
| $\frac{d ()}{d ()}$ | Total derivative |
| $\dot{()}$ | Time derivative ($\frac{\partial ()}{\partial t}$) |
| $\nabla \cdot ()$ | Divergence |
| $\nabla ()$ | Gradient |
| $\overline{()}$ | Complex conjugate |
| $\ ()\ $ | Vector norm |
| $ () $ | Absolute value |

Subscripts

| | |
|-----|-----------------------------|
| 0 | Initial value |
| a | Aerodynamic reference frame |
| b | Body reference frame |
| E | Geodetic reference frame |
| e | Elastic degrees of freedom |
| f | Fluid |
| G | Gust |

| | |
|----------|------------------------------|
| <i>g</i> | Structural coordinates |
| <i>H</i> | HTP |
| <i>h</i> | Modal coordinates |
| <i>j</i> | Aerodynamic grid/coordinates |
| <i>L</i> | Lag states |
| <i>n</i> | Aircraft nose |
| <i>r</i> | Rigid degrees of freedom |
| <i>s</i> | Steady state |
| <i>V</i> | VTP |
| <i>w</i> | Wing |

Superscripts

| | |
|-------------|-----------------------------------|
| <i>cs</i> | Control surface deflection effect |
| <i>flex</i> | Dynamic flexibility effect |
| <i>gust</i> | Gust-induced effect |
| <i>QS</i> | Quasi-steady, quasi-static |
| <i>u</i> | Motion-induced effect |
| <i>uns</i> | Unsteady |

Introduction

Context

Gust and atmospheric turbulence, which can be seen as sudden movement of the air around the aircraft, have been considered from the earliest days of aviation in order to ensure successful flights [1, 2]. These changes in air velocity modify the effective incidence seen by the body surfaces, creating aerodynamic forces and moments which cause a dynamic response of the aircraft. This response may involve different rigid as well as flexible motion according to the atmospheric disturbance, creating internal loads in addition to trajectory and attitude variations of the vehicle that need to be considered in different aircraft analysis and design tasks.

The simulation of the aircraft response in such cases is a multidisciplinary problem relevant for different applications. Aircraft design and certification require gust load analysis in order to ensure that the airframe is able to withstand the internal loads due to gust and turbulence [3, 4]. This defines the structural sizing and as a result, the aircraft weight. Uncertainties related to the model used for the loads calculation are translated into design margins.

The effect of gust and turbulence on aircraft flight dynamics is also of interest to evaluate the aircraft response and flight control laws in realistic atmospheric disturbances. Flight tests analysis is an important part of this kind of analysis. Possible flight control law tuning from the initial design also relies on flight test. Modelling improvements before the flight test phase could enable cost and lead time reduction. Enhanced simulation means could also allow the possibility to propose strategies to attenuate the gust and turbulence effects on the aircraft response.

For different purposes, gust loads as well as flight dynamic analysis require accurate means able to predict the aircraft response in these conditions in early design phases. Within this context, understanding and modelling the relevant physics involved leading to accurate simulations is essential.

Gust loads and flight dynamics applications require low computing times as several flight conditions and aircraft parameters are evaluated. Different aerodynamic simulation

approaches with different levels of fidelity can be used to generate computationally efficient unsteady aerodynamic models used to capture the gust and turbulence induced effects.

Appart from considering the atmospheric contribution, the aircraft rigid and flexible motion create additional aerodynamic forces and moments. An example of the simulation of the aircraft response due to a vertical gust is shown in figure 1. The aircraft before the gust encounter is also included. The wing flexible deformation modifies the angle of attack in addition to the variation created by the external gust profile, changing the lift force and affecting the overall aircraft response. These effects are also of importance when simulating the aircraft response in these cases.

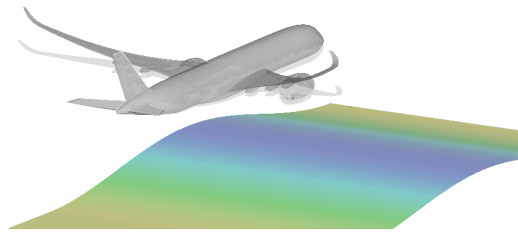


Figure 1: Illustration of the simulation of the aircraft response due to a vertical gust

The aircraft response can be simulated with different approaches covering the needs for specific applications. Models of different nature are traditionally used for flight dynamics and gust loads calculations.

Flight dynamics analysis are based on nonlinear time domain simulations with a corrected aerodynamic model to account for flexible deformation, assuming that the structure is in static equilibrium [5]. Dynamic effects due to rapid changes in rigid motion, flexible deformation or external aerodynamics are not taken into account and perturbations have an instantaneous effect on the aerodynamic forces. This assumption is referred to as quasi-steady aerodynamics and is sufficient to capture the main effects of slow manoeuvres of current aircraft passenger configurations. Nonlinear aerodynamic effects such as stalls as well as compressible effects appearing at high Mach numbers are included in the model. As the interest in flight dynamics is the study of the global aircraft response, aerodynamic forces and moments can be calculated though global aerodynamic coefficients with respect to a reference point, such as the aerodynamic centre. Different local and component effects are superposed and considered with respect to the reference point. The gust and turbulence profiles affect locally the aircraft parts at different times, due to the atmospheric disturbance propagation at a certain speed all along the vehicle.

Gust loads require the use of aeroelastic models to calculate the dynamic response [2]. This approach combine a structural model and a linear unsteady aerodynamics model usually expressed in the frequency domain. The aerodynamic forces are distributed all along the aircraft enabling local analysis for the structural sizing of the different components.

Dynamic effects due to motion and external disturbances are taken into account. Corrections are required to extend the range of validity of the linear aerodynamic model, in particular at transonic speeds close to cruise, where aerodynamic nonlinear effects appear.

Integration of methods and data from both approaches are of interest for multidisciplinary analysis, consistency between domains and overcome some of the limitations of each strategy. These kind of integration approaches are explored and proposed in this work in the framework of the simulation of the flexible aircraft response to gust and turbulence for flight dynamics investigations. The overall aircraft response also affects the calculated gust loads used to size the structure. Improved means to predict the global aircraft response could lead to more accurate gust loads. Local analysis which are not considered in the present work, are required to capture the level of loads in all the different structural components (shear force, bending and torsional moments).

Previous work

Extensive research has been previously focused on the simulation and modelling of the gust and turbulence effects on the aircraft response as well as the development of integrated flight dynamics and aeroelastic models. This section includes previous work on both topics contributing to the possibility to simulate the free flying flexible aircraft response due to gust and turbulence.

Gust and Atmospheric Turbulence Effects

Many possibilities for modelling unsteady aerodynamic effects are proposed in the literature. The traditional approach used during the last decades for gust loads analysis consist in calculating the gust and turbulence induced unsteady aerodynamic forces through potential flow equations over a range of frequencies with panel methods such as the Doublet Lattice Method (DLM), which captures unsteady effects without taking into account the steady state condition [6]. Corrections with wind tunnel and steady Computational Fluid Dynamics (CFD) data have been used to overcome limitations of panel methods, in particular in the transonic regime [7].

Other possibilities in early design phases can be considered as studied by Kier [8]. Different simulation methods with different modelling assumptions are compared by predicting the estimated gust loads in the time domain. Predictions from DLM are compared with quasi-steady Vortex Lattice Method (VLM), the steady strip theory and the unsteady strip theory with the Wagner and Küssner indicial functions [2]. The effect of gust propagation as well as the lags associated with the unsteady aerodynamic response are observed when evaluating the differences between the approaches. Recommendations are provided for preliminary gust loads design objectives.

Some advantages of a 3D panel method in comparison to DLM are shown by Kier [9] for lateral gust loads and flight dynamic analysis in early design phases. In particular, the 3D panel method is able to capture relevant flight dynamic effects such as the roll-yaw coupling which affects the flight mechanical modes like the dutch roll. These effects are not taken into account by DLM as in plane aerodynamic effects are not considered. DLM requires corrections to include some of the neglected physics. A 3D panel method is also used by Staveren [10] to identify gust stability derivatives to simulate one-dimensional (1D) and two-dimensional (2D) turbulence inputs. The method is used to calculate both the quasi-steady and unsteady stability derivatives using harmonic analysis from the aircraft frequency response functions. The identified gust derivatives are then dependent of the gust scale length and aircraft mass. The approach is compared with some analytical single-point and multi-point aircraft models presented in [11].

Some of the modelling limitations of panel methods have been pointed out by using higher fidelity simulation means, such as CFD, in particular at transonic conditions. High fidelity methods can be used to correct panel methods or to directly calculate the gust induced effect. The application of nonlinear CFD in the time domain to simulate the aircraft response of a flexible aircraft due to gust encounters is compared with classical DLM by Reimer et al. [12]. The multidisciplinary coupling framework of a CFD based approach is presented to account for flight dynamics and structural deformation. However, gust loads analysis as well as flight dynamics investigations require the simulation of a large number of cases with several parameter variations. The use of nonlinear CFD for unsteady purposes in the time domain involves large computation times.

Instead of solving nonlinear CFD directly in the time domain, recent developments have shown the possibility to obtain accurate aerodynamic predictions in the transonic regime with a low computational cost through linearized frequency-domain (LFD) methods. This approach, also known as time-linearized or linear harmonic small disturbance method, offer a large computational efficiency improvement while maintaining the accuracy of non-linear CFD. The governing equations are linearized around a non-linear steady state assuming low amplitude harmonic disturbances. This allows retaining the aerodynamic steady non-linearities such as shock waves as well as shock-induced local separation. The approach is proposed and validated by Thormann and Widhalm [13] in order to predict forced-motion unsteady aerodynamic effects and determine the flutter boundaries at high Mach numbers. Widhalm et al. [14] also propose a linearized approach as an appropriate strategy to cover wide parameter variations in a reasonable computational cost to extract dynamic stability derivatives. Both subsonic and transonic conditions are evaluated and results are validated against experimental data as well as time accurate unsteady CFD simulations.

The extension of the linearized CFD approach to solve unsteady aerodynamic effects due to gust encounters is presented by Bekemeyer and Timme [15]. Aerodynamic responses of an airfoil due to different gust profiles are obtained by superposing several frequency domain results at subsonic and transonic flight conditions. The maturity of the method is

demonstrated by Bekemeyer et al. [16] by efficiently computing the aerodynamic response to gust for a three dimensional relevant industrial case. Responses in the time domain are obtained by using a complex-valued weighting function in combination with the superposition of responses at discrete frequencies. Global lift as well as surface pressure distributions are calculated for a large civil aircraft and validated against nonlinear CFD in the time domain. The progress achieved in linearized CFD allowed the possibility to use unsteady CFD in an industrial context for gust loads calculations as shown by Weigold et al. [17]. This enables the possibility to avoid or minimise the adjustments required for panel methods. Advantages of using linearized CFD in the design of a gust loads alleviation at transonic conditions are also shown by Bekemeyer et al. [18].

The gust low amplitude assumption is not always respected and dynamic non linear effects that are not captured by linearized CFD may appear. Corrections to account for unsteady nonlinear effects at low frequencies have been recently investigated by Thormann and Timme [19]. The harmonic balance method is employed by using a small number of harmonics to correct the low frequency range while using the linearized frequency domain CFD at higher frequencies. Different gust encounters are considered to calculate the aerodynamic and aeroelastic response of an airfoil at transonic conditions.

Other strategies have been investigated to better account for nonlinear unsteady aerodynamic effects through the form of a CFD-based Reduced Order Model (ROM). This topic has been widely investigated in order to provide modelling strategies in the nonlinear aerodynamic region for many applications. An overview of nonlinear ROM applied to aerodynamics and aeroelasticity is given by Ripepi [20]. Some approaches have been proposed to deal with the specific problem of the nonlinear aerodynamic response of an aircraft to gust and turbulence. Quero et al. [21] present a ROM in the frequency domain based on the identification of Volterra kernels by continuous time impulses to predict the nonlinear aerodynamic response to gust and turbulence encounters. Bekemeyer et al. [22] propose another unsteady nonlinear ROM for gust load predictions based on least-squares residual minimization of the full order model projected in a reduced space. More accurate predictions are shown with respect to a linearized CFD approach once unsteady aerodynamic nonlinearities appear.

Unsteady aerodynamic forces calculated by linearized CFD or DLM are expressed in the frequency domain. Forces can be obtained in the time domain by different approaches. One of the possibilities consists in fitting the frequency data with rational functions in the time domain through the Rational Function Approximation (RFA) method proposed by Roger [23]. The method captures the unsteady effects in the time domain by introducing additional aerodynamic states, also referred to as lag states. This method has been widely used for various aeroservoelastic applications. Different forms have been proposed in order to keep the minimum number of additional lag states, such as the minimum state-method developed by Karpel [24].

Googin [25] proposes an aeroservoelastic method for manoeuvre and gust loads calculations in the time domain. An alternative RFA approach is applied, by adding explicit delays to the classic form proposed by Roger [23]. These delays can be associated with different parts of the aircraft, such as the nose, the wing and the tail. Compared to the classic RFA approximation, the RFA with explicit delays requires less additional lag states and is found to be more accurate at higher frequencies and predicting local gust loads in the rear part of the aircraft, where gust propagation effects are important. Weighting factors are proposed to correct the RFA to account for experimental data or quasi-steady aerodynamic nonlinearities.

Different frequency and time domain approaches to simulate the dynamic aircraft response to atmospheric gust excitations are presented by Karpel et al. [26]. The possibility to divide the aircraft in zones is also proposed to increase the accuracy of the RFA. These time delays can also be approximated by delay filters of different order in cases the use of explicit delays for each zone is not possible.

Kier and Looye [27] deal with the problematic of approximating the phase shift associated with the gust propagation effect. In the frequency domain, the time lags associated with the gust effect all along the aircraft are expressed as phase shifts with an exponential function, which can be difficult to capture in the time domain. Instead of approximating the gust column in the time domain, the proposed approach consists of expressing the gust downwash as a function of time thanks to the relative location between the aircraft and the gust through the propagation speed. A RFA with distributed coefficients over the aircraft is calculated in order to evaluate the aerodynamic effect of the downwash associated with the gust velocity as a function of time. The same approach, dividing the aircraft in five sections, is applied to the design of a gust load alleviation function by Giessler et al. [28].

Quero et al. [29] proposed an alternative to the classical Roger approximation [23] for cases in which gust-induced forces are required at higher frequencies, such as for gust loads analysis in the time domain. The approach is based on tangential interpolation and provides a minimal order approximation, avoiding any selection of lag states.

Integrated Aircraft Model

Once the aerodynamic forces and moments due to the atmospheric disturbance are calculated, the equations of motion are used to predict the aircraft response to these forces. The integration of flight dynamics and aeroelastic equations of motion offers the possibility to account for both rigid and flexible motion. The definition and formulation of these kind of integrated approaches have been addressed by several authors.

A derivation of these equations of motion from first principles using the Lagrange's equations and the principle of virtual work was proposed by Waszak and Schmidt [30, 31]. Aerodynamic generalized forces are obtained through strip theory in a closed form integral

expression. The reference axes are appropriately chosen in order to minimise the inertial coupling between rigid and flexible motion, through the concept of mean axes reference frame. The use of free vibration modes to express the flexible motion automatically fulfils the practical mean axes constraints of the reference frame minimising the inertial coupling. Additional inertial coupling terms are neglected. The nonlinear equations of motion of the integrated model describe the aircraft motion relative to body axes and the elastic deformation of the airframe relative to this reference frame. These differential equations for flight mechanics and aeroelastic motion are only coupled through the external aerodynamic forces. The same equations are obtained by Etkin [5] when adding the aerodynamic coupling terms due to the flexible degrees of freedom to the flight dynamics equations of motion.

The inertial coupling effects in the equations of motion of a free flying flexible aircraft are studied by Buttrill et al. [32]. The formulations and assumptions of the integrated equations of motion from Waszak [30, 31] and Buttrill [32] are compared in [33], providing possible simplifications as well as recommendations concerning the importance of the inertial coupling terms. Inertial coupling between the rigid and flexible degrees of freedom is taken into account in the derivation of the equations of motion done by Reschke [34] for a generic current passenger aircraft configuration. The effects on the flight dynamic states of considering an inertially coupled formulation are found to be small. An important effect of the inertial coupling is detected in structural components with large concentrated masses, such as the engines. The influence of inertial coupling on loads is found to be relevant at flight conditions with high angular rates or accelerations.

Various simulation environments are proposed to implement different integration strategies between models. One of the possibilities is VarLoads presented by Hofstee et al. [35] proposed for specific investigations from preliminary design to the analysis of in-flight events. The modular software structure of the environment allows the possibility to implement different models from various disciplines. The nonlinear equations of motion developed by Waszak and Schmidt [31] are implemented.

Apart from the equations of motion, an integrated approach between flight dynamics and aeroelastic responses needs to address the combination between different aerodynamic models dealing with different assumptions and data sources.

Rigid nonlinear quasi-steady aerodynamics are combined with an unsteady aerodynamic model from DLM in the work done by Gupta et al. [36]. A padé approximation similar to the RFA from Roger [23] is employed to express the unsteady aerodynamic forces in the time domain. The rigid quasi-steady contribution is removed from the unsteady forces.

When the quasi-steady aerodynamics model is corrected to account for quasi-static flexible effects, some aspects need to be considered when integrating both aerodynamic models. The work presented by Winther et al. [37] deals with this problematic and proposes a method to combine dynamic effects from the aeroelastic equations of motion with the

nonlinear quasi-steady flexible equations used for flight dynamics analysis. It is assumed that the rigid body dynamics of the residualized linear aeroelastic model are equivalent to the linearized flight dynamics model including quasi-static flexible corrections. The integrated model aims for real-time simulations and recommendations are given to keep low computational times. The approach, referred to as Residualized Model, is extended in the work proposed by Looye [38], providing the possibility to use aeroelastic models with unsteady aerodynamic lag states.

Another strategy presented by König and Schuler [39] proposes adding the states of a linearized or nonlinear flight dynamics equations of motion in an aeroelastic model. A modal analysis is employed to decouple rigid and flexible motion. The rigid body modes of the aeroelastic model need to be identified and are replaced by the states of the linearized or nonlinear flight dynamics equations of motion. It is assumed that the flight dynamic states are equivalent to a linear combination of rigid body modes of the aeroelastic model. The strategy is applied in the design of a controller through multi-objective parameter optimization for flight control, loads reduction and structural mode control. The integration of a linearized flight dynamics and aeroelastic model without coupling terms is also applied to different multi-objective control design techniques in the work presented by Puyou [40].

The work done by Reschke and Looye [41] compares the König and Schuler approach [39] and the Residualized Model method proposed by Looye [38]. The different assumptions, some pre-processing and implementation details as well as advantages of each approach are included. Both methods are based on the idea of keeping the flight dynamics model unchanged. Results obtained as well as computational times are found to be similar for both approaches. Recommendations to choose between them are based on the simulation environment.

Another possibility to integrate nonlinear quasi-steady aerodynamics with linear unsteady aerodynamics is proposed by Kier and Looye [27]. A set of nonlinear equations of motion as developed in [30, 31] are used. The quasi-steady aerodynamic effects are modelled through VLM. Unsteady aerodynamics are considered through a RFA of results from DLM according to Roger's method [23] for time domain simulations. Instead of projecting the aerodynamic forces to modal coordinates (generalized forces) before the approximation, the RFA is done in physical coordinates directly in the aerodynamic grid. This enables a clear separation between quasi-steady and unsteady terms which may come from different models. This has also the advantage that the approximation is only dependent on the Mach number and is not tied to a mass case like the modal unsteady aerodynamic forces.

Different applications can be found in literature. Teufel et al. [42] applies an integrated flight mechanics and aeroelastic model to predict the dynamic response of a large passenger aircraft to multidimensional gusts. These integration approaches have also been applied both for loads analysis [27] as well as for specific flight control law design strategies [28, 38].

Objectives

The main goal of the PhD is to propose a modelling approach able to capture relevant aerodynamic effects due to gust and turbulence in the frequency range of interest for flight dynamics investigations. The strategy is intended to capture relevant physics when simulating the gust and turbulence effect on flight dynamics, providing more accuracy in the predictions and minimising the increase of computational cost.

The topic requires an understanding of the main physics involved in order to propose appropriate models to capture the relevant effects. A strategy to generate the required data for the model, covering different parameters in a reasonable computation time, is also needed within an industrial context. Validation means and recommendations on the application of the proposed models are also necessary. One of the challenges when dealing with experimental data from flight test is the level of uncertainty of the gust or turbulence inputs encountered in flight.

Enhanced simulation means to capture the aircraft response in such conditions and keeping consistency between gust loads as well as flight dynamics analysis is of interest for multidisciplinary analysis in early design phases, which is essential for future aircraft developments. Specific aspects concerning flight dynamics analysis need to be addressed, such as the possibility to provide simulation means that could be integrated in the existing real-time simulation environments in the form of aerodynamic stability derivatives. The possibility to account for the effect of flight control laws in the time domain is also required for meaningful flight dynamics investigations.

Outline

In this PhD, and based on some of the previous work concerning the topic, an integrated approach including gust and turbulence induced effects is formulated and applied to simulate the free flying flexible aircraft response due to different atmospheric disturbances.

In part I, the theoretical aspects of different simulation methods and models are detailed and proposed in order to predict the aircraft dynamic response due to gust and turbulence.

The first chapter presents the aerodynamic formulation from higher to lower fidelity methods with its assumptions. The unsteady aerodynamic data is generated with CFD through its linearized form to cover a wide variation of parameters, such as the Mach number, keeping a reasonable computational time and avoiding corrections as the ones required to overcome the neglected physics of DLM. Nonlinear CFD in the time domain is also considered to validate the modelling approach and quantify the effect of possible aerodynamic nonlinearities in the global aircraft response. The remaining sections of this chapter deal with the means to predict the flight dynamics and aeroelastic response. The

equations of motion and aerodynamic models are described for each approach and details concerning the different modelling strategies are given.

The second chapter describes the integration framework to combine flight dynamics and aeroelastic models as well as how the gust-induced and dynamic flexible effects are considered. Some strategies to reduce the number of additional aerodynamic states, associated with the gust-induced effect, are shown. As flight dynamics investigations are focused on the low frequency range, accurate predictions can be obtained by keeping a low number of additional aerodynamic states in a rational function approximation. The analytical derivation of gust aerodynamic derivative coefficients for both vertical and lateral analysis is included as a possible mean to estimate the effect. Considering inertial coupling between rigid and flexible motion can provide more accuracy for specific load calculations but the effect on flight dynamics of current passenger aircraft configurations can be neglected. In this work, the external coupling through the aerodynamic forces is considered. Motion-induced unsteady aerodynamics from the flexible response are taken into account to assess the impact of dynamic flexibility on aircraft flight dynamics for current passenger aircraft configurations. Different forms of the residualized model approach are presented in order to account for the dynamic flexible effect.

In part II, the integrated approach is applied to simulate the aircraft response to gust and atmospheric turbulence. The theoretical inputs are assumed to be known and taken from the certification requirements [3]. Turbulence measured in flight is also considered as input for the simulation. Assumptions and uncertainties related to this measure are important and need to be taken into account for appropriate analysis. The analysis is done for both vertical and lateral atmospheric disturbances with different approaches and modelling assumptions detailed in the previous section. As the work is focused on the effect of gust and turbulence on flight dynamics, the variables of interest predicted and analysed through the different modelling strategies are aerodynamic global coefficients or quantities such as load factors at the centre of gravity as well as angular rates (roll, pitch, yaw). A generic current passenger aircraft configuration is used to evaluate the different simulation methods.

The third chapter focuses on the aircraft response to theoretical gust profiles at different flight conditions. Once the model is created and validated, some of the relevant physics as well as modelling assumptions are assessed. The predicted response to gust at transonic conditions is also evaluated in order to quantify the effect of possible shock motion or local stalls on the global response.

The fourth chapter focuses on the application of the approach to simulate the aircraft response due to theoretical as well as realistic atmospheric turbulence. Flight test measures are used to compare with simulation results. The effect of turbulence variations along the wingspan is discussed at the end of the chapter.

Finally, conclusions and some recommendations for future work are given.

Part I
Theory

Chapter 1

Simulation and Modelling of Aircraft Dynamic Response

In this chapter, various aerodynamic formulations with different modelling assumptions are presented. The equations of motion used to calculate the aircraft response as well as the form of the models providing the aerodynamic forces and moments are detailed. The described approaches cover both flight dynamics and aeroelastic responses.

1.1 Aerodynamic Formulation

Aerodynamics simulation and modelling is an extensive domain. Different strategies can be applied covering the needs of specific applications. Simulation means from higher to lower fidelity with its underlying assumptions and modelling strategies are shown in this section. From the Navier-Stokes equations to solve the aerodynamic problem in the time domain, to the linearisation of the equations to solve it in the frequency domain as well as the traditional potential methods used for unsteady aerodynamic computations. The predicted aerodynamics from simulation means can be adjusted with experimental data such as wind tunnel or flight tests in order to extend the validity of the model within the flight envelope.

1.1.1 Reynolds Averaged Navier Stokes (RANS) Equations

The Navier-Stokes equations is the common approach used to capture the flow phenomena around the aircraft. The equations force the conservation of mass, energy and momentum by imposing the continuity equation, Newton's second law of motion and the first law of thermodynamics. Additional empirical relations to define the fluid properties such as viscosity and thermal conductivity as well as a constitutive law are added to the system

of equations. Even if an important progress has been recently done in terms of computational resources, the Navier-Stokes equations are not suitable when dealing with relevant industrial problems. The adopted solution consists of using the Reynolds Averaged Navier Stokes (RANS) equations, in which the characteristic turbulent flow variations are averaged and a turbulence model is used to approximate the additional turbulent variations. The flow variables are then expressed as a time-average and a turbulent variation around the average condition.

According to the formulation employed by Ripepi and Quero [20, 43], the governing equations for a compressible, viscous and conductive fluid with constant properties in conservative form are:

$$\frac{\partial \mathbf{y}_f}{\partial t} + \nabla \cdot \mathbf{f}(\mathbf{y}_f) = \nabla \cdot \mathbf{d}(\mathbf{y}_f) \quad (1.1)$$

Being \mathbf{y}_f the conservative flow variable vector which depends both on the spatial position (\mathbf{x}) and time (t), the inviscid fluxes \mathbf{f} and viscous fluxes \mathbf{d} , defined respectively as:

$$\mathbf{y}_f = \begin{bmatrix} \rho \\ \rho \mathbf{v} \\ E \end{bmatrix}$$

$$\mathbf{f} = \begin{bmatrix} \rho \mathbf{v} \\ \rho \mathbf{v} \times \mathbf{v} + P \mathbf{I} \\ \mathbf{v}(E + P) \end{bmatrix}$$

$$\mathbf{d} = \begin{bmatrix} 0 \\ \tau \\ \tau \cdot \mathbf{v} + \mathbf{q} \end{bmatrix}$$

With $\rho(\mathbf{x}, t)$ being the density, $\mathbf{v}(\mathbf{x}, t)$ the flow velocity, E the energy per unit volume, $P(\mathbf{x}, t)$ the pressure, $\tau(\mathbf{x}, t)$ the viscous stress tensor, $\mathbf{q}(\mathbf{x}, t)$ the power exchanged by conduction and \mathbf{I} the identity matrix. The state equation for the pressure as well as the constitutive equations for the viscous stress tensor and the power exchanged by conduction lead to the closure of the problem. The resulting nonlinear Partial Differential Equations (PDEs) is solved by specifying the boundary and initial conditions of the problem.

These equations are averaged in time leading to the Reynolds Averaged Navier-Stokes (RANS) equations. This overcomes the high computational cost of the direct solution of the Navier-Stokes equations. Additional details about the formulation can be found in [44].

Increased accuracy can be achieved through alternative approaches such as the Detached Eddy Simulation (DES) which combines RANS equations near wall regions and Large Eddy Simulations (LES) [45], the direct simulation of the rest of the flow.

In this study, steady and unsteady RANS equations have been solved by the use of the Computational Fluid Dynamics (CFD) code TAU from the DLR. Finite volume discretization is employed on deformable unstructured meshes. This code has been applied and validated extensively in research and industry for both steady and unsteady problems [46].

The turbulence model used in all the simulations presented in this work is the Spalart-Allmaras model [47]. Steady solutions are obtained using the backward Euler implicit scheme with Lower-Upper Symmetric Gauss-Seidel (LU-SGS) iterations. Convergence is accelerated through a 2v multigrid scheme [48].

For the unsteady solution, the equations are integrated in time with the second order backward difference operator using a dual time stepping [48]. For subsonic problems, time step size is set to 0.004s with 100 inner iterations per time step. For transonic conditions, the time step size is set to 0.002s with 150 inner iterations per time step based on a similar configuration [49].

The method used to impose the atmospheric disturbances is the so called Disturbance Velocity Approach (DVA) (also known as Field Velocity Approach) [50]. The gust effect is added as a velocity term in the governing equations and prescribed in the mesh with no additional deformation of the grid required.

The resolution of the RANS equations in the time domain through CFD simulations can be applied for a detailed analysis of the relevant physics to quantify aerodynamic nonlinear effects in specific flight conditions [49]. In this case, these simulations are used for the validation of the model-based approach. The effect of possible aerodynamic nonlinearities is also analysed. In particular, when flying at high Mach numbers in transonic conditions, where shock motions or local stalls may appear due to gust and turbulence induced effects.

The CFD solver can also be coupled with a computational structural mechanics (CSM) and flight mechanics (FM) solver in order to deform the mesh according to the structural deformation and rigid body response of the aircraft respectively. The framework FlowSimulator is used to handle the coupling, the different sets of data and simulations [51]. Details about the unsteady aerodynamic solution in the time domain have been previously provided. Structural deformations are represented using a modal approach. The aerodynamic forces are projected to the different modes before calculating the aircraft response due to these forces. The structural equations are solved through a Newmark time integration scheme [52]. Rigid body and flexible motion calculated through the equations of motion presented in the next sections of this chapter are interpolated into the CFD surface mesh. The appropriate mesh deformation to account for the aircraft rigid and flexible motion is calculated and applied using the radial basis function method (RBF). Further details on the deformation technique can be found in [53] and [54]. Apart from the 6 rigid body modes, 90 flexible modes are retained. A similar coupling approach can be found in [55].

All the CFD simulations presented in this work are done with the same mesh. An

unstructured mesh with 11.4 million points is used for a similar configuration as the one presented in [12]. The surface mesh is shown in figure 1.1.

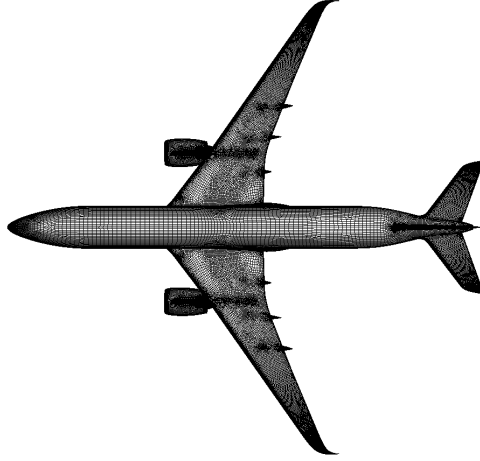


Figure 1.1: CFD surface mesh

1.1.2 Linearized Reynolds Averaged Navier Stokes (RANS) Equations

The previous detailed RANS equations can be linearized around a nonlinear steady state condition. The formulation is presented according to Bekemeyer [56]. Applying a finite-volume discretisation of the governing equations, for a fixed flight condition, the ordinary differential equation (ODE) in semi-discrete form can be expressed as:

$$\frac{\partial \boldsymbol{\nu} \mathbf{y}_f}{\partial t} = \mathbf{R}(\mathbf{y}_f, \mathbf{x}, \dot{\mathbf{x}}, \mathbf{w}_G) \quad (1.2)$$

with \mathbf{x} and $\dot{\mathbf{x}}$ being the change in mesh coordinates and their velocities respectively, \mathbf{w}_G being the gust disturbances which are accounted for through mesh velocities $\dot{\mathbf{x}}$. The term \mathbf{R} corresponds to the non-linear fluid residual of the unknowns of the problem and $\boldsymbol{\nu}$ contains the cell volumes in a matrix.

An increment between the conservative flow variable and the steady state solution can be defined:

$$\Delta \mathbf{y}_f = \mathbf{y}_f - \mathbf{y}_{f_s} \quad (1.3)$$

Similarly, for gust disturbances $\Delta \mathbf{w}_G = \mathbf{w}_G - \mathbf{w}_{G_s}$, mesh coordinates $\Delta \mathbf{x} = \mathbf{x} - \mathbf{x}_s$ and velocities $\Delta \dot{\mathbf{x}} = \dot{\mathbf{x}} - \dot{\mathbf{x}}_s$. When assuming small disturbances, a Taylor expansion can

be applied around the steady state:

$$\boldsymbol{\nu} \frac{d\Delta\mathbf{y}_f}{dt} + \mathbf{y}_f \frac{d\Delta\boldsymbol{\nu}}{dt} = \mathbf{R}(\mathbf{y}_{fs}, \mathbf{x}_s, \dot{\mathbf{x}}_s, \mathbf{w}_{Gs}) + \frac{\partial \mathbf{R}}{\partial \mathbf{y}_f} \Delta\mathbf{y}_f + \frac{\partial \mathbf{R}}{\partial \mathbf{x}} \Delta\mathbf{x} + \frac{\partial \mathbf{R}}{\partial \dot{\mathbf{x}}} \Delta\dot{\mathbf{x}} + \frac{\partial \mathbf{R}}{\partial \mathbf{w}_G} \Delta\mathbf{w}_G + \dots \quad (1.4)$$

with $\frac{\partial \mathbf{R}}{\partial \mathbf{y}_f}$ being the fluid Jacobian matrix, $\frac{\partial \mathbf{R}}{\partial \mathbf{x}}$, $\frac{\partial \mathbf{R}}{\partial \dot{\mathbf{x}}}$ and $\frac{\partial \mathbf{R}}{\partial \mathbf{w}_G}$ changes in the fluid residual due to mesh deformation, mesh velocities and gust disturbance, respectively. The different derivatives are defined around the nonlinear steady state condition. The term $\mathbf{R}(\mathbf{y}_{fs}, \mathbf{x}_s, \dot{\mathbf{x}}_s, \mathbf{w}_{Gs})$ is the nonlinear steady-state flow residual which accounts for the steady aerodynamic nonlinearities. A well converged steady solution is important before solving the linearized problem.

Assuming harmonic excitation ($\Delta\mathbf{w}_G = \hat{\mathbf{w}}_G e^{j\omega t}$) and the fact that the system also change harmonically in time, it is possible to express equation 1.4 in the frequency domain:

$$\left(\frac{\partial \mathbf{R}}{\partial \mathbf{y}_f} - jk\boldsymbol{\nu} \right) \hat{\mathbf{y}}_f = -\frac{\partial \mathbf{R}}{\partial \mathbf{x}} \hat{\mathbf{x}} - \frac{\partial \mathbf{R}}{\partial \dot{\mathbf{x}}} \hat{\dot{\mathbf{x}}} + \hat{\mathbf{y}}_f \frac{d\Delta\boldsymbol{\nu}}{dt} - \frac{\partial \mathbf{R}}{\partial \mathbf{w}_G} \hat{\mathbf{w}}_G \quad (1.5)$$

with $\hat{\mathbf{y}}_f$, $\hat{\mathbf{x}}$, $\hat{\dot{\mathbf{x}}}$ and $\hat{\mathbf{w}}_G$ being the Fourier coefficients.

The reduced frequency k is defined as:

$$k = \frac{\omega l_{ref}}{V_\infty} = \frac{(2\pi f) l_{ref}}{V_\infty} \quad (1.6)$$

with ω being the angular frequency, l_{ref} being the reference chord length, f being the frequency and V_∞ the true air speed.

Changes in rigid body motion, surface deflection or structural deformation can be taken into account through mesh deformation and velocities (\mathbf{x} , $\dot{\mathbf{x}}$). In the present work, the considered disturbance is the one from gust excitations according to [56]. The idea behind the approach is the same for other forced motions. Changes in the aerodynamic residual due to harmonic gust disturbances are denoted by the term $\frac{\partial \mathbf{R}}{\partial \mathbf{w}_G} \hat{\mathbf{w}}_G$, which can also be expressed as:

$$\frac{\partial \mathbf{R}}{\partial \mathbf{w}_G} \hat{\mathbf{w}}_G = \frac{\partial \mathbf{R}}{\partial \dot{\mathbf{x}}} \frac{\partial \dot{\mathbf{x}}}{\partial \mathbf{w}_G} \hat{\mathbf{w}}_G \quad (1.7)$$

with $\dot{\mathbf{x}}$ being the mesh velocities used to take into account the gust effect in the CFD simulation through the disturbance velocity approach. By using this technique, the relation between the gust disturbance \mathbf{w}_G and the mesh velocity $\dot{\mathbf{x}}$ is:

$$\dot{\mathbf{x}} = -\mathbf{w}_G \quad (1.8)$$

The gust-induced effect can be then written as:

$$\frac{\partial \mathbf{R}}{\partial \mathbf{w}_G} \hat{\mathbf{w}}_G = -\frac{\partial \mathbf{R}}{\partial \dot{\mathbf{x}}} \hat{\mathbf{w}}_G \quad (1.9)$$

Before solving the linear system in equation 1.5, the gust-induced term can be directly calculated by evaluating the residual through finite-difference discretisation, avoiding the matrix calculation and storage:

$$\frac{\partial \mathbf{R}}{\partial \mathbf{w}_G} \hat{\mathbf{w}}_G = \frac{\mathbf{R}(\mathbf{y}_{fs}, \mathbf{x}_s, \dot{\mathbf{x}}_s, \mathbf{w}_{Gs} + \delta \hat{\mathbf{w}}_G) - \mathbf{R}(\mathbf{y}_{fs}, \mathbf{x}_s, \dot{\mathbf{x}}_s, \mathbf{w}_{Gs} - \delta \hat{\mathbf{w}}_G)}{2\delta} \quad (1.10)$$

with the gust shape vector $\hat{\mathbf{w}}_G$ which is known and the finite-difference step size δ , which need to be small to avoid errors due to higher order terms but large enough to avoid errors from the limited accuracy of the residual [48].

The gust shape vector can be expressed analytically as:

$$\hat{\mathbf{w}}_G = w_{Gz} e^{j\varphi(\mathbf{x}, k)} \quad (1.11)$$

with w_{Gz} being the gust amplitude and φ being the phase shift which is evaluated for each mesh element and it is associated with the gust propagation effect, which is the fact that the gust affects the different aircraft parts at different times. This phase shift can be expressed for each element as:

$$\varphi(\mathbf{x}, k) = \frac{(\mathbf{x} + x_0)}{V_\infty} \omega = (\mathbf{x} + x_0) \frac{k}{l_{ref}} \quad (1.12)$$

with x_0 being the distance between the gust and the aircraft reference point. The harmonic gust vector is extended in all the different directions. Figure 1.2 shows an example of the definition of a high frequency vertical gust mode excitation over the CFD mesh of a generic aircraft configuration. All the points over the computational domain are affected by the harmonic gust excitation.

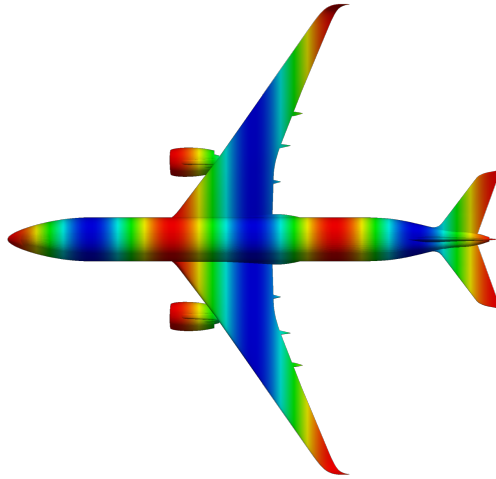


Figure 1.2: Vertical gust mode shape over the CFD mesh

Lateral gusts can be also defined by modifying the direction of the mesh velocity (towards y axis instead of z axis as the vertical disturbance):

$$\hat{\boldsymbol{w}}_{\boldsymbol{G}} = w_{Gy} e^{j(\boldsymbol{x}+x_0)\frac{k}{l_{ref}}} \quad (1.13)$$

The solution of equation 1.5 gives the aircraft aerodynamic response ($\hat{\boldsymbol{y}}_f$) to a predefined harmonic vertical or lateral gust excitation ($\hat{\boldsymbol{w}}_{\boldsymbol{G}}$) at a specific reduced frequency (k). By exciting different frequencies, the response can be calculated obtaining the so-called frequency response function. From this information in the frequency domain, different techniques are possible in order to calculate the response in the time domain due to aperiodic gust excitations such as the 1-cos gust shape profile. The advantage of solving the linearized RANS equations is that the computationally expensive solution of equation 1.5 at different reduced frequencies is done only once. When the frequency response function has been obtained, the response to different gust profiles in the time domain can be investigated without requiring additional CFD simulations while staying at the considered flight condition. Responses in the frequency domain can also be directly considered [56].

The Linearized Frequency Domain (LFD) solver of the DLR code TAU is used to solve the linearized RANS equations. The linear system is solved through an iterative method as for the solution of the RANS equations in the time domain. The DLR code TAU uses a first-discretise-then-linearise matrix-forming approach with the fluid Jacobian matrix derived analytically [56]. This allows for efficient computation in complex test cases. The iterative method used to solve the linear system is a LU-SGS smoothed linear multigrid cycle [57]. A Generalized Minimal Residual algorithm (GMRes) is used in order to stabilize and accelerate the linear multigrid solver [48]. This method has the property of minimizing the norm of the residual over a Krylov subspace [58]. The mesh used to solve the linearized RANS equations with CFD is the same as the one presented in section 1.1.1.

Linearized CFD simulations in the frequency domain are able to capture aerodynamic effects such as shock waves at transonic conditions without required corrections in a reasonable computational cost. Simulation results in the frequency domain are used to build a model able to capture the gust-induced effects in the time domain for arbitrary gust excitations and in a reasonable amount of time. Details about the model are given in sections 1.3.2 and 2.3.

As demonstrated in the formulation, the approach makes the assumption that low-amplitude harmonic disturbances are applied to the nonlinear steady condition which is the same as the one used to solve the RANS equations in the time domain. This allows the linearization of the RANS equations in the frequency domain around the steady state as shown in this part, reducing the overall computational cost. Further details on the approach are given in [13]. Additional information and extension of the technique to the gust-induced effects can be found in [56].

1.1.3 Doublet Lattice Method (DLM)

The classical Doublet Lattice Method (DLM) used traditionally in unsteady aerodynamic problems is also considered in order to capture both gust and motion induced effects [6]. The formulation is detailed according to Quero [43].

When neglecting viscous effects and power exchanged by conduction in the previous presented nonlinear RANS equations, the Euler equations are obtained:

$$\frac{\partial \mathbf{y}_f}{\partial t} + \nabla \cdot \mathbf{f}(\mathbf{y}_f) = 0 \quad (1.14)$$

The assumption of irrotational flow ($\nabla \times \mathbf{v}$) allows expressing the velocity as a gradient of a scalar potential function (ϕ_v) as $\mathbf{v} = \nabla \phi_v$.

The mass and energy conservation are given with these assumptions in equations 1.15 and 1.16. Equation 1.16 is also known as the Bernoulli equation.

$$\frac{\partial \rho}{\partial t} + \nabla \cdot (\rho \nabla \phi_v) = 0 \quad (1.15)$$

$$\frac{\partial \phi_v}{\partial t} + \frac{\|\nabla \phi_v\|^2}{2} - \frac{V_\infty^2}{2} + \frac{a_\infty^2}{\gamma - 1} \left[\left(\frac{\rho}{\rho_\infty} \right)^{\gamma - 1} \right] = 0 \quad (1.16)$$

with V_∞ as the freestream velocity, a_∞ being the speed of sound and γ the heat capacity ratio.

Even if the assumption of zero vorticity is made, circulation vorticity at the boundary layer and the wake is imposed to capture the lift affecting the body. The unique solution to the problem is obtained by adding the wake condition and the tangential flow condition around the body. There are limitations of the irrotational assumption when analysing transonic conditions as the presence of shock waves cannot be properly captured. However, some possibilities exist to approximate the effect at moderate upstream Mach numbers [20].

The density can be evaluated with equation 1.16 and applied to equation 1.15 in order to obtain the equation for the velocity potential (ϕ_v):

$$\nabla^2 \phi_v - \frac{1}{a_\infty^2} \left[\frac{\partial^2 \phi_v}{\partial t^2} + \frac{\partial(v^2)}{\partial t} + \nabla \phi_v \cdot \nabla \left(\frac{v^2}{2} \right) \right] = 0 \quad (1.17)$$

with $v = \|\nabla \phi_v\|$.

The total potential (ϕ_v) can be expressed as a sum of a steady and small disturbance component ($\phi_v = \phi_s + \phi_p$). The linear aerodynamic potential equation is given in equation 1.18, assuming a constant speed of sound (a_∞) and freestream Mach number (M_∞):

$$(1 - M_\infty^2) \frac{\partial^2 \phi_p}{\partial x^2} + \frac{\partial^2 \phi_p}{\partial y^2} + \frac{\partial^2 \phi_p}{\partial z^2} - \left(\frac{2V_\infty}{a_\infty^2} \right) \frac{\partial^2 \phi_p}{\partial x \partial t} - \left(\frac{1}{a_\infty^2} \right) \frac{\partial^2 \phi_p}{\partial t^2} = 0 \quad (1.18)$$

This equation is completed with the boundary condition specifying the flow to be tangential to the surface, as there is no shear force due to the absence of viscosity. It is assumed that the thickness component is time independent which can be modelled by source panels and it can be superposed to the time dependent flow solution over the body midplane modelled by a doublet sheet.

In order to solve the problem, the different possible solutions to the linear aerodynamic potential equation which can be superposed need to satisfy the boundary conditions. The farfield condition is satisfied when superposing doublet and sources, as their effect tends to zero when the distance tends to the infinite. The assumption of irrotational flow which neglects viscosity needs to be complemented with the Kutta condition to fix the flow circulation around the lifting surface and find a unique solution. This condition established that the pressure difference across the wake at the trailing edge is zero for the linearized flow.

It can be demonstrated that the harmonically oscillating source potential is an elementary valid solution to the linear aerodynamic potential equation. A source cannot generate lift and the potential is differentiated, which yields the doublet potential. The term acceleration potential ($\Psi(x, y, z, t)$) shown in equation 1.19 is used, which allows expressing the source and doublet solutions to the problem as a function of the pressure difference between the upper and lower surface of the lifting body.

$$\Psi(x, y, z, t) = - \left[\frac{\partial}{\partial t} + V_\infty \frac{\partial}{\partial x} \right] |\phi_p| e^{j\omega t} \quad (1.19)$$

The integral equation 1.20 can be obtained through the acceleration potential, which relates the downwash ($|w|$) with the pressure ($|P|$) magnitude. The kernel function is given in equation 1.21, with $B^2 = 1 - M_\infty^2$ and $K_0 = \sqrt{\lambda^2 + B^2 y_0^2 + B^2 z_0^2}$.

$$|w|(x, y, z) = \frac{-1}{4\pi\rho V_\infty} \iint_S \Delta|P| K((x - \zeta), (y - \eta), z) d\zeta d\eta \quad (1.20)$$

$$K(x_0, y_0, z_0) = \exp\left(\frac{-j\omega x_0}{V_\infty}\right) \frac{\partial}{\partial z^2} \left[\int_{-\infty}^{x_0} \frac{1}{K_0} \exp\left(\frac{j\omega}{V_\infty B^2}(\lambda - M_\infty R)\right) d\lambda \right] \quad (1.21)$$

The solution to the problem is obtained by determining the doublet distribution which satisfies equation 1.20 and the tangential boundary condition. The downwash (w) is known for each problem and the unknown to determine is the pressure distribution. DLM provides a numerical solution to this equation. The geometry of the lifting body is divided in panels as shown in figure 1.3 and equation 1.20 is evaluated at each panel independently. The doublet is placed at the quarter chord of the panel and the flow tangency boundary condition is imposed at the three quarter chord. The pressure is assumed to be spatially

constant at each panel and the unknowns can come out of the integration term. The concept of principle values is used to deal with the singularities along the doublet line at the quarter chord of the panel. Geometrical effects such as dihedral angle can be taken into account by modifying the geometry of the DLM grid shown in figure 1.3.

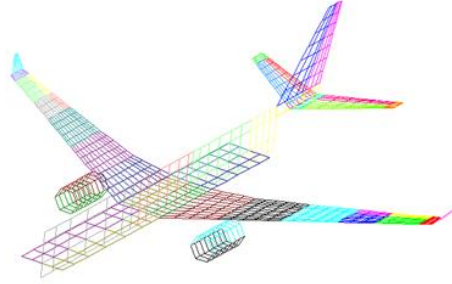


Figure 1.3: DLM panel discretisation of a generic aircraft

The solution of the problem in terms of pressure coefficient is shown in equation 1.22.

$$\Delta \mathbf{c}_p = \mathbf{Q}(M_\infty, k) \mathbf{w}(k) \quad (1.22)$$

with $\mathbf{Q}(M_\infty, k)$ being the so called Aerodynamic Influence Coefficient (AIC) matrix which is defined for each panel and provides the incremental pressure coefficient ($\Delta \mathbf{c}_p$) between the upper and lower surface of a lifting surface due to a local angle of attack (or downwash) variation. The AIC matrix depends on the freestream Mach number (M_∞) and the reduced frequency (k) specified in equation 1.6. The pressure difference $\Delta \mathbf{c}_p$ is given at the quarter chord of the panel and the downwash $\mathbf{w}(k)$ is specified at three quarters of the panel chord. The downwash nondimensionalized with the freestream velocity (V_∞) can be associated to a local angle of attack variation. Further details on the approach can be found in [59].

This potential method captures essential physical aspects when simulating the aircraft response due to gust encounters, such as the propagation effect of the wind through the different aircraft parts as well as linear unsteady aerodynamic effects at subsonic conditions due to gust and rigid or structural flexible motion.

The theoretical results from DLM need to be corrected to account for additional effects such as viscosity or geometrical parameters like the thickness. Correction methods using data from wind tunnel test or higher fidelity methods such as CFD can be applied to extend its applicability, in particular in the transonic regime. The DLM results used in this study have been corrected with a quasi-steady aerodynamic database.

1.2 Flight Dynamics Response

The aircraft response in flight can be described by the principles of classical mechanics, which deal with the motion of bodies possessing a scalar inertial property known as mass [60]. This part details some of the main elements to be able to predict the flight dynamics response. In particular, the equations of motion to calculate how the aircraft reacts to external forces with its reference system. Different contributions need to be taken into account as external forces. This work focuses on the aerodynamic contribution and other kind of forces such as the thrust computed from engine models is not detailed. The aerodynamic model and assumptions used in flight mechanics to express the external aerodynamic forces and moments is also presented, which is based on some of the previous presented formulations in conjunction with experimental results coming from wind tunnel or flight test.

1.2.1 Equations of Motion

The flight dynamics equations of motion are based on Newton-Euler six-degrees of freedom equations for a rigid body expressed in the body-fixed reference frame (b). The derivation of the equation of motion can be found in [34]. The formulation is given in equations 1.23 and 1.24 according to Reschke [34] and Looye [38].

$$m(\dot{\mathbf{V}}_b + \boldsymbol{\Omega}_b \times \mathbf{V}_b - \mathbf{T}_{bE}\mathbf{G}_E) = \mathbf{F}_b \quad (1.23)$$

$$\mathbf{J}_b\dot{\boldsymbol{\Omega}}_b + \boldsymbol{\Omega}_b \times \mathbf{J}_b\boldsymbol{\Omega}_b = \mathbf{M}_b \quad (1.24)$$

where \mathbf{V}_b and $\boldsymbol{\Omega}_b$ are the translational and angular velocity vectors expressed in the body axes, m and \mathbf{J}_b are the total mass and inertia tensor of the aircraft respectively. The matrix \mathbf{T}_{bE} refers to the transformation from the geodetic reference frame (E) to body axis (b) and \mathbf{G}_E is the gravitational vector in the geodetic frame. \mathbf{F}_b and \mathbf{M}_b contain the different external forces and moments defined in the body axis such as the ones from aerodynamics, thrust and other external contributions. Under the assumption of small angular motions, the flight mechanics equations can be linearized and solved through a modal approach.

The geodetic reference system is assumed to be an earth-fixed inertial system. Figure 1.4 shows the body and geodetic inertial frame. It is possible to define the position of the aircraft with respect to the geodetic inertial reference system:

$$\mathbf{L}_E = [x_{0E} \ y_{0E} \ z_{0E}]^T \quad (1.25)$$

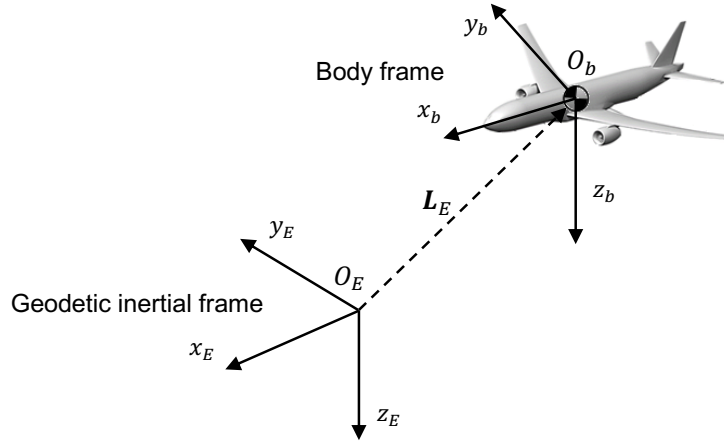
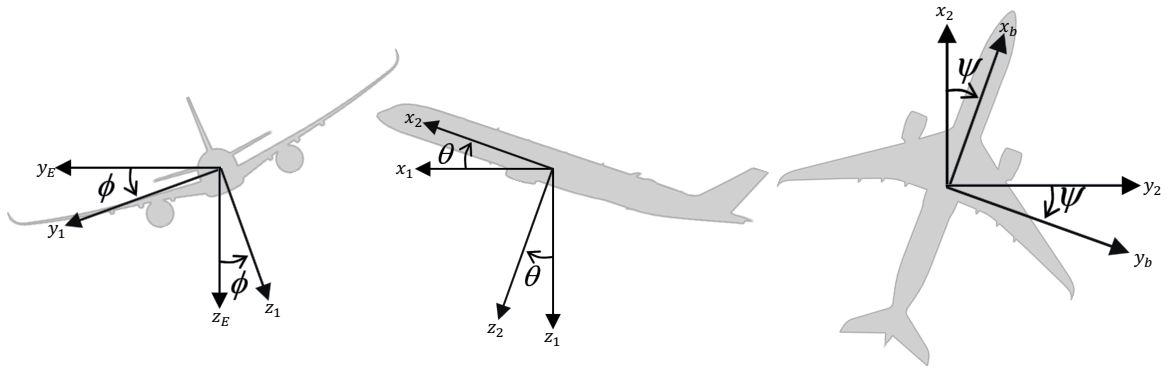


Figure 1.4: Geodetic and body reference frames

An intermediate reference frame parallel to the geodetic inertial frame with the origin moving with the aircraft centre of gravity can be defined. The orientation of the body fixed frame can be defined with respect to this reference frame by the so-called Euler angles as shown in equation 1.26. Euler angles are represented in figure 1.5.

$$\Theta = [\phi \ \theta \ \psi]^T \quad (1.26)$$

Figure 1.5: Euler angles defining the orientation of the body frame (b) with respect to the geodetic frame (E). Intermediate axes (1, 2) are defined for the rotation sequence.

The translational (\mathbf{V}_b) and angular ($\mathbf{\Omega}_b$) velocity vectors are expressed in the body frame:

$$\mathbf{V}_b = [u_b \ v_b \ w_b]^T \quad (1.27)$$

$$\mathbf{\Omega}_b = [p \ q \ r]^T \quad (1.28)$$

Kinematic relations are formulated to express the translational and angular velocities from body axes to the inertial frame:

$$\dot{\mathbf{L}}_E = \mathbf{T}_{Eb} \mathbf{V}_b \quad (1.29)$$

$$\dot{\boldsymbol{\Theta}} = \mathbf{D}^{-1} \boldsymbol{\Omega}_b \quad (1.30)$$

with \mathbf{T}_{Eb} being the transformation matrix between body to the inertial frame given in equation 1.31. The transformation matrix between the time derivative of the Euler angles and angular velocity expressed in body axis \mathbf{D} is given in equation 1.32. Additional details can be found in [5].

$$\mathbf{T}_{Eb} = \begin{bmatrix} \cos \theta \cos \psi & \sin \phi \sin \theta \cos \psi - \cos \phi \sin \psi & \cos \phi \sin \theta \cos \psi + \sin \phi \sin \psi \\ \cos \theta \sin \psi & \sin \phi \sin \theta \sin \psi + \cos \phi \cos \psi & \cos \phi \sin \theta \sin \psi - \sin \phi \cos \psi \\ -\sin \theta & -\sin \phi \cos \theta & \cos \phi \cos \theta \end{bmatrix} \quad (1.31)$$

$$\mathbf{D} = \begin{bmatrix} 1 & 0 & -\sin \theta \\ 0 & \cos \phi & \cos \theta \sin \phi \\ 0 & -\sin \phi & \cos \theta \cos \phi \end{bmatrix} \quad (1.32)$$

1.2.2 Quasi-steady Flexible Aerodynamic Model

In equations 1.23 and 1.24, the aerodynamic forces and moments are calculated according to a quasi-steady flexible aerodynamic model, which cover a wide range of aircraft conditions. This model is able to capture the main aerodynamic effects occurring for slow aircraft manoeuvres, the typical ones of current aircraft passenger configurations, including nonlinear effects such as stall as well as compressible effects appearing at high Mach numbers. This is achieved by combining data from different sources such as CFD simulations according to the formulations presented previously, wind tunnel tests and once the aircraft has been designed and manufactured, flight tests measures. Different forms of the model are possible, but the typical way of expressing the aerodynamic forces and moments is given in equations 1.33 and 1.34 according to Looye [38].

$$\mathbf{F}_b = \bar{q} S_{ref} \mathbf{T}_{ba} \begin{bmatrix} C_x \\ C_y \\ C_z \end{bmatrix} \quad (1.33)$$

$$\mathbf{M}_b = \bar{q} S_{ref} l_{ref} \mathbf{T}_{ba} \begin{bmatrix} C_l \\ C_m \\ C_n \end{bmatrix} + \mathbf{r}_{CG-25\%} \times \mathbf{F}_b \quad (1.34)$$

with \bar{q} being the dynamic pressure, S_{ref} the wing reference area, l_{ref} is the reference length, which is usually the Mean Aerodynamic Chord (MAC) of the wing or the half wing span. The dimensionless force (drag C_x , side-force C_y and lift C_z) and moment (rolling C_l , pitching C_m and yawing C_n) coefficients are expressed in the aerodynamic reference system (a). The distance between the aircraft centre of gravity and the origin of the aerodynamic reference system is $r_{CG-25\%}$. The origin of the aerodynamic frame is usually positioned at 25% of the MAC of the wing. The matrix \mathbf{T}_{ba} , given in equation 1.35, transforms the forces and moments expressed in the aerodynamic reference frame to the body frame. The angles defining the orientation of the aerodynamic reference frame are the angle of attack (α) and sideslip (β) and are shown in figure 1.6.

$$\mathbf{T}_{ba} = \begin{bmatrix} \cos \beta \cos \alpha & -\sin \beta \cos \alpha & -\sin \alpha \\ \sin \beta & \cos \beta & 0 \\ \cos \beta \sin \alpha & -\sin \beta \sin \alpha & \cos \alpha \end{bmatrix} \quad (1.35)$$

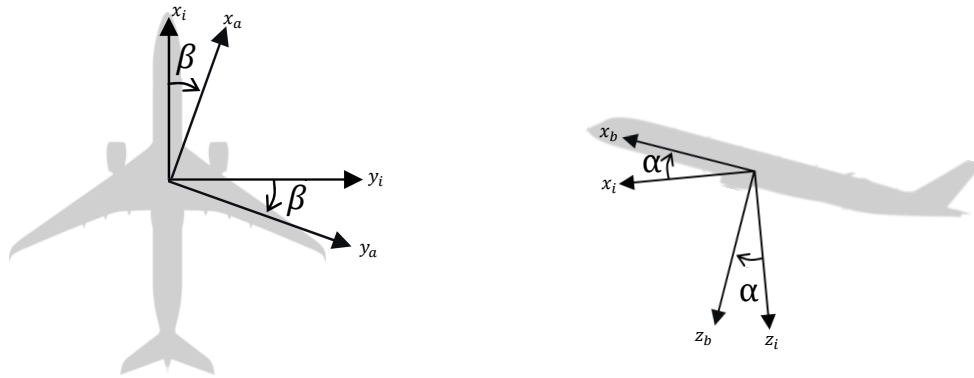


Figure 1.6: Angle of attack (α) and sideslip (β) defining the orientation of the aerodynamic reference system (a) with respect to the body frame (b). Intermediate axes (i) are defined for the rotation sequence.

The aerodynamic coefficients are given through mathematical expressions as a function of different parameters such as the angle of attack (α), sideslip (β), Mach number (M), body angular rates (p , q , r) or control surface deflection, among others. Apart from the aerodynamic quasi-steady contribution, this model may also include some unsteady effects. The most relevant is the lag effect of the downwash angle on the horizontal tail plane due to an angle of attack variation at the wing (incidence rate effect $\dot{\alpha}$). Terms such as $C_{z\dot{\alpha}}$ for the lift force coefficient capture this downwash delay between the wing and the horizontal tail plane. Next chapter provides a possibility to include the gust and turbulence induced effects at low frequencies. An example of some terms that contribute to the lift force

coefficient (C_z) are given in equation 1.36.

$$C_z = C_{z0} + C_{z\alpha}\alpha + C_{z\beta}\beta + C_{zq}\frac{q l_{ref}}{V_\infty} + C_{z\dot{\alpha}}\frac{\dot{\alpha} l_{ref}}{V_\infty} + \dots \quad (1.36)$$

The coefficients can be corrected to account for the effects of the quasi-static flexible deformation of the airframe [61]. The corrections are meant to include flexible effects in the rigid aerodynamic coefficients at frequencies close to zero. This correction usually depends on the vertical load factor and dynamic pressure [5]. The dynamic effect appearing when the flexible modes are excited is not taken into account. Chapter 2 describes a possibility to add the dynamic flexible effect. Different responses with and without this modelling assumption are analysed in chapter 3. Additional details on the aerodynamic modelling used for flight mechanics analysis can be found in [5, 60].

1.3 Aeroelastic Response

The aeroelastic response of the aircraft deals with the perturbations appearing around a trimmed flight state, which can be calculated with the previous detailed equations 1.23 and 1.24. This is useful to predict the flutter stability margins of the aircraft as well as the loads that appear when the aircraft encounters gust or turbulence, relevant to achieve certification [3]. These perturbations can be predicted through modally reduced linear elastic equations of motion, which are presented in this section. These equations are able to capture the unsteady interactions between the aircraft structural dynamics and the airflow. Unsteady aerodynamic models used in conjunction with the equations of motion and based on the previous detailed aerodynamic formulations are also detailed. The aeroelastic response can be also expressed through a state space model for aeroservoelastic applications, as presented at the end of this section.

1.3.1 Equations of Motion

The linear Finite Element Method (FEM) is used to numerically discretize the aircraft structure. The model consist of different grid points with mass and stiffness elements. The global aircraft FEM model shown in figure 1.7 can be reduced to retain the most relevant degrees of freedom for the analysis. A condensation of the model in a reduced number of degrees of freedom simplifies and reduces the computational cost of the dynamic analysis. Condensed lumped masses and inertia elements are calculated and attached to the retained grid points which are elastically interconnected with the appropriate stiffness elements [62]. Figure 1.8 shows the condensed model with the structural reference frame.



Figure 1.7: Global FEM model

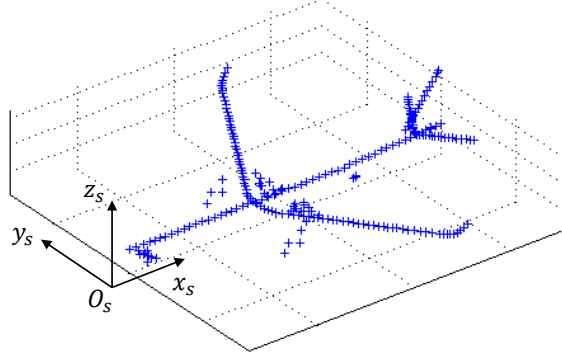


Figure 1.8: Condensed FEM model with structural reference frame

The linear aeroelastic equations of motion in the structural reference system are given in equation 1.37 according to Looye [38]. The derivation can be found in [34].

$$\mathbf{M}_{gg}\ddot{\mathbf{x}}_g(t) + \mathbf{B}_{gg}\dot{\mathbf{x}}_g(t) + \mathbf{K}_{gg}\mathbf{x}_g(t) = \mathbf{F}_g(t) \quad (1.37)$$

with \mathbf{M}_{gg} , \mathbf{B}_{gg} and \mathbf{K}_{gg} being the mass, damping and stiffness matrix of the degrees of freedom of the FEM structural model, \mathbf{x}_g being the degrees of freedom of the grid points with respect to the structural reference system, which has the dimension n_g . Structural damping is usually neglected in aeroelastic analysis. The external forces applied to the set of interconnected grid points is \mathbf{F}_g , expressed as well in the structural reference frame.

A modal analysis of the aircraft configuration is performed from equation 1.37, neglecting the structural damping, without an external excitation ($\mathbf{F}_g = 0$) and without constraints (free aircraft). By assuming the small linear displacements of the degrees of freedom which can be expressed as a superposition of harmonic functions ($\mathbf{x}_g = \hat{\mathbf{x}}_g e^{j\omega t}$), equation 1.37 can be expressed in the frequency domain:

$$(-\omega^2 \mathbf{M}_{gg} + \mathbf{K}_{gg})\mathbf{x}_g(\omega) = 0 \quad (1.38)$$

The structural modes of the studied configuration defined by its eigenfrequencies and the associated mode shape eigenvectors can be obtained from equation 1.38. In this study, the eigenfrequencies and modal matrix ϕ_{gh} which collects the eigenvectors in columns have been calculated with the software MSC.Nastran [63]. The first six eigenfrequencies have a value close to zero and correspond to the six rigid body modes.

The structural displacements (\mathbf{x}_g) can be expressed as a function of the modal or generalized coordinates (\mathbf{u}_h) as shown in equation 1.39.

$$\mathbf{x}_g = \phi_{gh}\mathbf{u}_h = [\phi_{gr} \quad \phi_{ge}] \begin{bmatrix} \mathbf{u}_r \\ \mathbf{u}_e \end{bmatrix} \quad (1.39)$$

Rigid body and flexible degrees of freedom can be considered separately. The modes are divided in rigid with subscripts r and elastic with subscript e . The number of eigenvectors considered in ϕ_{gh} can be truncated leading to an additional reduction in the considered degrees of freedom. The order of magnitude of the retained number of modes is close to 100. This usually covers the frequency range of interest and beyond. The number of retained eigenvectors which define the modal basis is usually smaller than the total number of structural degrees of freedom ($n_h < n_g$). The approximation is justified by the fact that the neglected modes have a low energy and its contribution to the structural deformation of the degrees of freedom is several orders of magnitude lower than the one from the retained modes.

The flight mechanics response is taken into account through the rigid body modes assuming low amplitude angular motions. The rigid body modes obtained from the modal analysis are defined in arbitrary directions. A redefinition of the rigid body modes corresponding to the three translations and three rotations may be of interest for aeroelastic analysis [43]. A possible correction involves imposing unit translations and rotations around the centre of gravity respectively according to the direction of the body reference frame [38] presented in section 1.2.

The equation of motion 1.37 can be projected in the reduced set of generalized coordinates. Replacing equation 1.39 in equation 1.37 expressed in the frequency domain, the half-generalized form of the linear aeroelastic equations of motion is obtained:

$$(-\omega^2 \mathbf{M}_{gh} + j\omega \mathbf{B}_{gh} + \mathbf{K}_{gh}) \mathbf{u}_h(\omega) = \mathbf{F}_g(\omega) \quad (1.40)$$

with \mathbf{M}_{gh} , \mathbf{B}_{gh} and \mathbf{K}_{gh} being the half-generalized mass, damping and stiffness respectively. Modal damping can be estimated or identified from experiments. This form of the equation is interesting for loads analysis, as it provides the load distribution along the airframe.

Multiplying equation 1.40 by the modal matrix (ϕ_{gh}^T) provides the equations of motion in modal coordinates (h) expressed in the frequency (equation 1.41) and time (equation 1.42) domain.

$$(-\omega^2 \mathbf{M}_{hh} + j\omega \mathbf{B}_{hh} + \mathbf{K}_{hh}) \mathbf{u}_h(\omega) = \phi_{gh}^T \mathbf{F}_g(\omega) \quad (1.41)$$

$$\mathbf{M}_{hh} \ddot{\mathbf{u}}_h(t) + \mathbf{B}_{hh} \dot{\mathbf{u}}_h(t) + \mathbf{K}_{hh} \mathbf{u}_h(t) = \phi_{gh}^T \mathbf{F}_g(t) \quad (1.42)$$

with \mathbf{M}_{hh} , \mathbf{B}_{hh} and \mathbf{K}_{hh} being the generalized mass, damping and stiffness matrices respectively, which are diagonal due to the orthogonality of the modes and \mathbf{u}_h as the generalized coordinates divided in rigid (\mathbf{u}_r) and elastic (\mathbf{u}_e) contributions which are the solutions of the equation of motion. When adapting the rigid body modes according to the body reference frame as suggested by Looye [38], the total aircraft mass (m) and inertia tensor (\mathbf{J}_b) can be found in the diagonal terms of the rigid partition (\mathbf{M}_{rr}) of the

generalized mass matrix (\mathbf{M}_{hh}). The term $\phi_{gh}^T \mathbf{F}_g$ is the projection of the external forces to the different rigid and flexible modes and quantifies the effect of the external excitation on each mode. Next section focuses on different forms of the aerodynamic contribution (\mathbf{F}_g) both in the frequency and time domain.

1.3.2 Unsteady Aerodynamic Model

The unsteady aerodynamic contribution in the aeroelastic equations of motion can take different forms and can be expressed both in the frequency and time domain. The form of the models is based on the results obtained from the aerodynamic formulations presented in section 1.1. The number of load cases can exceed several hundreds of thousands and efficient computation methods are required.

Different contributions can be considered when calculating the aerodynamic forces projected to the generalized coordinates (term $\phi_{gh}^T \mathbf{F}_g$) as shown in equation 1.43. Unsteady aerodynamic forces can be induced by the aircraft motion (\mathbf{F}_h^u), control surface deflection (\mathbf{F}_h^{cs}) and gust or turbulence (\mathbf{F}_h^{gust}). In this study, only motion and gust induced effects are considered but unsteady aerodynamic effects from control surface deflections can be easily added in a similar way. This part describes the form to express the unsteady aerodynamic contribution from both motion and gust or turbulence induced effects in the frequency and time domain.

$$\phi_{gh}^T \mathbf{F}_g = \mathbf{F}_h^u + \mathbf{F}_h^{cs} + \mathbf{F}_h^{gust} \quad (1.43)$$

Frequency Domain

The form of the unsteady aerodynamic forces obtained from DLM or CFD simulations is described in order to solve the equations of motion in the frequency domain (equation 1.41).

Results from DLM, as stated in section 1.1.3, provide the incremental pressure coefficient distribution over the different panels through the calculation of the Aerodynamic Influence Coefficient (AIC) as shown in equation 1.22. The AIC matrix expressed in the DLM aerodynamic grid (j) relates a downwash at each panel to the increment of pressure coefficient. The downwash can account for different effects, such as the one created by a gust or induced by the aircraft motion and it can be seen as a local angle of attack variation at each panel. The aircraft motion and deformation in modal coordinates (\mathbf{u}_h) needs to be translated into the downwash effect through the modal panel deflection [17]. The gust downwash corresponds to the imposed harmonic wind distribution all along the aircraft. A spline matrix (\mathbf{G}_{gj}) is also required in order to project the forces from the aerodynamic grid to the structural reference frame [43]. The forces expressed in the structural frame can be projected to the different modes through the modal matrix (ϕ_{gh}), obtaining

the so called Generalized Aerodynamic Force (GAF), which indicate the impact of the disturbance on each aircraft mode as a function of the frequency. The generalized (\mathbf{Q}_{hh} , \mathbf{Q}_{hG}) and half-generalized (\mathbf{Q}_{gh} , \mathbf{Q}_{gG}) aerodynamic forces can be expressed as shown in equations 1.44 and 1.45 for motion and gust induced effects respectively.

$$\mathbf{F}_h^u(\omega) = \bar{q}\phi_{gh}^T \mathbf{G}_{gj} \mathbf{Q}_{jh} \mathbf{u}_h = \bar{q}\phi_{gh}^T \mathbf{Q}_{gh} \mathbf{u}_h = \bar{q}\mathbf{Q}_{hh} \mathbf{u}_h \quad (1.44)$$

$$\mathbf{F}_h^{gust}(\omega) = \bar{q}\phi_{gh}^T \mathbf{G}_{gj} \mathbf{Q}_{jG} \mathbf{w}_G = \bar{q}\phi_{gh}^T \mathbf{Q}_{gG} \mathbf{w}_G = \bar{q}\mathbf{Q}_{hG} \mathbf{w}_G \quad (1.45)$$

with \mathbf{Q}_{hh} and \mathbf{Q}_{gh} being the unsteady motion-induced in generalized and half-generalized form respectively. The generalized and half-generalized gust induced forces are also included (\mathbf{Q}_{hG} and \mathbf{Q}_{gG}). These matrices depend on the mach number (M) and reduced frequency (k). The gust and turbulence inputs are given by \mathbf{w}_G . Additional inputs such as control surface deflections (ailerons, spoilers, elevator or rudder) could be considered with the appropriate GAF calculation associated with the effect. Additional details on the derivation of these forces from DLM can be found in [43].

Simulation results with CFD linearized in the frequency domain (LFD) according to the formulation detailed in section 1.1.2 can directly provide generalized aerodynamic forces due to motion (\mathbf{Q}_{hh}) and gust-induced effects (\mathbf{Q}_{hG}).

Generalized aerodynamic forces can be also calculated with nonlinear CFD in the time domain according to the formulation detailed in section 1.1.1. Different harmonic excitations can be imposed as input and the solution in the time domain can be expressed in the frequency domain through a Fourier transformation.

When expressing unsteady aerodynamics in the frequency domain, transfer functions of the generalized displacements can be directly calculated as shown in equation 1.46. From this solution other quantities such as acceleration or integrated loads can be derived [17].

$$\mathbf{u}_h(\omega) = [-\omega^2 \mathbf{M}_{hh} + j\omega \mathbf{B}_{hh} + \mathbf{K}_{hh} - \bar{q}\mathbf{Q}_{hh}]^{-1} \bar{q}\mathbf{Q}_{hG} \mathbf{w}_G(\omega) \quad (1.46)$$

Time Domain

Unsteady aerodynamic forces calculated by CFD-LFD and DLM are expressed in the frequency domain. Time domain solutions can be obtained by different approaches. One of them consists in fitting the frequency data with rational functions. This method is called Rational Function Approximation (RFA). It allows capturing the unsteady flow in the time domain by introducing additional aerodynamic lag states [23]. The gust propagation effect in the time domain can be captured with enough lag states [25] or by combining RFA with explicit delays all along the aircraft [27, 28].

The general form of the rational function approximation is given in equation 1.47. The expression is given in the Laplace domain ($s = jk = j(2\pi f)l_{ref}/V_\infty$, with k being

the reduced frequency, f the frequency, l_{ref} the reference chord length and V_∞ the true air speed) allowing for time domain simulations. The coefficients of the approximation ($\mathbf{F}_0, \mathbf{F}_1, \mathbf{F}_2, \mathbf{F}_{i+2}$) are determined by setting the number (N_d) and the value of the delay parameters (d_i) applying least squares techniques to fit the unsteady aerodynamic forces given for different frequencies. The different coefficients (\mathbf{F}_i) are calculated in order to minimise the criteria set in equation 1.48. Constrained equations can be enforced to match values at specific frequency values through the coefficient G_i . The time domain approximation can be validated by comparing the aerodynamic forces with the ones calculated with DLM or CFD-LFD in the frequency domain as shown in chapter 3.

$$\mathbf{Q}_{RFA}(s) = \mathbf{F}_0 + \frac{\mathbf{F}_1}{V_\infty} s + \frac{\mathbf{F}_2}{V_\infty^2} s^2 + \sum_{i=1}^{N_d} \mathbf{F}_{i+2} \frac{s}{s + V_\infty d_i} \quad (1.47)$$

$$J = \sum_{i=1}^N G_i \|\mathbf{Q}(M, k) - \mathbf{Q}_{RFA}(M, s)\|^2 \quad (1.48)$$

Once the identification of the coefficients ($\mathbf{F}_0, \mathbf{F}_1, \mathbf{F}_2, \mathbf{F}_{i+2}$) is performed for each effect, multiplying equation 1.47 with dynamic pressure (\bar{q}) and the induced effect (modal displacement \mathbf{u}_h or gust \mathbf{w}_G), provides the unsteady aerodynamic force approximated through a rational function approximation given in the Laplace domain:

$$\mathbf{F}_h^u(s) = \bar{q} \left(\mathbf{F}_{hh0} + \frac{\mathbf{F}_{hh1}}{V_\infty} s + \frac{\mathbf{F}_{hh2}}{V_\infty^2} s^2 + \sum_{i=1}^{N_{dh}} \mathbf{F}_{hh(i+2)} \frac{s}{s + V_\infty d_{hi}} \right) \mathbf{u}_h \quad (1.49)$$

$$\mathbf{F}_h^{gust}(s) = \bar{q} \left(\mathbf{F}_{hG0} + \frac{\mathbf{F}_{hG1}}{V_\infty} s + \frac{\mathbf{F}_{hG2}}{V_\infty^2} s^2 + \sum_{i=1}^{N_{dG}} \mathbf{F}_{hG(i+2)} \frac{s}{s + V_\infty d_{Gi}} \right) \mathbf{w}_G \quad (1.50)$$

A Laplace transformation allows expressing the motion (\mathbf{F}_h^u) and gust-induced (\mathbf{F}_h^{gust}) unsteady aerodynamic forces in the time domain as shown in equations 1.51 and 1.52 respectively. The second derivative of the wind input is not considered as it is not always available. The lag states associated with motion (\mathbf{u}_{hi}) and gust (\mathbf{w}_{Gi}) induced unsteady aerodynamic effects in the time domain are given in equations 1.53 and 1.54 respectively.

$$\mathbf{F}_h^u(t) = \bar{q} \left(\mathbf{F}_{hh0} \mathbf{u}_h + \frac{\mathbf{F}_{hh1}}{V_\infty} \dot{\mathbf{u}}_h + \frac{\mathbf{F}_{hh2}}{V_\infty^2} \ddot{\mathbf{u}}_h + \sum_{i=1}^{N_{dh}} \mathbf{F}_{hh(i+2)} \mathbf{u}_{hi} \right) \quad (1.51)$$

$$\mathbf{F}_h^{gust}(t) = \bar{q} \left(\mathbf{F}_{hG0} \mathbf{w}_G + \frac{\mathbf{F}_{hG1}}{V_\infty} \dot{\mathbf{w}}_G + \sum_{i=1}^{N_{dG}} \mathbf{F}_{hG(i+2)} \mathbf{w}_{Gi} \right) \quad (1.52)$$

$$\dot{\mathbf{u}}_{hi} = V_\infty d_{hi} \mathbf{u}_{hi} + \dot{\mathbf{u}}_h \quad (1.53)$$

$$\dot{\mathbf{w}}_{Gi} = V_\infty d_{Gi} \mathbf{w}_{Gi} + \dot{\mathbf{w}}_G \quad (1.54)$$

with V_∞ being the true air speed, d_{hi} and d_{Gi} the value of the delay coefficients chosen for the rational function approximation according to equation 1.47. The number of delay coefficients (N_d) is specified for each case.

1.3.3 State-space Model

From the equations of motion given in section 1.3.1 and the unsteady aerodynamic forces given in the time domain through a rational function approximation as shown in section 1.3.2, it is possible to formulate a state space model which can be used for various aeroservoelastic applications.

The typical structure of a state space model is:

$$\begin{cases} \dot{\mathbf{X}} = \mathbf{A}\mathbf{X} + \mathbf{B}\mathbf{U} \\ \mathbf{Y} = \mathbf{C}\mathbf{X} + \mathbf{D}\mathbf{U} \end{cases} \quad (1.55)$$

with \mathbf{X} being the states of the aircraft, \mathbf{U} the model inputs and \mathbf{Y} the model outputs. \mathbf{A} , \mathbf{B} , \mathbf{C} and \mathbf{D} are matrices determined through the physical relations between states, inputs and outputs.

The states include the modal displacement, its derivative and lag states:

$$\mathbf{X} = [\mathbf{u}_h \quad \dot{\mathbf{u}}_h \quad \mathbf{u}_{hi} \quad \mathbf{w}_{Gi}]^T$$

The considered input are the gust or turbulence and its derivative:

$$\mathbf{U} = [\mathbf{w}_G \quad \dot{\mathbf{w}}_G]^T$$

From these states and inputs and combining equations 1.42, 1.51, 1.52, 1.53 and 1.54 the expressions to calculate the matrices A and B are:

$$\mathbf{A} = \left[\begin{array}{c|c|c|c} 0 & \mathbf{I}_h & 0 & 0 \\ \hline -\mathbf{M}_h^{-1} \mathbf{K}_h & -\mathbf{M}_h^{-1} \mathbf{B}_h & \bar{q} \mathbf{M}_h^{-1} [\mathbf{F}_{hh(i+2)}]_i & \bar{q} \mathbf{M}_h^{-1} [\mathbf{F}_{hG(i+2)}]_i \\ \hline 0 & \mathbf{I}_h & \ddots & 0 \\ & \vdots & & \\ 0 & \mathbf{I}_h & 0 & \ddots \\ \hline 0 & 0 & 0 & \ddots \\ & & & V_\infty (d_{Gi} \mathbf{I}_G) \\ & & & 0 \\ & & & \ddots \end{array} \right]$$

$$\begin{aligned} \mathbf{K}_h &= \mathbf{K}_{hh} - \bar{q}\mathbf{F}_{hh0} & \mathbf{B}_h &= \mathbf{B}_{hh} - \bar{q}\frac{\mathbf{F}_{hh1}}{V_\infty} & \mathbf{M}_h &= \mathbf{M}_{hh} - \bar{q}\frac{\mathbf{F}_{hh2}}{V_\infty^2} \\ \mathbf{M}_0^{gust} &= \bar{q}\mathbf{M}_h^{-1}\mathbf{F}_{hG0} & \mathbf{M}_1^{gust} &= \frac{\bar{q}}{V_\infty}\mathbf{M}_h^{-1}\mathbf{F}_{hG1} \end{aligned}$$

$$\mathbf{B} = \left[\begin{array}{c|c} 0 & 0 \\ \hline \mathbf{M}_0^{gust} & \mathbf{M}_1^{gust} \\ \hline 0 & 0 \\ \hline & \mathbf{I}_G \\ & \vdots \\ & \mathbf{I}_G \end{array} \right]$$

with \mathbf{I}_h and \mathbf{I}_G being the identity matrix of the dimension of the number of generalized coordinates and gust or turbulence inputs respectively.

Matrices \mathbf{C} and \mathbf{D} are not detailed as they depend on the chosen outputs. In the present work, the aeroelastic model is not used to compute specific outputs. The interest of the model is the possibility to take into account certain model states when simulating the aircraft response due to gust and turbulence. Further details are given in chapter 2. Additional details about the model and possible applications can be found in [38, 40].

Chapter 2

Integrated Aircraft Model

In this chapter, the strategy and different aspects to consider when integrating the previously detailed equations of motion and aerodynamic models are included. The main objective of the approach is to capture relevant physics when simulating the aircraft response due to different atmospheric disturbances. Results of the proposed strategy when simulating the aircraft response due to different gust and turbulence effects are given in chapters 3 and 4. The modelling assumptions and equations of motion of the integrated approach are presented as well as the details on how the gust-induced and dynamic flexible effect are taken into account.

2.1 Modelling Assumptions

The integrated model is build based on a series of modelling assumptions which define its range of applicability. This part contains all the different modelling assumptions that have been adopted. Similar assumptions than the ones done in [27] and [38] have been made and are based on current passenger aircraft configurations. For unconventional designs, some of them should be revised and the strategy could be adapted. The main assumptions are:

- The Earth rotation is neglected and the geodetic reference frame is assumed to be inertial.
- Gravity defined according to this reference system is constant.
- The structure can be divided in a collection of lumped masses.
- Elastic deformations with respect to the reference shape are small allowing the application of linear elastic theory.

- The aircraft deformation can be written as a linear combination of modal shapes, which are available from a free-free modal analysis and are orthogonal.
- The quasi-static flexible effects captured in the flight dynamics response are equivalent to the statically residualized aerodynamic forces used to calculate the aeroelastic response (further details are given in section 2.4).
- The inertia tensor of the aircraft is constant, which involves that inertia forces act in the deformed reference condition assumed to be constant during the simulation.
- The inertial cross coupling between the overall aircraft motion and elastic deformation is small and can be neglected.

The last two assumptions were not considered and the inertial coupling between the rigid and flexible motions was taken into account in [34] for a generic current passenger aircraft configuration. The effects of considering an inertially coupled formulation on the flight mechanic states were found to be small and can be neglected. One of the most important effect of the inertial coupling is detected in components with a high concentrated mass, such as the engines.

2.2 Equations of Motion

The equations of motion of the integrated approach based on the previous modelling assumptions are given in this part. The set of equations are formulated in the time domain. It can be shown according to [31] that a set of nonlinear equations of motion of a flexible aircraft in the time domain can be obtained through the combination of equations 1.23 and 1.24 to capture the flight dynamics response and 1.42 to account for flexible deformations.

One of the overlaps when combining these two equations of motion is that the rigid motion is calculated in both cases. Equations 1.23 and 1.24 are used to solve the flight dynamics response in order to account for large nonlinear aircraft motions. The linear elastic generalized equations of motion 1.42 are used to solve the flexible motion by limiting the modal contribution to the flexible degrees of freedom ($u_h = u_e$).

The second overlap that needs to be considered is that the quasi-steady aerodynamics model presented in section 1.2.2 and used to capture the flight dynamics response takes into account quasi-static flexibility. These effects are also included when calculating the flexible deformation according to equation 1.42. This overlap is solved through the residualized model approach and is described in section 2.4.

The predicted aircraft response using the integration of these equations of motion is expressed relative to a mean body axis reference frame, which captures the mean motion of the airframe [31, 64]. It is oriented and positioned according to constraints of minimum

relative momentum of flexible deformation with respect to these axes, avoiding the inertial coupling between rigid and flexible motion. These constraints are nonlinear and difficult to satisfy. However, the linearized form is adopted which is also called practical mean axis constraints. The free-free vibration modes obtained through a modal analysis automatically fulfil these linearized constraints. A body reference frame positioned with its origin at the centre of gravity of the deformed aircraft and oriented according to the directions of the translational rigid body modes, satisfies the linearized mean axis constraints [38]. This occurs due to the orthogonality of the rigid modes with respect to the flexible modes obtained from a modal analysis. This can be seen with the generalized mass (\mathbf{M}_{hh}) and stiffness (\mathbf{K}_{hh}) matrices from equation 1.42, in which the off-diagonal terms are zero. The rigid body modes can be expressed with respect to the body reference frame without affecting this orthogonality. The body reference frame, as the one presented in section 1.2 to express the flight dynamics equations of motion, can be seen as a mean axes reference frame describing the mean overall motion of the aircraft. Additional details about the practical mean axes constraints can be found in [34].

According to the last two assumptions presented in section 2.1 and the mean body axes reference frame, the coupling between rigid and flexible motion only occurs through the external forces. In particular, through the unsteady motion-induced aerodynamic forces and moments. Additional details about this coupling are given in section 2.4.

The set of nonlinear equations of motion of a flexible aircraft are given in equations 2.1, 2.2 and 2.3, with $\Delta \mathbf{F}_b^{gust}$ and $\Delta \mathbf{M}_b^{gust}$ being the force and moment contribution of gust induced effect on flight dynamics expressed in the time domain and in the body axes reference frame. The dynamic flexible effect on flight dynamics expressed in body axes is also included with the terms $\Delta \mathbf{F}_b^{flex}$ and $\Delta \mathbf{M}_b^{flex}$. Details on how these dynamic effects due to gust or turbulence and structural deformation are calculated are given in sections 2.3 and 2.4.

$$m(\dot{\mathbf{V}}_b + \boldsymbol{\Omega}_b \times \mathbf{V}_b - \mathbf{T}_{bE} \mathbf{G}_E) = \mathbf{F}_b + \Delta \mathbf{F}_b^{gust} + \Delta \mathbf{F}_b^{flex} \quad (2.1)$$

$$\mathbf{J}_b \dot{\boldsymbol{\Omega}}_b + \boldsymbol{\Omega}_b \times \mathbf{J}_b \boldsymbol{\Omega}_b = \mathbf{M}_b + \Delta \mathbf{M}_b^{gust} + \Delta \mathbf{M}_b^{flex} \quad (2.2)$$

$$\mathbf{M}_{ee} \ddot{\mathbf{u}}_e(t) + \mathbf{B}_{ee} \dot{\mathbf{u}}_e(t) + \mathbf{K}_{ee} \mathbf{u}_e(t) = \boldsymbol{\phi}_{ge}^T \mathbf{F}_g(t) \quad (2.3)$$

Figure 2.1 shows the integration approach to combine nonlinear flight mechanics and linear aeroelastic equations of motion. The aspects to consider when integrating a quasi-steady flexible and unsteady aerodynamics model to account for gust-induced and motion induced forces are described in sections 2.3 and 2.4. Some of the unsteady aerodynamic effects due to rigid body motion are included in the quasi-steady aerodynamics model through coefficients such as $Cz_{\dot{\alpha}}$ as described in section 1.2.2. Aerodynamic forces and moments due to the the aircraft response and control surface deflection are calculated

through the quasi-steady flexible aerodynamics model. In the present analysis, flexible deformation due to the gust or turbulence excitation is the main contribution to the motion-induced unsteady aerodynamic forces in the aeroelastic equations of motion ($\mathbf{F}_h^u = \mathbf{F}_e^u$). The rigid body motion effect on the dynamic flexibility motion is found to be less important than the gust contribution and is not taken into account in this work. However, it could also be added as demonstrated in [38]. If dynamic flexible effects can be neglected, the aeroelastic linear equations of motion can be omitted and the unsteady contribution only accounts for the gust induced effect ($\Delta \mathbf{F}_b^{gust}$, $\Delta \mathbf{M}_b^{gust}$). The impact of dynamic flexibility on the response is assessed in chapter 3.

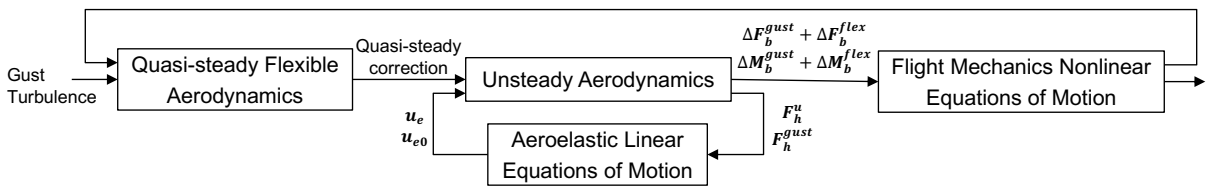


Figure 2.1: Integration approach between nonlinear flight dynamics and linear aeroelastic equations of motion

2.3 Gust-induced Effect

This section focuses on the gust induced effect and how its contribution can be taken into account in the integrated model approach. Different possibilities exist in order to express the gust excitation. In this section, a consistent gust input in the time domain is defined between the quasi-steady flexible aerodynamics and unsteady aerodynamics model used to calculate the flight dynamics and aeroelastic response respectively.

The rational function approximation presented in section 1.3.2 is considered through equations 1.52 and 1.54 to express the gust-induced unsteady aerodynamic forces in the time domain. The model can be built by identifying the RFA coefficients from DLM as well as CFD simulations in the frequency domain, as shown in chapter 3.

When the analysis is focused on the low frequency range, it is possible to approximate the effect in a single point with a reduced number of additional aerodynamic states, also referred to as lag states. This allows the identification of aerodynamic derivatives that capture the gust effect, such as $Cz_{\dot{\alpha}_G}$, as proposed in [10]. These gust-induced aerodynamic derivatives can be extracted from the rational function approximation obtained through DLM or CFD simulations. Another possibility is the estimation of these coefficients from analytical expressions involving geometrical parameters and quasi-steady aerodynamic coefficients by making some assumptions. Section 2.3.1 includes the derivation and form of

the model that can be either identified from aerodynamic simulations or estimated through analytical expressions.

A possible variation of the adopted approach in the present work is proposed in [27]. It is assumed that the gust effect creates the same downwash as the one induced by the aircraft motion. The only difference is that the downwash associated with the gust effect is delayed along the aircraft in order to account for the gust propagation effect. This is shown in equation 2.4, with $\mathbf{x}_{Gj}(t) = \mathbf{x}_j - V_\infty t$, being \mathbf{x}_j the different coordinates of the aerodynamic grid and V_∞ the true airspeed of the aircraft assuming that the gust profile is not moving.

$$\mathbf{w}_{Gj}(t) = \mathbf{w}_{Gj}(\mathbf{x}_{Gj}(t)) \quad (2.4)$$

The gust-induced force expressed in the time domain takes then the form given in equation 2.5 and 2.6. The rational function approximation is directly applied in physical coordinates and projected from the aerodynamic (j) to the structural grid (g). This enables a clear separation between a quasi-steady and unsteady contribution. The expression only depends on the Mach number and is not tied to mass case for the motion-induced forces as the expression in generalized form. However, it requires a quasi-steady aerodynamic model with distributed coefficients all along the aircraft.

$$\mathbf{F}_g^{gust}(t) = \bar{q} \left(\mathbf{F}_{gj0} \mathbf{w}_{Gj} + \frac{\mathbf{F}_{gj1}}{V_\infty} \dot{\mathbf{w}}_{Gj} + \sum_{i=1}^{N_d} \mathbf{F}_{gj(i+2)} \mathbf{w}_{Gi} \right) \quad (2.5)$$

$$\dot{\mathbf{w}}_{Gi} = V_\infty d_{Gi} \mathbf{w}_{Gi} + \dot{\mathbf{w}}_{Gj} \quad (2.6)$$

Another possibility consists of dividing the aircraft in sections as proposed in [28]. A rational function approximation can then be calculated for each section. Different gust inputs delayed for each section are then taken into account, instead of evaluating the gust input over the aerodynamic grid. The propagation time delay is set according to the distance between sections and the aircraft speed.

The use of explicit delays might create difficulties in some simulation environments and applications. Another possibility proposed in [26] consists on approximating the time delays by filters. The first order approximation of a pure time delay in the Laplace domain can be expressed as: $e^{Ts} \approx \frac{1}{1+Ts}$

2.3.1 Aerodynamic Derivatives

As mentioned previously, when the analysis is focused on low frequencies, there is the possibility to reduce the states of the model by keeping a low number of lag states of the rationalisation. This allows the derivation of dynamic gust-induced coefficients which can

be extracted to capture the main effects. These coefficients can be identified directly from DLM and CFD simulations as shown in chapter 3 or estimated from physical relations.

The derivation of the lift and side-force unsteady aerodynamic derivatives due to vertical and lateral gusts respectively are presented in this section, according to a similar strategy proposed in [10]. The gust-induced aerodynamic derivative holds for symmetrical one-dimensional vertical or lateral gust. For the derivation, it is assumed that the position of the aerodynamic center of the wing and the center of gravity coincide.

Vertical Response

A discrete symmetrical vertical gust is considered $\alpha_G = \frac{w_{zG}}{V_\infty}$. The gust disturbance reaches the nose initially before the wing and finally the Horizontal Tail Plane (HTP). When reaching the wing, the gust induces a variation of angle of attack which modifies the wing downwash (ε) that is seen by the HTP after a certain time. This propagation time is given by $\tau_{w/H} = \frac{l_{w/H}}{V_\infty}$, with $l_{w/H}$ as the length between the wing aerodynamic center and the HTP and V_∞ as the aircraft true airspeed. The downwash effect modifies the angle of attack seen by the HTP creating an increment of aerodynamic force in addition to the gust contribution. The lag effect of the downwash on the HTP due to an angle of attack variation at the wing can be captured through the $C_{z\dot{\alpha}}$ coefficient.

The angle of attack variation due to the gust reaches the HTP after the same propagation time as the downwash from the wing. When the gust is measured at the aircraft nose, the propagation time ($\tau_{n/H}$) takes into account the distance from the aircraft nose to the HTP ($l_{n/H}$). The gust-induced effect is not considered in the $C_{z\dot{\alpha}}$ coefficient and it can be captured by an additional term which is derived in this section. The gust induced coefficient includes both the lag associated with the gust propagation as well as the wing downwash induced by the gust effect. Figure 2.2 illustrates the gust effect at different parts of the aircraft as well as the downwash seen by the HTP due to the angle of attack variation at the wing caused by the gust. According to figure 2.2, the aircraft can be divided in different sections such as nose (forward fuselage section), wing and HTP. Additional aerodynamic effects due to interference between different parts are not included.

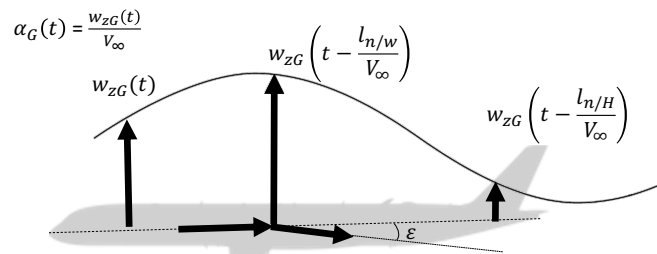


Figure 2.2: Illustration vertical gust effect and downwash on the aircraft

Aerodynamic stiffness terms are considered for each part making the assumption of quasi-steady aerodynamics in each section ($Cz_{\alpha n}$, $Cz_{\alpha w}$, $Cz_{\alpha H}$). The lift force can be expressed by considering the different contributions :

$$F_z^{gust}(t) = \bar{q}S_{ref}Cz_{\alpha n}\alpha_n(t) + \bar{q}S_{ref}Cz_{\alpha w}\alpha_w(t) + \bar{q}_H S_H Cz_{\alpha H}\alpha_H(t) \quad (2.7)$$

The lift force coefficient can be derived from the previous expression through the appropriate nondimensionalized parameters (dynamic pressure \bar{q} and reference surface S_{ref}):

$$C_z^{gust}(t) = \frac{F_z^{gust}(t)}{\bar{q}S_{ref}} \quad (2.8)$$

$$C_z^{gust}(t) = Cz_{\alpha n}\alpha_n(t) + Cz_{\alpha w}\alpha_w(t) + Cz_{\alpha H}\frac{V_H^2}{V_\infty^2}\frac{S_H}{S_{ref}}\alpha_H(t) \quad (2.9)$$

The variation of angle of attack due to the gust excitation is expressed in the frequency domain ($\alpha_G(\omega)$). The angle of attack seen at each section can be delayed with the appropriate propagation time, taken the aircraft nose as the reference point where the gust is measured. Then, an explicit delay is not required to express the angle of attack at the aircraft nose: $\alpha_n(\omega) = \alpha_G(\omega)$

The angle of attack seen by the wing section is the same as the one measured at the nose delayed by time it takes the gust to propagate from the nose to the wing ($\tau_{n/w}$). This time is given by the distance between both sections ($l_{n/w}$) and the aircraft true airspeed (V_∞). The downwash effect of the front part of the fuselage to the wing is neglected. The angle of attack variation at the wing due to a vertical gust excitation can be expressed in the frequency domain as: $\alpha_w(\omega) = \alpha_G(\omega)e^{-j\omega\tau_{n/w}} = \alpha_G(\omega)e^{-j\omega\frac{l_{n/w}}{V_\infty}}$

The angle of attack seen by the HTP is the same as the one seen at the nose delayed by the time it takes the excitation to reach the HTP from the nose ($\tau_{n/H}$). As presented previously, the downwash variation at the wing due to the variation of angle of attack has an effect on the HTP. In this case, the propagation time is the one it takes the downwash from the wing to the HTP ($\tau_{w/H}$). However, the propagation time from the nose, where the gust is measured, to the wing also needs to be added, as the downwash is created once the gust reaches the wing ($\tau_{n/H} = \tau_{n/w} + \tau_{w/H}$). The propagation time from the nose to the HTP is considered for both effects and it can be defined through the distance between both parts ($l_{n/H}$). It is assumed that the effect of the downwash on the HTP is only induced by the wing which is the main contribution. The downwash angle (ε) created due to angle of attack variation at the wing (α_0) can be expressed as $\varepsilon = \frac{\partial\varepsilon}{\partial\alpha}\alpha_0$. The angle of attack variation at the HTP due to a vertical gust excitation can then be defined as: $\alpha_H(\omega) = \alpha_G(\omega)e^{-j\omega\tau_{n/H}} - \alpha_w(\omega)\frac{\partial\varepsilon}{\partial\alpha}e^{-j\omega\tau_{w/H}} = \alpha_G(\omega)e^{-j\omega\tau_{n/H}} - \alpha_G(\omega)\frac{\partial\varepsilon}{\partial\alpha}e^{-j\omega(\tau_{n/w}+\tau_{w/H})} = \alpha_G(\omega)e^{-j\omega\frac{l_{n/H}}{V_\infty}}\left(1 - \frac{\partial\varepsilon}{\partial\alpha}\right)$

The increment of lift force coefficient due to the gust excitation can be expressed as:

$$C_z^{gust}(\omega) = Cz_{\alpha n}\alpha_G + Cz_{\alpha w}e^{-j\omega\frac{l_n/w}{V_\infty}}\alpha_G + Cz_{\alpha H}\frac{V_H^2}{V_\infty^2}\frac{S_H}{S_{ref}}e^{-j\omega\frac{l_n/H}{V_\infty}}\left(1 - \frac{\partial\varepsilon}{\partial\alpha}\right)\alpha_G(\omega) \quad (2.10)$$

When dividing the increment of lift force coefficient by the gust input, the so-called Frequency Response Function (FRF) is obtained:

$$\frac{C_z^{gust}(\omega)}{\alpha_G(\omega)} = Cz_{\alpha n} + Cz_{\alpha w}e^{-j\omega\frac{l_n/w}{V_\infty}} + Cz_{\alpha H}\frac{V_H^2}{V_\infty^2}\frac{S_H}{S_{ref}}e^{-j\omega\frac{l_n/H}{V_\infty}}\left(1 - \frac{\partial\varepsilon}{\partial\alpha}\right) \quad (2.11)$$

A first order Taylor polynomial approximation can be used to express the time delay: $e^{-j\omega\tau_{A/B}} \approx 1 - j\omega\tau_{A/B}$

The aerodynamic frequency response function can then be expressed as:

$$\frac{C_z^{gust}(\omega)}{\alpha_G(\omega)} = Cz_{\alpha n} + Cz_{\alpha w}\left(1 - j\omega\frac{l_n/w}{V_\infty}\right) + Cz_{\alpha H}\frac{V_H^2}{V_\infty^2}\frac{S_H}{S_{ref}}\left(1 - j\omega\frac{l_n/H}{V_\infty}\right)\left(1 - \frac{\partial\varepsilon}{\partial\alpha}\right) = \quad (2.12)$$

$$= \underbrace{\left[Cz_{\alpha n} + Cz_{\alpha w} + Cz_{\alpha H}\frac{V_H^2}{V_\infty^2}\frac{S_H}{S_{ref}}\left(1 - \frac{\partial\varepsilon}{\partial\alpha}\right) \right]}_{Cz_\alpha} + \underbrace{\left[-Cz_{\alpha w}\frac{l_n/w}{l_{ref}} - Cz_{\alpha H}\frac{V_H^2}{V_\infty^2}\frac{S_H}{S_{ref}}\left(1 - \frac{\partial\varepsilon}{\partial\alpha}\right)\frac{l_n/H}{l_{ref}} \right]}_{Cz_{\dot{\alpha}_G}}\frac{l_{ref}}{V_\infty}j\omega$$

From expression 2.12, it can be concluded that the gust-induced effect on the aircraft lift response can be predicted as a first-order approximation through the quasi-steady lift coefficient due to an angle of attack variation (Cz_α) and an additional dynamic term ($Cz_{\dot{\alpha}_G}$) that can be estimated from quasi-steady aerodynamic derivatives as well as geometrical parameters. This estimation is limited to low frequency gust excitations as the propagation delay has been approximated with a first-order function.

A similar expression can be obtained for the pitching moment coefficient (Cm). The centre of gravity effect in pitch is taken into account through the lever arm from the aerodynamic centre (x_0) to the centre of gravity position (x_{cg}): $Cm = Cm_0 + (x_{cg} - x_0)Cz$, with Cm_0 being the pitching moment coefficient calculated at the aerodynamic centre.

The dynamic gust-induced derivatives ($Cz_{\dot{\alpha}_G}$ and $Cm_{\dot{\alpha}_G}$) can be also identified from the rational function approximation (detailed in section 1.3.2) calculated from DLM or CFD unsteady simulations. The identification of the coefficient from aerodynamic simulation

methods is more accurate than the analytical estimation as shown in [10]. However, the analytical form can provide an order of magnitude of the effect in early design phases as well as validation means to compare with the aerodynamic simulation approach.

In some cases, the rational function approximation may contain lag terms as detailed in section 1.3.2. An identification approach to create a model with aerodynamic coefficients from a RFA with lag states is also possible, increasing the accuracy in the prediction at higher gust frequencies. The terms associated with the lag states can be added in a model with aerodynamic coefficients. An example is presented with a rational function approximation with one lag term (the number of additional delay states of the RFA in equation 1.52 N_{dG} is set to 1), given by the expression in equation 2.13.

$$\mathbf{F}_h^{gust}(s) = \bar{q} \left(\mathbf{F}_{hG0} + \frac{\mathbf{F}_{hG1}}{V_\infty} s + \mathbf{F}_{hG3} \frac{s}{s + V_\infty d_{Gi}} \right) \mathbf{w}_G \quad (2.13)$$

Ignoring the second order terms, equation 2.13 can be rearranged as follows:

$$\mathbf{F}_h^{gust}(s) = \bar{q} \mathbf{F}_{hG0} \mathbf{w}_G + \bar{q} \frac{\frac{\mathbf{F}_{hG1}}{V_\infty} + \frac{\mathbf{F}_{hG3}}{V_\infty d_{Gi}}}{1 + \frac{s}{V_\infty d_{Gi}}} \dot{\mathbf{w}}_G \quad (2.14)$$

A first order filter can be added to the dynamic gust-induced effect and the different terms can be identified from the rational function approximation (equation 2.14):

$$\Delta C_z^{gust} = C_{z\alpha} \alpha_G + \frac{C_{z\dot{\alpha}_G} \frac{l_{ref}}{V_\infty}}{1 + \tau_G s} \dot{\alpha}_G \quad (2.15)$$

This model captures the gust propagation as well as unsteady aerodynamic effects at low frequencies. When simulating the aircraft response to higher frequencies, additional lag states are required and filters of higher order can be added to the model. This model is meant to cover the low frequency range for flight dynamics investigations. At high frequencies, the aircraft react less to atmospheric disturbances but there are cases of interest in gust loads analysis for structural sizing. The model identification from linearized CFD simulation results in the frequency domain is shown in chapter 3 in order to express the gust-induced effects in the time domain.

Another possibility to increase the accuracy of the prediction by keeping a low number of additional aerodynamic states consists of adding an explicit delay. Adding explicit delays has been previously proposed to reduce the number of required states of the rational function approximation [25, 26, 28]. Instead of approximating the whole delay effect due to the gust propagation with a first order filter creating an additional state, the approach captures part of this time lag with an explicit delay.

Equation 2.16 shows the identified model from a rational function approximation with an explicit delay, which is defined by the distance between two aircraft parts ($l_{A/B}$) and

the true airspeed (V_∞). In lift, an explicit delay from the nose to the wing is a valid option as the wing is the main contribution in lift. The same optimization problem as the one set in section 1.3.2 can be used to set the most appropriate point ($A - B$) for each degree of freedom to minimise the number of required additional aerodynamic lag stages according to the criteria in equation 1.48.

$$\Delta C_z^{gust} = \exp\left(-\frac{l_{A/B}}{V_\infty}s\right) C_{z\alpha} \alpha_G + \frac{C_{z\dot{\alpha}_G} \frac{l_{ref}}{V_\infty}}{1 + \tau_G s} \dot{\alpha}_G \quad (2.16)$$

Lateral Response

The same derivation can be done in lateral for the side-force coefficient. In this case, the gust excitation can be seen as a variation of the sideslip (β_G). As the main contribution to side-force is the Vertical Tail Plane (VTP), the wing and fuselage contribution are considered in the same section. The sideslip variation at the wing creates a sidewash (σ) that reaches the VTP after the propagation time $\tau_{w/V} = \frac{l_{w/V}}{V_\infty}$. This sidewash creates an aerodynamic force on the VTP in addition to the lateral gust effect. The sideslip variation at the VTP ($\beta_V = -(\beta - \sigma)$) due to the lateral gust reaches the VTP from the wing after the same propagation time ($\tau_{w/V}$). Figure 2.3 illustrates the lateral gust effect as well as the sidewash seen by the VTP due to the sideslip variation at the wing induced by the gust.

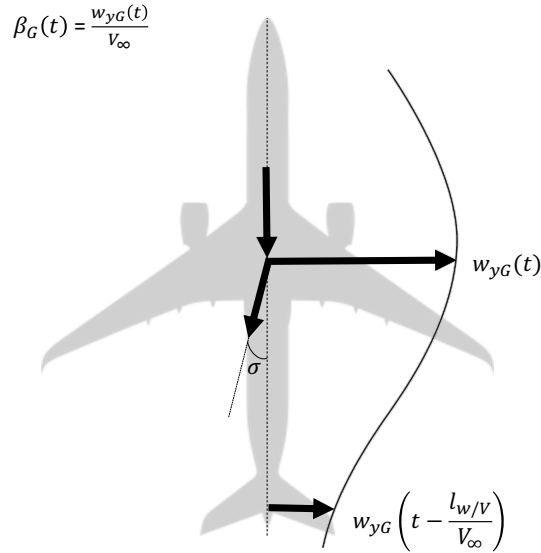


Figure 2.3: Illustration lateral gust effect and sidewash on the aircraft

The sideforce given in aerodynamic axes can be written as:

$$F_y^{gust}(t) = \bar{q}S_{ref}C_{y_{\beta w}}\beta_w(t) + \bar{q}V_S C_{y_{\beta V}}\beta_V(t) \quad (2.17)$$

The sideforce coefficient can be also defined from nondimensionalized coefficients as:

$$C_y^{gust}(t) = \frac{F_y^{gust}(t)}{\bar{q}S_{ref}} \quad (2.18)$$

$$C_y^{gust}(t) = C_{y_{\beta w}}\beta_w(t) + C_{y_{\beta V}}\frac{V_V^2}{V_\infty^2}\frac{S_V}{S_{ref}}\beta_V(t) \quad (2.19)$$

The sideslip variation for the wing and fuselage section is also expressed in the frequency domain: $\beta_w(\omega) = \beta_G(\omega)$

An explicit delay is added to account for the gust propagation effect on the VTP. The sidewash (σ) effect due to a sideslip variation (β_0) is also taken into account ($\sigma = \frac{\partial\sigma}{\partial\beta}\beta_0$). The sideslip variation due to the lateral gust at the VTP is expressed in the frequency domain as: $\beta_V(\omega) = -e^{-j\omega\tau_w/V}\beta_G(\omega) + \frac{\partial\sigma}{\partial\beta}e^{-j\omega\tau_w/V}\beta_G(\omega) = -\left(1 - \frac{\partial\sigma}{\partial\beta}\right)e^{-j\omega\frac{l_w/V}{V_\infty}}\beta_G(\omega)$

The sideforce coefficient is then formulated in the frequency domain as:

$$C_y^{gust}(\omega) = C_{y_{\beta w}}\beta_G - C_{y_{\beta V}}\frac{V_V^2}{V_\infty^2}\frac{S_V}{S_{ref}}\left(1 - \frac{\partial\sigma}{\partial\beta}\right)e^{-j\omega\frac{l_w/V}{V_\infty}}\beta_G(\omega) \quad (2.20)$$

The Frequency Response Function (FRF) can be also defined in lateral dividing by the variation of sideslip due to the lateral gust:

$$\frac{C_y^{gust}(\omega)}{\beta_G(\omega)} = C_{y_{\beta w}} - C_{y_{\beta V}}\frac{V_V^2}{V_\infty^2}\frac{S_V}{S_{ref}}\left(1 - \frac{\partial\sigma}{\partial\beta}\right)e^{-j\omega\frac{l_w/V}{V_\infty}} \quad (2.21)$$

A first order Taylor polynomial approximation is used to express the time delay ($e^{-j\omega\tau_{A/B}} \approx 1 - j\omega\tau_{A/B}$) as for the derivation of the vertical gust-induced effect. The sideforce frequency response function is then expressed as:

$$\begin{aligned} \frac{C_y^{gust}(\omega)}{\beta_G(\omega)} &= C_{y_{\beta w}} - C_{y_{\beta V}}\frac{V_V^2}{V_\infty^2}\frac{S_V}{S_{ref}}\left(1 - \frac{\partial\sigma}{\partial\beta}\right)\left(1 - j\omega\frac{l_w/V}{V_\infty}\right) = \\ &= \underbrace{\left[C_{y_{\beta w}} - C_{y_{\beta V}}\frac{V_V^2}{V_\infty^2}\frac{S_V}{S_{ref}}\left(1 - \frac{\partial\sigma}{\partial\beta}\right)\right]}_{C_{y_\beta}} + \\ &+ \underbrace{\left[C_{y_{\beta V}}\frac{V_V^2}{V_\infty^2}\frac{S_V}{S_{ref}}\left(1 - \frac{\partial\sigma}{\partial\beta}\right)\frac{l_w/V}{l_{ref}}\right]}_{C_{y_{\beta_G}}}\frac{l_{ref}}{V_\infty}j\omega \end{aligned} \quad (2.22)$$

The lateral gust-induced effect on the aircraft response can be also estimated through a quasi-steady coefficient due to variations in sideslip (Cy_β) and an additional gust dynamic term ($Cy_{\dot{\beta}_G}$). The wing and fuselage contributions could be also divided in the derivation obtaining a similar expression as the one for lift previously.

A similar identification process as the one shown in the previous section in vertical can be applied. Lateral dynamic gust coefficients ($Cy_{\dot{\beta}_G}$, $Cl_{\dot{\beta}_G}$ and $Cn_{\dot{\beta}_G}$) can be derived from a rational function approximation with a reduced number of delay coefficients such as the one shown in equation 2.13. Rolling and yawing moment coefficients due to lateral gust need to consider as well the centre of gravity effect as in pitch. Additional details about the centre of gravity effect are provided in chapter 3. An explicit delay can also be added to the identified model. The model identification from CFD simulation results in the frequency domain is shown in chapter 3.

2.3.2 Quasi-steady Correction

Gust-induced unsteady aerodynamic forces, predicted by DLM or CFD and projected to the rigid body modes, need to be consistent with the quasi-steady flexible aerodynamics model at low frequencies. As both aerodynamic models may be generated or corrected with data from different sources (aerodynamic simulations, wind tunnel or flight test), predicted responses at low frequencies may be different. Different strategies to perform this so-called quasi-steady correction are possible.

The gust or turbulence excitation at low frequencies can be seen as a constant angle of attack variation (α) all along the aircraft. This condition depends on the gust wavelength which needs to be high enough with respect to the aircraft characteristic length. Unsteady aerodynamic effects appear at fast variation of angle of attack. Both effects can be physically evaluated through the reduced frequency (k) defined in equation 1.6, which includes the influence of the aircraft speed. Aerodynamic quasi-steady responses are obtained at low reduced frequencies. For a given aircraft speed, the predicted response to a low frequency angle of attack or sideslip variation from the unsteady aerodynamic model needs to be the same as the one predicted by the quasi-steady aerodynamics model. This involves correcting the low frequency range to match the quasi-steady aerodynamic coefficients. This correction allows taking into account quasi-static flexible effects which are already included in the aerodynamic coefficients. The nonlinear dependence of these coefficients with the angle of attack, which is modified by the gust and turbulence contribution, can be also taken into account at low frequencies. A weighting factor is applied in order to ensure the consistency in a similar way as proposed in [25].

An example is shown below for the lift force coefficient. Given a low frequency angle of attack variation that could come from a gust disturbance ($\alpha = \alpha_G$, with $\dot{\alpha}_G \approx 0$), the predicted lift force coefficient by a quasi-steady flexible aerodynamic model linearized

around the steady state and the unsteady aerodynamic model in the time domain is shown in equations 2.23 and 2.24 respectively.

$$C_z^{QS} = \frac{F_z^{QS}}{\bar{q}S_{ref}} = C_{z\alpha}\alpha \quad (2.23)$$

$$C_z^{uns} = \frac{F_z^{uns}}{\bar{q}S_{ref}} = \frac{V_\infty}{S_{ref}} F_{zG0}\alpha \quad (2.24)$$

A weighting function in lift is defined according to the ratio $\frac{C_z^{QS}}{C_z^{uns}}$. This can be used to adjust the gust-induced effect coming from DLM or CFD in order to keep consistency at low frequencies with the quasi-steady flexible aerodynamics model. This correction is meant to be valid at low frequencies.

Once corrected, the increment of aerodynamic force and moment in the time domain due to a vertical (α_G) and lateral (β_G) atmospheric disturbance is expressed in equations 2.25 and 2.26, respectively. As previously detailed, there is also the possibility to add additional lag states with higher order filters or keep one lag state and add an explicit delay to the model. The identification of the model from CFD simulation results in the frequency domain according to section 1.3.2 is shown in chapter 3.

$$\Delta \mathbf{F}_b^{gust} = \bar{q}S_{ref} \begin{bmatrix} C_{y\beta}\beta_G + C_{y\dot{\beta}_G} \frac{l_{ref}/V_\infty}{1+\tau_{Gy}s} \dot{\beta}_G \\ C_{z\alpha}\alpha_G + C_{z\dot{\alpha}_G} \frac{l_{ref}/V_\infty}{1+\tau_{Gz}s} \dot{\alpha}_G \end{bmatrix} \quad (2.25)$$

$$\Delta \mathbf{M}_b^{gust} = \bar{q}S_{ref}l_{ref} \begin{bmatrix} C_{l\beta}\beta_G + C_{l\dot{\beta}_G} \frac{l_{ref}/V_\infty}{1+\tau_{Gl}s} \dot{\beta}_G \\ C_{m\alpha}\alpha_G + C_{m\dot{\alpha}_G} \frac{l_{ref}/V_\infty}{1+\tau_{Gm}s} \dot{\alpha}_G \\ C_{n\beta}\beta_G + C_{n\dot{\beta}_G} \frac{l_{ref}/V_\infty}{1+\tau_{Gn}s} \dot{\beta}_G \end{bmatrix} \quad (2.26)$$

The dependency of this model on the Mach number can be taken into account. The quasi-steady flexible aerodynamics model used in the nonlinear simulation considers Mach variations. The unsteady gust-induced aerodynamic forces are calculated at a given Mach number. The recommended approach in [38] is to develop an interpolation between different rational function approximations at different Mach numbers to capture the Mach effect. This approach and further details on the Mach effect are given in section 3.5.

2.4 Dynamic Flexibility Effect

In some cases, when simulating the aircraft response due to gust and turbulence, dynamic flexible effects may be relevant. When using the equations of motion with a quasi-steady

flexible aerodynamics model, dynamic flexible effects are not taken into account. The integrated approach described in this chapter offers the possibility to include these effects when analysing the aircraft response in such cases $(\Delta \mathbf{F}_b^{flex}, \Delta \mathbf{M}_b^{flex})$.

When taking into account the flexible contribution, the integration approach needs to deal with another overlap as presented in section 2.2. Quasi-steady flexible effects are considered both in the aerodynamic forces calculated through a quasi-steady aerodynamics model as presented in section 1.2.2 as well as through the flexible motion (\mathbf{u}_e) solved with the aeroelastic equations of motion 2.3. The technique used to solve this overlap is called residualized model approach and is detailed in this section.

2.4.1 Residualized Model Approach

The overlap in terms of quasi-static deformation taken into account both in the quasi-steady flexible aerodynamics model as well as through the aeroelastic modal deformation is solved by making one of the assumptions mentioned in section 2.1. The quasi-static flexible effects captured in the flight dynamics response are assumed to be equivalent to the statically residualized aerodynamic forces used to calculate the aeroelastic response. The quasi-steady flexible aerodynamics model is created from CFD simulations and can be corrected from wind tunnel as well as flight test. Therefore, it is interesting to keep the quasi-static flexible effect captured in the identified quasi-steady flexible aerodynamic model and remove the predicted effect from the aeroelastic equations of motion. Then, the quasi-static flexible contribution (\mathbf{u}_{e0}) can be computed and subtracted from the unsteady motion-induced forces of the flexible degrees of freedom. This contribution is found by residualizing the aeroelastic equations of motion (setting $\dot{\mathbf{u}}_e = 0$, $\ddot{\mathbf{u}}_e = 0$ and isolating $\mathbf{u}_e = \mathbf{u}_{e0}$). This strategy known as residualized model approach is proposed in [37] and extended to unsteady aerodynamic forces with lag states from a rational function approximation in [38]. Additional details about the application of the method are provided in [34] and [41].

The derivation of the residualized unsteady aerodynamic forces is described. The first step consists of calculating the quasi-static deformation predicted by the aeroelastic equations of motion (equation 2.3) with $\dot{\mathbf{u}}_e = 0$, $\ddot{\mathbf{u}}_e = 0$ as shown in equation 2.27. The unsteady terms due to elastic deformation in the motion-induced aerodynamic forces are also removed. The rational function approximation is used to express the unsteady aerodynamic forces in the time domain. In this case, the effect of rigid body motion on the dynamic flexible deformation is not considered. However, its effect can be included as an additional unsteady aerodynamic force due to the flight dynamic states from equations 2.1 and 2.2 as shown in [38].

$$\mathbf{K}_{ee} \mathbf{u}_{e0} = \phi_{g_e}^T \mathbf{F}_g(t) = \bar{q} (\mathbf{F}_{ee0} \mathbf{u}_{e0} + \mathbf{F}_{er} \mathbf{u}_r + \mathbf{F}_{eG} \mathbf{w}_G) \quad (2.27)$$

The quasi-static flexible contribution can be isolated:

$$\mathbf{u}_{e0} = \bar{q}(\mathbf{K}_{ee} - \bar{q}\mathbf{F}_{ee0})^{-1} (\mathbf{F}_{er}\mathbf{u}_r + \mathbf{F}_{eG}\mathbf{w}_G) \quad (2.28)$$

The increment of unsteady aerodynamic forces and moments due to dynamic flexibility affecting the rigid degrees of freedom is shown in equation 2.29, where the additional states of the rational function approximation are solved through the N_{de} (number of additional lag states) equations given in 2.30. These equations are decoupled for each lag state. Unsteady aerodynamic effects due to rigid body motion are included in the quasi-steady flexible aerodynamic model. An interpolation approach between different rational function approximations can be also applied in this case for different Mach numbers as proposed with the gust-induced forces. The aircraft mass is a relevant parameter in this case as it plays an important role in the flexible response (\mathbf{u}_e).

$$\begin{bmatrix} \Delta \mathbf{F}_b^{flex} \\ \Delta \mathbf{M}_b^{flex} \end{bmatrix} = \bar{q} \left(\mathbf{F}_{re0}(\mathbf{u}_e - \mathbf{u}_{e0}) + \frac{\mathbf{F}_{re1}}{V_\infty} \dot{\mathbf{u}}_e + \frac{\mathbf{F}_{re2}}{V_\infty^2} \ddot{\mathbf{u}}_e + \sum_{i=1}^{N_{de}} \mathbf{F}_{re(i+2)} \mathbf{u}_{ei} \right) \quad (2.29)$$

$$\dot{\mathbf{u}}_{ei} = V_\infty d_{ei} \mathbf{u}_{ei} + \dot{\mathbf{u}}_e \quad (2.30)$$

2.4.2 Integrated State-space Model

As seen in section 1.3.3, the aeroelastic model can be expressed as a state space model. The dynamic increment due to flexible deformation can be also calculated through an aeroelastic state-space model. There is the possibility to integrate the state-space model with the nonlinear equations of motion (equations 2.1 and 2.2) or with its linearized form. This part describes the procedure to adapt the previous presented state-space model according to the residualized model approach to remove the quasi-static flexible contribution. This allows calculating the increment due to dynamic flexibility.

The aeroelastic state space model can be split in the rigid and flexible contribution:

$$\begin{bmatrix} \dot{\mathbf{x}}_r \\ \dot{\mathbf{x}}_e \\ \dot{\mathbf{x}}_L \end{bmatrix} = \begin{bmatrix} \mathbf{A}_{rr} & \mathbf{A}_{re} & \mathbf{A}_{rL} \\ \mathbf{A}_{er} & \mathbf{A}_{ee} & \mathbf{A}_{eL} \\ 0 & 0 & \mathbf{A}_{LL} \end{bmatrix} \begin{bmatrix} \mathbf{x}_r \\ \mathbf{x}_e \\ \mathbf{x}_L \end{bmatrix} + \begin{bmatrix} \mathbf{B}_r \\ \mathbf{B}_e \\ \mathbf{B}_g \end{bmatrix} \mathbf{U} \quad (2.31)$$

With \mathbf{x}_r being the rigid states (\mathbf{u}_r , $\dot{\mathbf{u}}_r$ and lag coefficients \mathbf{u}_r^i), \mathbf{x}_e being the flexible states (\mathbf{u}_e , $\dot{\mathbf{u}}_e$ and lag coefficients \mathbf{u}_e^i) and \mathbf{x}_L the delays due to the wind input or control surface deflections if considered.

The global flexible states are expressed as a quasi-static and dynamic contributions:
 $\mathbf{x}_e = \mathbf{x}_e^{QS} + \Delta \mathbf{x}_e$

The quasi-static contribution can be found by residualizing the state space model. In this case, the residualization is done through the flexible states ($\dot{\mathbf{x}}_e = 0$). According to equation 2.31, the quasi-static flexible contribution can be found :

$$\mathbf{x}_e^{QS} = -\mathbf{A}_{ee}^{-1}(\mathbf{A}_{er}\mathbf{x}_r + \mathbf{A}_{eL}\mathbf{x}_L + \mathbf{B}_e\mathbf{U}) \quad (2.32)$$

The dynamic flexible effect can then be calculated from the state space model by replacing $\mathbf{x}_e = \mathbf{x}_e^{QS} + \Delta\mathbf{x}_e$ in equation 2.31 and adding the quasi-static flexible definition of equation 2.32.

$$\Delta\dot{\mathbf{x}}_e = \mathbf{A}_{ee}\Delta\mathbf{x}_e + \mathbf{A}_{ee}^{-1}\mathbf{A}_{er}\dot{\mathbf{x}}_r + \mathbf{A}_{ee}^{-1}\mathbf{A}_{eL}\dot{\mathbf{x}}_L + \mathbf{A}_{ee}^{-1}\mathbf{B}_e\dot{\mathbf{U}} \quad (2.33)$$

When replacing the last expression concerning the lag states of equation 2.31 in equation 2.33, the new state space model to be solved is expressed as:

$$\begin{bmatrix} \Delta\dot{\mathbf{x}}_E \\ \dot{\mathbf{x}}_L \end{bmatrix} = \begin{bmatrix} \mathbf{A}_{ee} & \mathbf{A}_{ee}^{-1}\mathbf{A}_{eL}\mathbf{A}_{LL} \\ 0 & \mathbf{A}_{LL} \end{bmatrix} \begin{bmatrix} \Delta\mathbf{x}_e \\ \mathbf{x}_L \end{bmatrix} + \begin{bmatrix} \mathbf{A}_{ee}^{-1}\mathbf{A}_{er} & \mathbf{A}_{ee}^{-1}\mathbf{A}_{eL}\mathbf{B}_L & \mathbf{A}_{ee}^{-1}\mathbf{B}_e \\ 0 & \mathbf{B}_L & 0 \end{bmatrix} \begin{bmatrix} \dot{\mathbf{x}}_r \\ \mathbf{U} \\ \dot{\mathbf{U}} \end{bmatrix} \quad (2.34)$$

If the dynamic contribution ($\Delta\mathbf{x}_e$) can be calculated by solving the aeroelastic state space model of equation 2.34, the increment of aerodynamic force and moment due to the dynamic flexible effect can be integrated with the nonlinear equations of motion through the expression given in equation 2.35. Additional details on the aeroelastic state space model are provided in section 1.3.3.

$$\begin{bmatrix} \Delta F_b^{flex} \\ \Delta M_b^{flex} \end{bmatrix} = \left(M_{rr} - \bar{q} \frac{F_{rr2}}{V_\infty^2} \right) \mathbf{A}_{re} \Delta\dot{\mathbf{x}}_e \quad (2.35)$$

Part II

Results

Chapter 3

Theoretical Gust

This chapter presents the results of the previously detailed approach applied to simulate the aircraft response to different vertical and lateral theoretical gust. The aircraft configuration is the same for all the sections and it is associated with a generic current passenger aircraft.

3.1 Gust Definition

The gust excitation is assumed to be known and is the one specified for loads certification purposes [3]. Different gust profiles are used as input exciting different frequency ranges both in vertical and lateral. Figures 3.1 and 3.2 show the considered gust profiles in time and frequency domain. The parameter H defines half of the gust wavelength in feet. The gust amplitude is given by certification requirements. The analysis is based on the hypothesis that the gust profile is constant along the wingspan. This assumption is evaluated in chapter 4.

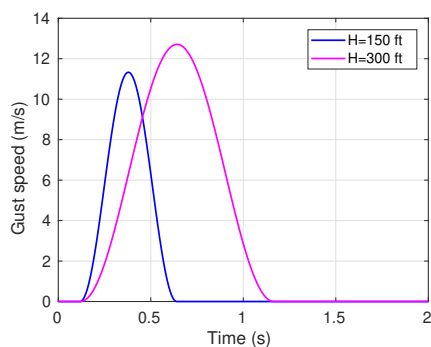


Figure 3.1: Gust profiles in time domain

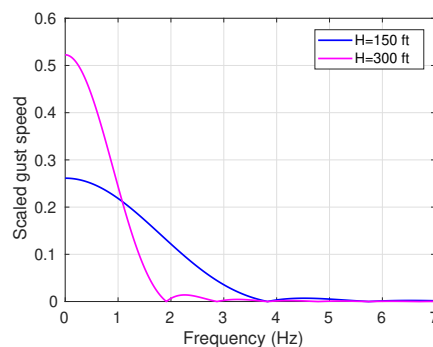


Figure 3.2: Gust profiles in frequency domain

3.2 Fixed Rigid Aircraft

In this section, the gust-induced effect is predicted by DLM and linearized CFD in the frequency domain. Results from CFD are used to built a model with different forms as detailed in sections 1.3.2 and 2.3 to capture the gust-induced effect in the time domain. Results are compared with nonlinear CFD in the time domain for a fixed rigid aircraft. Once the gust-induced effect is generated and validated, it is used in the next sections to predict the response of a free flying aircraft with different modelling assumptions.

Vertical Response

Gust-induced forces are computed with DLM and linearized CFD around a nonlinear steady state condition in the frequency range of interest of the gust excitation. The considered flight condition is $M=0.5$ and altitude of 0ft. In this case, corrected DLM and CFD-LFD predict similar aerodynamic responses at low frequencies as shown in figures 3.3 and 3.4 for the GAF in lift and pitch due to a vertical gust. DLM has been corrected with a quasi-steady aerodynamic database at low frequencies. Results from CFD-LFD have not been adjusted. Slight differences between both approaches can be explained by its different modelling assumptions. Geometrical parameters such as thickness are directly taken into account with CFD-LFD without corrections required. At low frequencies, the gust effect can be seen as a constant angle of attack seen by the whole aircraft at the same time and the value of the GAF in lift at low frequencies can be associated with the lift force quasi-steady coefficient (Cz_α). The same can be done in pitch at low frequencies (Cm_α).

A rational function approximation according to section section 1.3.2 is applied to express the unsteady aerodynamic forces from CFD-LFD in the time domain. The Roger approximation is applied with 10 delay coefficients. The GAF is plotted in the frequency domain to validate the rationalisation as shown in figures 3.3 and 3.4.

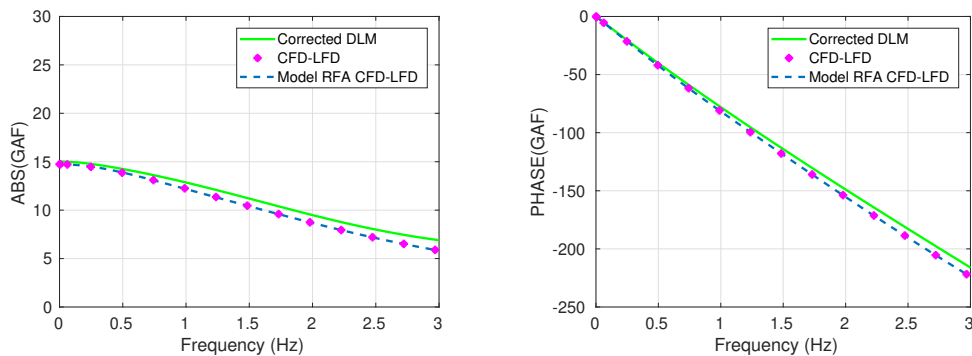


Figure 3.3: GAF in lift due to vertical gust

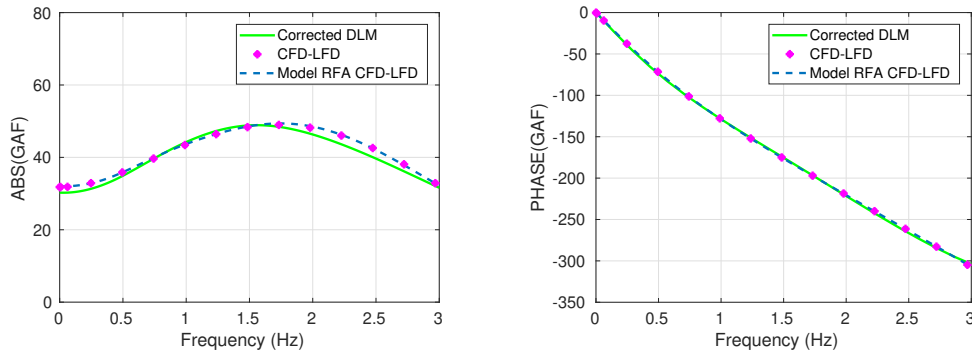


Figure 3.4: GAF in pitch due to vertical gust

At low frequencies, the CFD-LFD solution due to the gust excitation can be validated against unsteady motion-induced forces. As shown in figure 3.5, a rigid body rotation, a heaving velocity and a vertical gust excitation create the same angle of attack variation all along the aircraft at low frequencies. The aerodynamic response is therefore expected to be the same at low frequencies as shown in figure 3.6. The difference in phase of 90° of the GAF in lift due to heaving motion is due to the fact that the derivative of the vertical translation (heaving speed) is taken into account.



Figure 3.5: Heave, pitch and vertical gust modes at a frequency close to zero (source:[17])

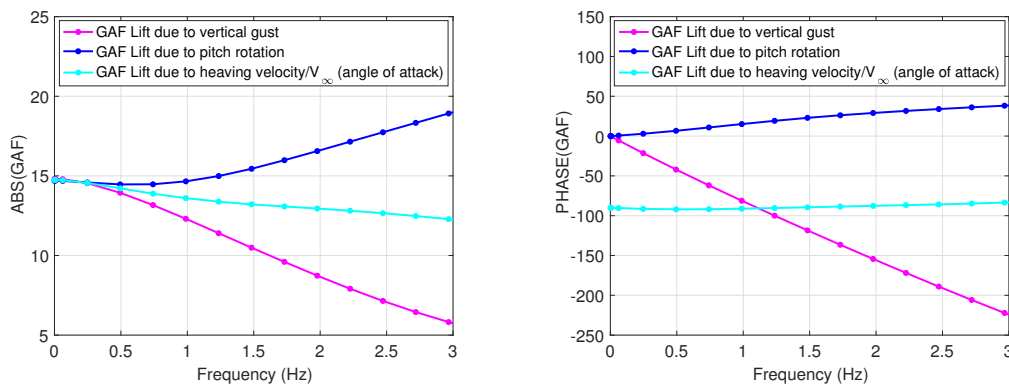


Figure 3.6: Comparison of GAF in lift due to heave motion, pitch rotation and vertical gust

The predicted increment of lift and pitching moment due to a vertical gust with CFD-LFD in the time domain show a very good agreement with nonlinear CFD at the considered flight conditions ($M=0.5$ and $h=0\text{ft}$) as shown in figures 3.7 and 3.8.

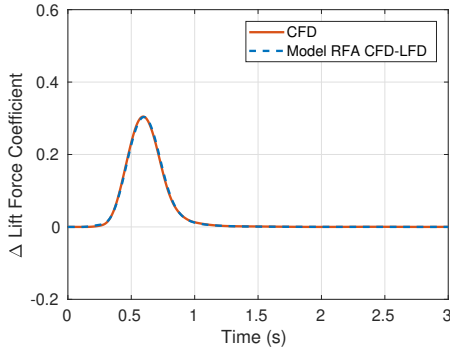


Figure 3.7: Lift coefficient of fixed rigid A/C due to vertical gust ($H=150\text{ft}$)

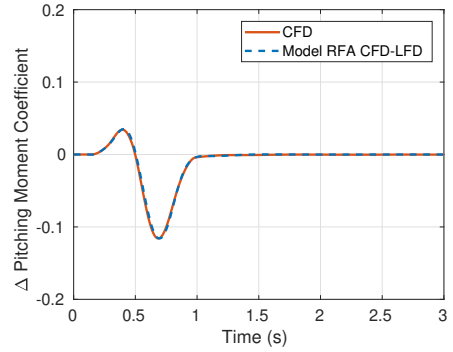


Figure 3.8: Pitching moment coefficient of fixed rigid A/C due to vertical gust ($H=150\text{ft}$)

There is another possibility to validate the results from CFD-LFD. The GAF can also be calculated from nonlinear unsteady CFD simulations in the time domain. Instead of solving the linearized problem, harmonic gust inputs at specific frequencies are applied and solved in the time domain. Different solutions in the time domain are obtained for each gust frequency, which provide a GAF value at these frequencies. This approach can also be useful to assess possible aerodynamic nonlinearities. The GAF calculation in lift and pitch at low frequencies is compared with the one calculated from nonlinear harmonic CFD simulations in the time domain in figures 3.9 and 3.10 showing a good agreement.

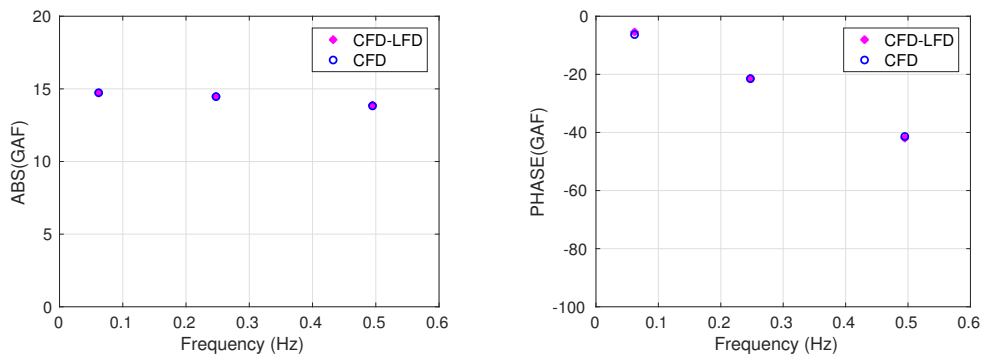


Figure 3.9: GAF in lift due to vertical gust

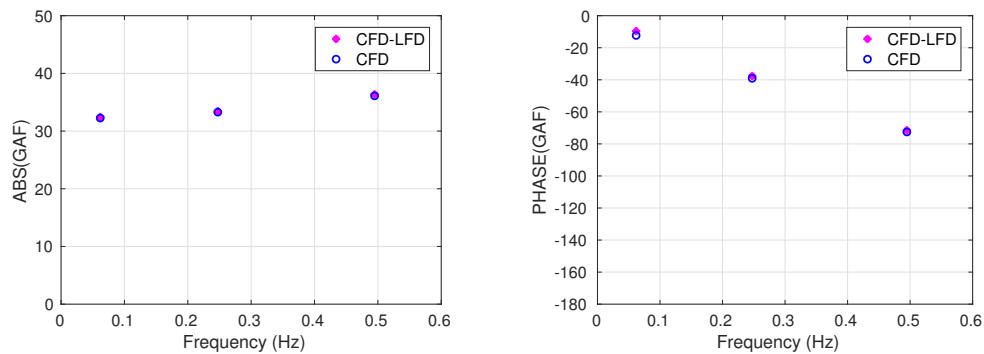


Figure 3.10: GAF in pitch due to vertical gust

Lateral Response

The same gust profile as the one detailed in figures 3.1 and 3.2 is applied to simulate lateral gust encounters. Instead of an angle of attack variation, the lateral gust modifies the sideslip seen by the aircraft. DLM requires specific corrections to simulate lateral gusts due to the geometry simplification of panels. A more accurate aircraft shape can be used with CFD-LFD to simulate the lateral response. The steady state including the static deformation is accounted in the linearized unsteady simulation and geometric parameters such as the dihedral angle effect which plays an important role in lateral can be directly considered.

Once the DLM is corrected to account for geometric effects, both approaches predict similar aerodynamic responses as shown in figure 3.11 and 3.12 for the GAF projected in roll and yaw due to a lateral gust ($M=0.5$ and $h=0\text{ft}$). A rational function approximation with 10 delay coefficients is also applied to express the GAF from CFD-LFD in the time domain and validated in the frequency domain for the range considered in this case.

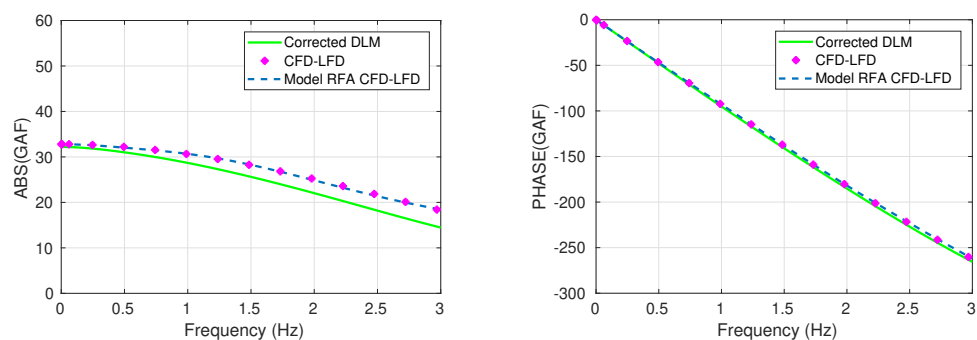


Figure 3.11: GAF in roll due to lateral gust

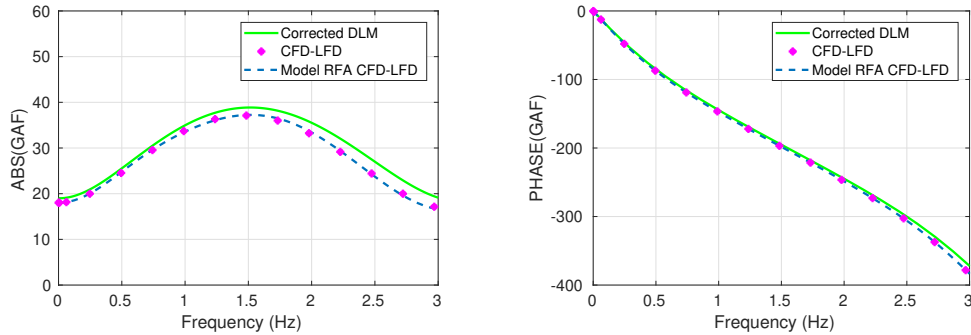
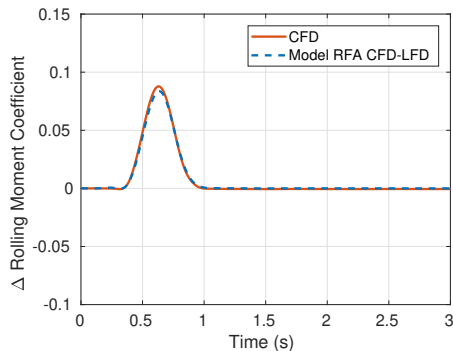
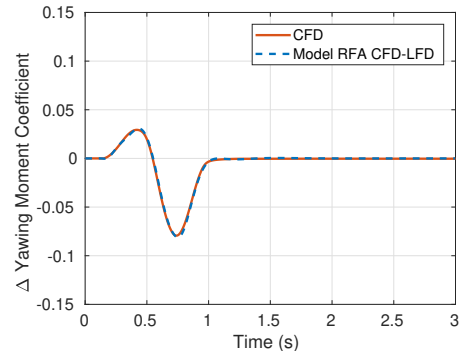


Figure 3.12: GAF in yaw due to lateral gust

The approximated forces are also compared with nonlinear CFD in the time domain. Lateral gust-induced forces expressed through the rational function approximation are able to capture the delay between the nose and the VTP for the frequency range of interest. In this case, the approximation is based on the gust sensor positioned at the fuselage front part and is meant to cover the low frequency range.

Figure 3.13: Rolling moment coefficient of fixed rigid A/C due to lateral gust ($H=150\text{ft}$)Figure 3.14: Yawing moment coefficient of fixed rigid A/C due to lateral gust ($H=150\text{ft}$)

Reduction Aerodynamic States

At low frequencies, the number of required states of the rational function approximation can be reduced. Different options are possible to capture the gust-induced effects with a reduced number of aerodynamic states.

Dynamic gust-induced coefficients can be extracted to capture the main effects at low frequencies as detailed in section 2.3 and proposed in [10]. These coefficients ($Cz_{\dot{\alpha}_G}$, $Cm_{\dot{\alpha}_G}$,

$Cl_{\dot{\beta}_G}$ and $Cn_{\dot{\beta}_G}$) are identified in this section from linearized CFD simulations through a rational function approximation with one lag state. An example of increment of lift due to the gust effect is given in equation 2.15.

A different lag state can be associated with each degree of freedom. In lift, the time lag is associated with the delay between the nose and the wing, as the wing is the main contribution in lift. Figure 3.15 shows the identification of the model from CFD-LFD simulations as expressed in equation 2.15 according to the RFA with one lag state. In pitch, the delay is associated with a distance between the nose and a point between the wing and HTP, as both surfaces contribute to the response in pitch. The delay coefficient set for the RFA (τ_G) is higher than for lift. The model in pitch identified through the form of equation 2.15 is plotted in the frequency domain in figure 3.16 against the simulation results from CFD-LFD used to generate the model.

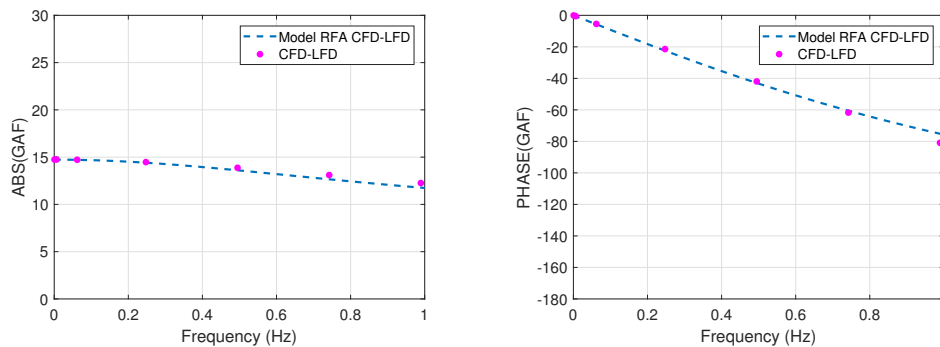


Figure 3.15: GAF in lift due to vertical gust

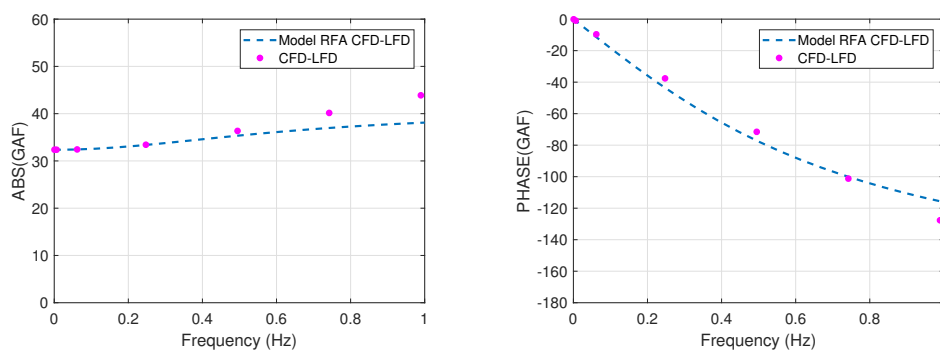


Figure 3.16: GAF in pitch due to vertical gust

The predicted gust-induced effect can be validated as well by comparing the predicted response with nonlinear CFD in the time domain for a fixed rigid aircraft as shown in

figures 3.17 and 3.18 for lift and pitch. The model is used to predict the response due to a low frequency gust profile ($H=300\text{ft}$ from figures 3.1 and 3.2).

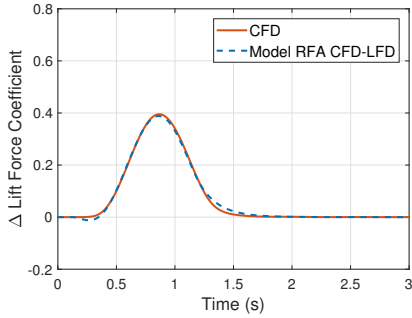


Figure 3.17: Lift coefficient of fixed rigid A/C due to vertical gust ($H=300\text{ft}$)

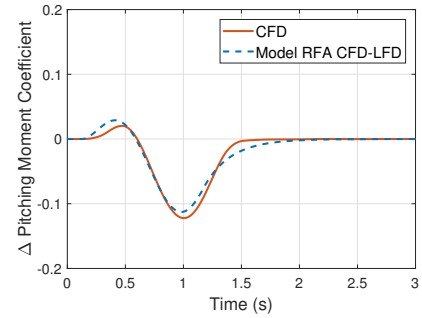


Figure 3.18: Pitching moment coefficient of fixed rigid A/C due to vertical gust ($H=300\text{ft}$)

In roll, the time lag is associated as in lift with the delay between the nose and the wing, as the wing is also the main contribution in roll. The same delay coefficient as in lift is set to identify the model in roll. Figure 3.19 shows the model generated from CFD-LFD simulations in the frequency domain to validate the identification. In yaw, the main contribution is the VTP and the lag state captures the time it takes the gust disturbance from the nose to the VTP. In this case, the delay coefficient of the RFA (τ_G) is higher than for the other axes, as the time lag is associated with a longer distance. The model in yaw identified with the form of equation 2.15 is also plotted in the frequency domain against CFD-LFD simulations in figure 3.20.

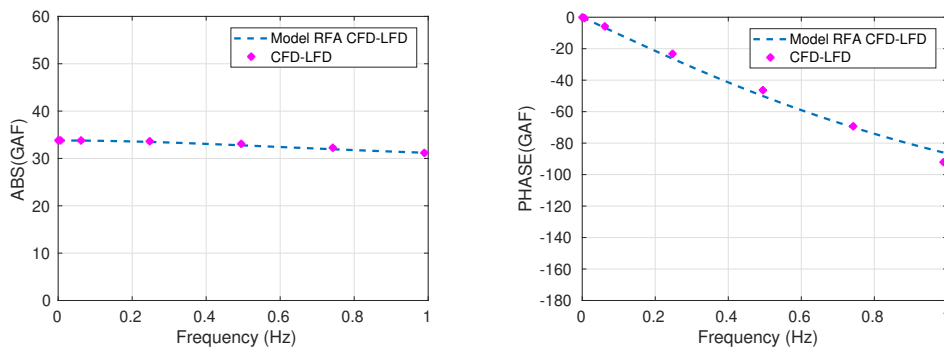


Figure 3.19: GAF in roll due to lateral gust

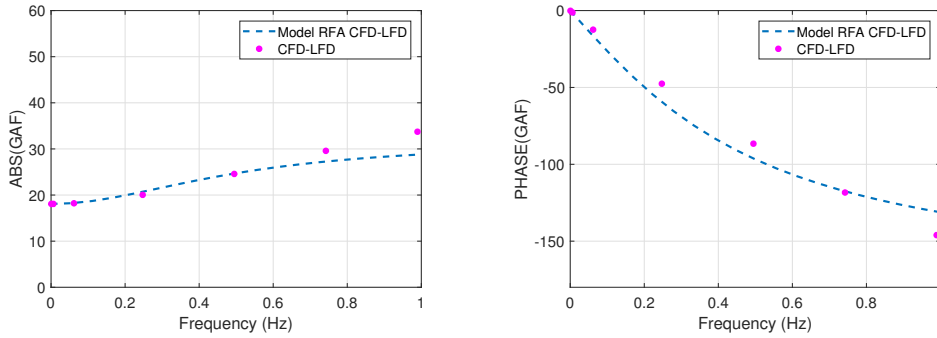


Figure 3.20: GAF in yaw due to lateral gust

The predicted gust-induced effect in roll and yaw from the identified model is also validated against nonlinear CFD in the time domain for a fixed rigid aircraft as shown in figures 3.21 and 3.22.

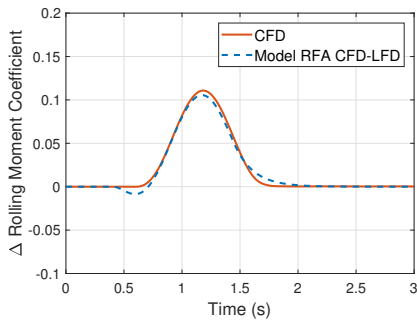


Figure 3.21: Rolling moment coefficient of fixed rigid A/C due to lateral gust (H=300ft)

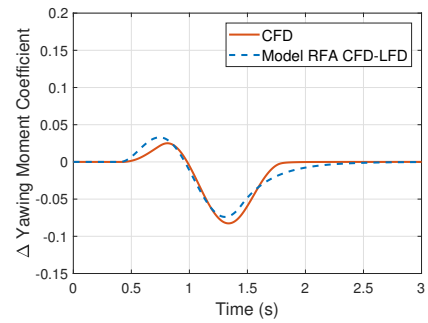


Figure 3.22: Yawing moment coefficient of fixed rigid A/C due to lateral gust (H=300ft)

Slight differences in amplitude are observed due to the approximation of the gust-induced time lag with a single aerodynamic state. However, this model is able to capture the right phase of the response to both vertical and lateral gusts exciting relevant frequencies for flight dynamics investigations. If higher accuracy is required or effects at higher frequencies need to be captured, additional delay coefficients can be added as shown previously in this section.

Another possibility to increase the accuracy of the prediction by keeping a low number of additional aerodynamic states consists of adding an explicit delay as shown in section 2.3. As detailed in equation 2.16, an explicit delay is added to the form of the rational function approximation with one aerodynamic lag state and used to identify the gust-induced aerodynamic derivatives. In this case, an explicit delay is added between the

aircraft nose sensor position and the wing leading edge, which is defined by the distance between both parts ($l_{A/B}$) and the aircraft speed (V_∞) in equation 2.16. The same delay is applied for all the axes but an optimization would be possible to set the most appropriate point for each degree of freedom as detailed in section 2.3.

The model with an explicit delay from the aircraft nose to the wing identified through a RFA with one lag state is shown in figures 3.23 and 3.24 for lift and pitch in the frequency domain. A good agreement with linearized CFD simulations can be observed in the frequency range of interest to validate the identification. The frequency is also limited to 1 Hz to cover a typical range for flight dynamics investigations. The only difference with respect to the previous calculated GAF in figures 3.15 and 3.16 can be seen in the phase. The explicit delay creates a phase shift which can be better captured with a RFA with one additional lag state.

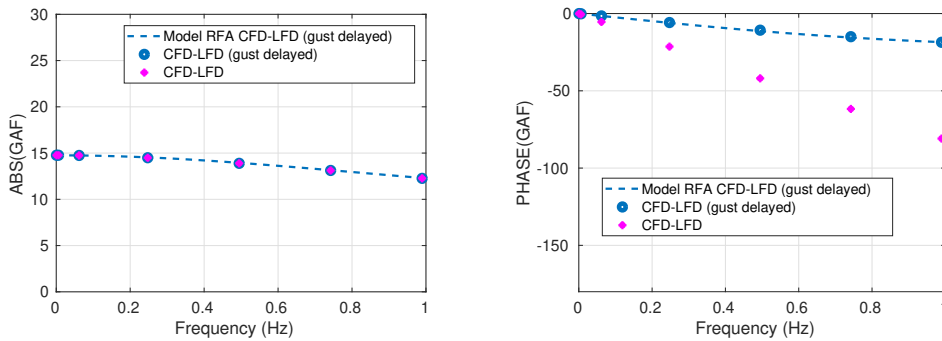


Figure 3.23: GAF in lift due to vertical gust

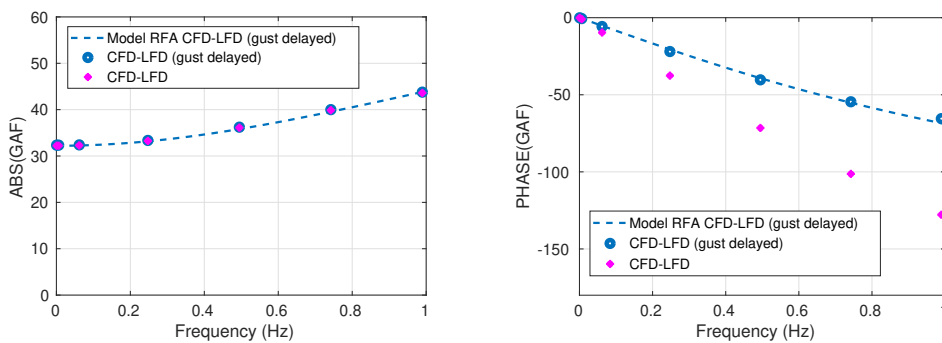


Figure 3.24: GAF in pitch due to vertical gust

Figures 3.25 and 3.26 show the predicted response in the time domain of the previous identified model with an explicit delay for the low frequency gust profile ($H=300\text{ft}$ from

figures 3.1 and 3.2). A good agreement in the time domain can be also observed with respect to nonlinear CFD.

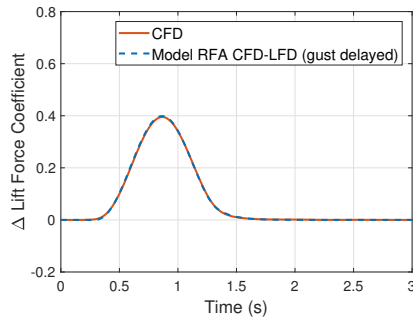


Figure 3.25: Lift coefficient of fixed rigid A/C due to vertical gust (H=300ft)

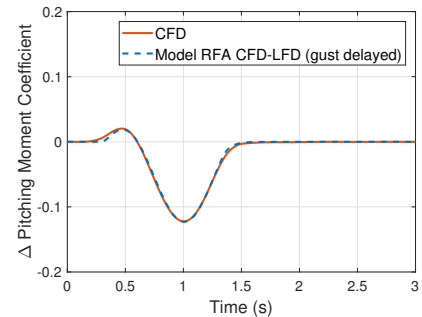


Figure 3.26: Pitching moment coefficient of fixed rigid A/C due to vertical gust (H=300ft)

The same approach is applied in lateral by adding the explicit delay from the nose sensor to the wing leading edge to the model previously identified with an additional aerodynamic state. The model identified from linearized CFD simulations is shown in figures 3.27 and 3.28 for roll and yaw. The low delay required in roll is justified by the fact that the wing is the main contribution in roll and the explicit delay already captures the whole propagation lag from the nose to the wing. The delay in yaw is associated with the distance from the wing to the VTP which can be better captured with an additional aerodynamic state. The model in the frequency domain also shows a good agreement with the simulations from linearized CFD. The predicted response in roll and yaw due to a lateral gust from the identified model is also validated against nonlinear CFD in the time domain as shown in figures 3.29 and 3.30.

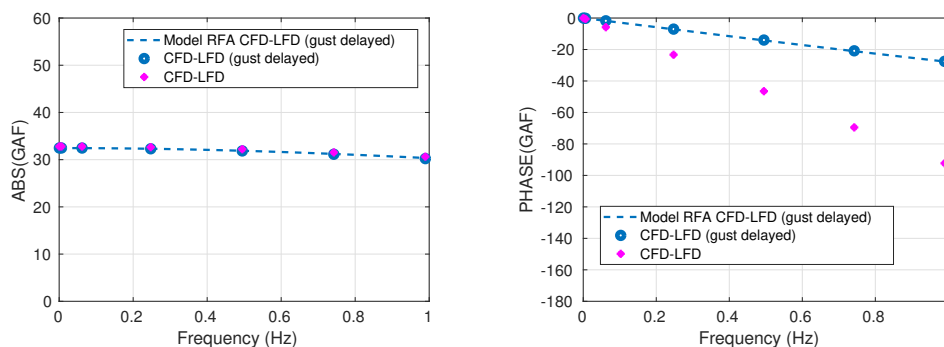


Figure 3.27: GAF in roll due to lateral gust

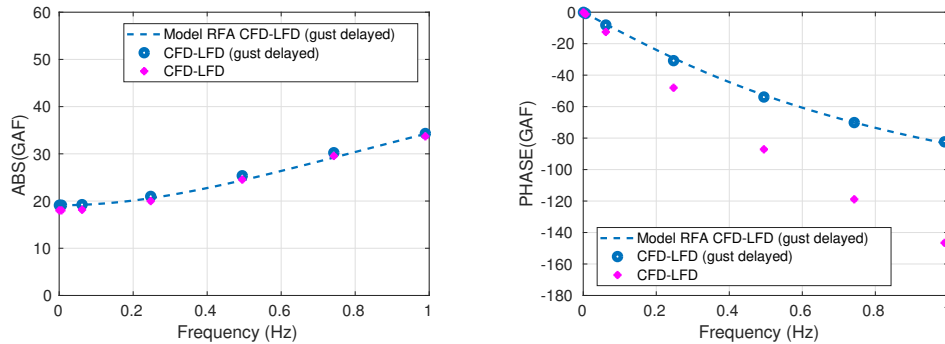
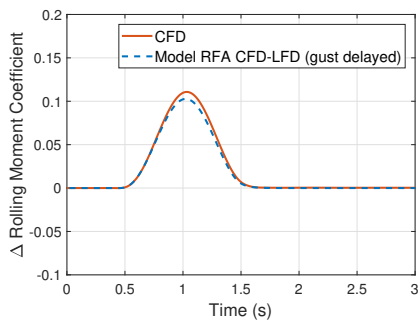
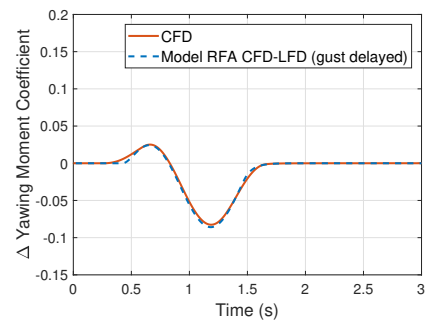


Figure 3.28: GAF in yaw due to lateral gust

Figure 3.29: Rolling moment coefficient of fixed rigid A/C due to lateral gust ($H=300\text{ft}$)Figure 3.30: Yawing moment coefficient of fixed rigid A/C due to lateral gust ($H=300\text{ft}$)

3.3 Free Flying Quasi-steady Flexible Aircraft

Once the gust-induced effect is validated through the different forms presented previously, the model is integrated with the flight dynamics equations of motion to analyse the aircraft response to different gust profiles and conditions both in vertical and lateral. Quasi-steady flexible aerodynamics are used to compute aerodynamic forces due to aircraft motion. Dynamic flexible effects are not considered in this section.

Vertical Response

Figure 3.31 and 3.32 show the aircraft response in lift and pitch due to a vertical low frequency gust profile ($H=300\text{ft}$ presented in figures 3.1 and 3.2). The same model with the gust contribution limited to an angle of attack effect at low frequencies is also shown to illustrate the importance of the gust-induced effect. The predominant physics captured is

the gust propagation effect along the aircraft. Figure 3.31 shows the gust propagation effect through the delay between the aircraft nose and the wing, which is the main contribution in lift. The gust propagation effect plays an important role in pitch as the disturbance has an impact on the different parts of the aircraft at different times. The aircraft response in pitch shown in 3.32 through the increment of pitching moment coefficient shows the initial pitch up due to gust effect in the forward part of the fuselage and then the stabilizing pitch down once the gust affects the wing and reaches the HTP, reducing the increase of angle of attack due to the gust. This response depends on the position centre of gravity.

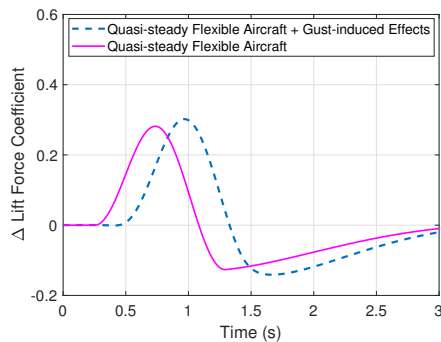


Figure 3.31: Lift coefficient of quasi-steady flexible A/C due to vertical gust (H=300ft)

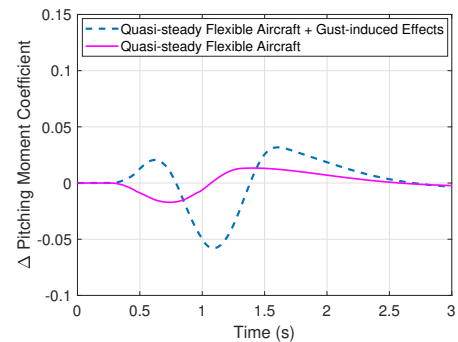


Figure 3.32: Pitching moment coefficient of quasi-steady flexible A/C due to vertical gust (H=300ft)

The previous model based approach is compared with high fidelity simulations (CFD-CSM-FM). Figures 3.33 and 3.34 show a good agreement in the predicted response between both approaches for the frequency range excited in this case (figure 3.2 for the gust with H=300ft). The high fidelity approach includes 90 flexible modes. At this frequency range and for the aircraft configuration studied, quasi-static flexible effects are sufficient.

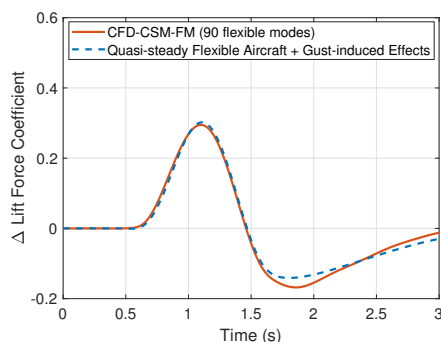


Figure 3.33: Lift coefficient of quasi-steady flexible A/C due to vertical gust (H=300ft)

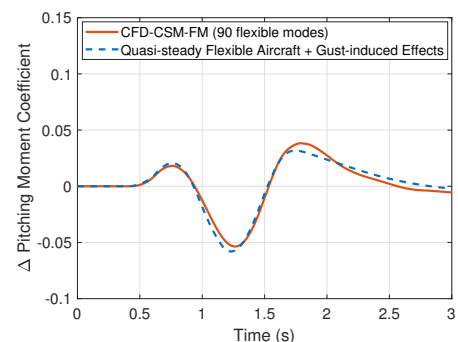


Figure 3.34: Pitching moment coefficient of quasi-steady flexible A/C due to vertical gust (H=300ft)

Lateral Response

Figures 3.35 and 3.36 show the predicted response in roll and yaw due to a lateral gust creating a sideslip variation, instead of an increment of angle of attack. The impact of gust propagation in lateral can be seen. The propagation effect in roll is similar as in lift. The main contribution in roll is also the wing and the delay between the nose and the wing creates a similar effect in roll as the one shown in figure 3.31. As the VTP provides the main effect in yaw, the delay between the nose and VTP need to be captured for accurate responses. The front fuselage part also contributes to yaw with the initial peak that can be be seen in figure 3.36. This effect also depends on the position of the centre of gravity. The model-based approach is also compared with high fidelity simulations. The response in figures 3.37 and 3.38 show a good agreement between both approaches. At this frequency range and for this aircraft, the assumption of quasi-static flexibility is also sufficient.

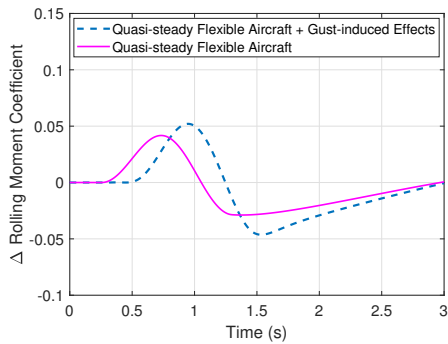


Figure 3.35: Rolling moment coefficient of quasi-steady flexible A/C due to lateral gust (H=300ft)

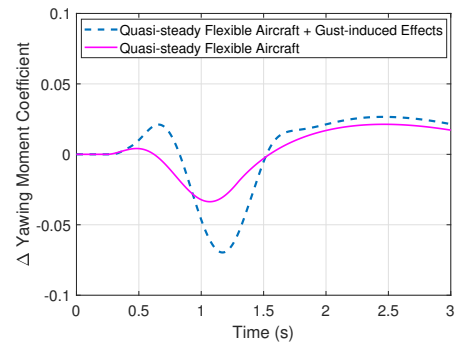


Figure 3.36: Yawing moment coefficient of quasi-steady flexible A/C due to lateral gust (H=300ft)

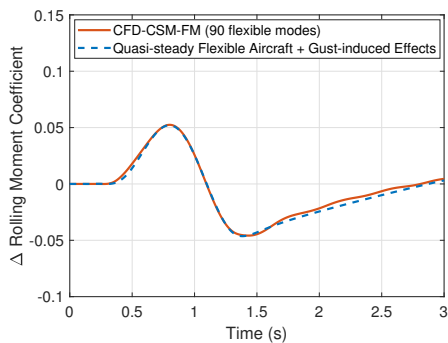


Figure 3.37: Rolling moment coefficient of quasi-steady flexible A/C due to lateral gust (H=300ft)

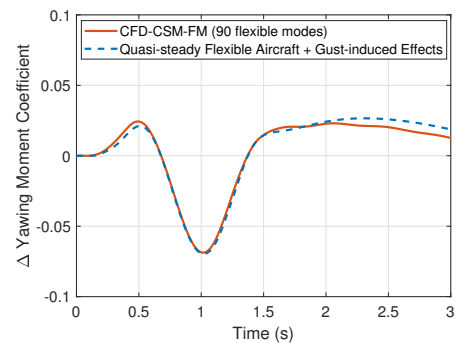


Figure 3.38: Yawing moment coefficient of quasi-steady flexible A/C due to lateral gust (H=300ft)

Effect of CG Position

Once the gust-induced effect is included in the flight dynamics equations of motion, the aircraft response can be simulated at different centre of gravity conditions in order to evaluate the stability in gust encounters. Figures 3.39 and 3.40 show the aircraft response in lift and pitch due to the low frequency gust profile ($H=300\text{ft}$) for different centre of gravity positions. The responses are calculated in open loop (flight control laws are not taken into account). The initial effect of the gust disturbance on the aircraft response is the initial pitch up due to the increased angle of attack at the forward part of the fuselage. Then, once the maximum gust amplitude reaches the wing and the HTP later on, the aircraft tends to pitch down stabilizing the aircraft by reducing the increase of angle of attack due to the gust as shown previously in figures 3.32 and 3.34. Figure 3.40 shows that the aircraft reacts less to the initial disturbance in the case with the forward centre of gravity position. The lever arm between the local lift forces created in the forward part of the aircraft is reduced compared to the case with the rearward centre of gravity. The stabilizing pitch down occurs earlier with the forward centre of gravity as the lever arm between the aerodynamic centre and the centre of gravity is higher than in the case with rearward centre of gravity. Figure 3.41 is included to illustrate this effect. The aircraft is more stable with the forward centre of gravity position. The response in lift shows a slightly reduced maximum lift with the centre of gravity in the forward position due to the reduced maximum angle of attack variation induced by the response in pitch.

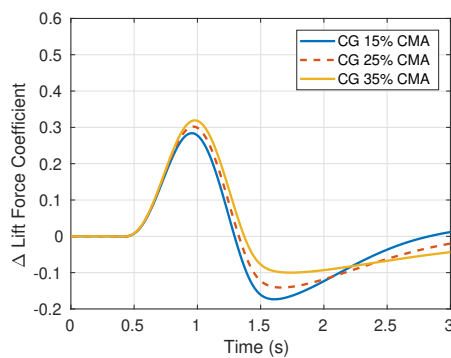


Figure 3.39: Lift coefficient of quasi-steady flexible A/C due to vertical gust ($H=300\text{ft}$) for different CG

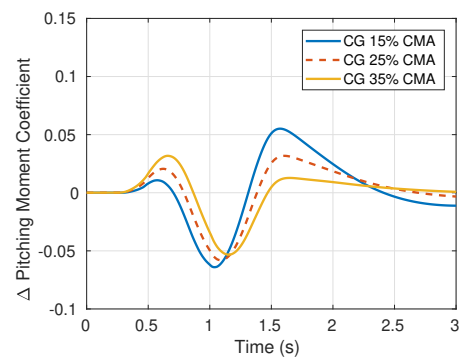


Figure 3.40: Pitching moment coefficient of quasi-steady flexible A/C due to vertical gust ($H=300\text{ft}$) for different CG

The open loop response of the aircraft, once the gust is gone, shows the short period mode. As demonstrated in [5], the damping of this mode is directly linked with the coefficient Cm_α and is reduced once the centre of gravity is moved in the forward position. This can be seen both in the increment of lift force and pitching moment coefficient in

figures 3.39 and 3.40. The response in pitch can be controlled through the elevator. Another mode excited which is not visible in the figure is the phugoid (exchange of energy between speed and altitude at a constant angle of attack). Its period is high enough to be controlled with the pilot or flight control laws.

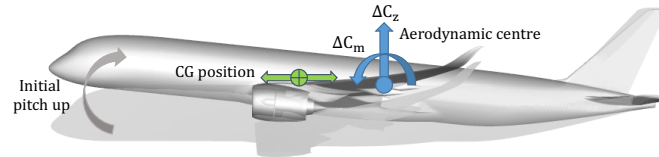


Figure 3.41: Illustration of the effect at different centre of gravity positions in vertical

The centre of gravity effect is also analysed for lateral gusts. Figures 3.42 and 3.43 show the response due to the same lateral gust used in the previous section for different centre of gravity positions. As in pitch, the effect of the lateral gust at the forward part of the fuselage creates a local increment of sideslip increasing the yawing moment coefficient. The lever arm of the local lateral forces at the front fuselage to the centre of gravity is lower in the case with the forward centre of gravity position. Once the gust reaches the VTP, the side force created stabilises the aircraft reducing the initial increase of sideslip. The lever arm of the VTP is higher in the case of forward centre of gravity, increasing the stability with respect to the sideslip disturbance, restoring the direction of flight.

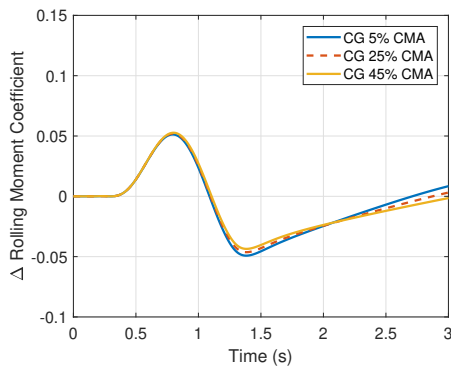


Figure 3.42: Rolling moment coefficient of quasi-steady flexible A/C due to vertical gust ($H=300\text{ft}$) for different CG

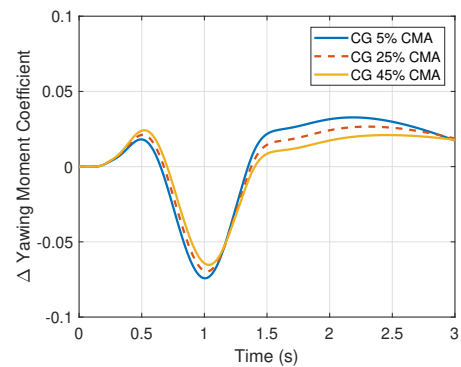


Figure 3.43: Yawing moment coefficient of quasi-steady flexible A/C due to vertical gust ($H=300\text{ft}$) for different CG

Figure 3.44 illustrates the effect of different centre of gravity position in yaw. The response in roll due to lateral gusts is not affected by centre of gravity variation along the longitudinal axis. The position of the centre of gravity along the vertical axis has a direct

effect in the amplitude of the response in roll due to the contribution of the increment of side force due to the lateral gust. After the gust effect, the open loop response shows the beginning of the dutch roll mode, which affects both roll and yaw due to its strong coupling.

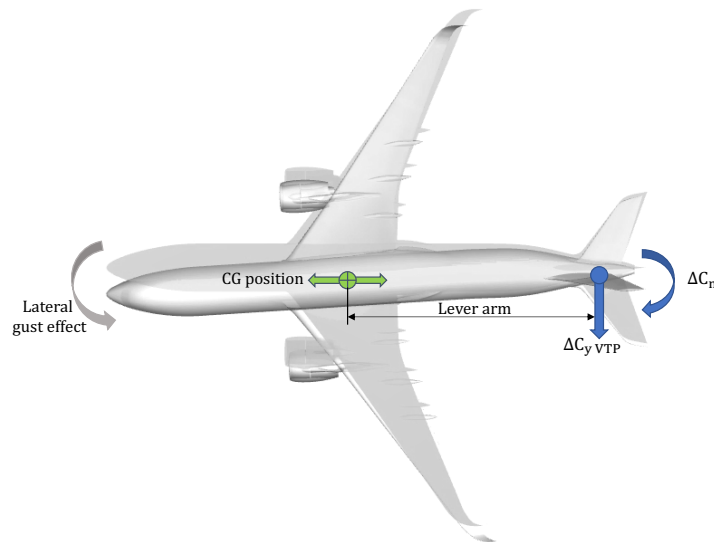


Figure 3.44: Illustration of the effect at different centre of gravity positions in lateral

Roll Damping

The roll stability in gust encounters can be analysed through the roll damping instead of the centre of gravity position. Once the aircraft encounters lateral disturbances, one side of the wing increases locally the angle of attack modifying the rolling moment due to asymmetrical lift distribution. When the aircraft reacts to this effect, the up-going wing reduces the initial increase of incidence while the one going downwards increases the local angle of attack. The induced rolling moment due to the aircraft manoeuvre brings back the wing to the initial state. Figure 3.45 illustrates this effect. The aerodynamic coefficient which captures the roll damping is the Cl_p . The wing dihedral plays an important role in the roll damping. The increment of incidence is higher if the wing has a dihedral, which increases the roll damping.



Figure 3.45: Illustration of the roll damping

Figure 3.46 and 3.47 shows the different response in roll and yaw due to a lateral gust with and without static deformation. The dihedral angle is decreased without static deformation as shown in figure 3.48 and the effect can be seen in the response. The initial increase in roll is less attenuated by the wing moving downwards as the increase of local angle of attack is less important compared to the aircraft response with higher wing dihedral. The impact in yaw is low and the differences observed can be explained by the coupling that appears between roll and yaw after the gust disturbance.

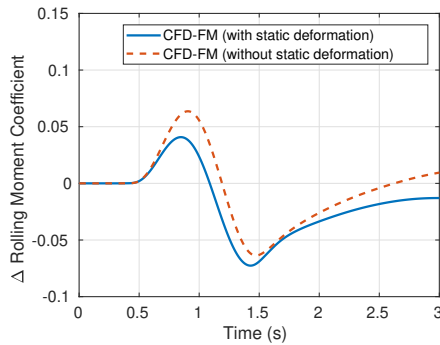


Figure 3.46: Rolling moment coefficient of free flying rigid A/C due to vertical gust ($H=300\text{ft}$) for different wing dihedral

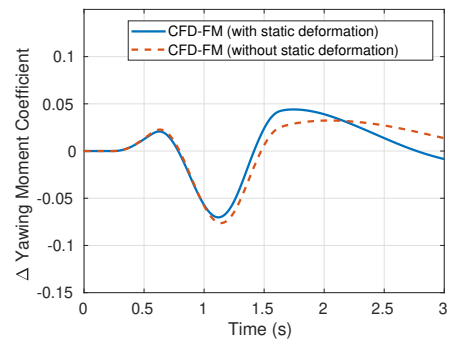


Figure 3.47: Yawing moment coefficient of free flying rigid A/C due to vertical gust ($H=300\text{ft}$) for different wing dihedral



Figure 3.48: Illustration of the dihedral effect with and without static deformation

Effect of Quasi-static Flexibility

Different options are possible in order to account for the quasi-static flexibility effect in the aerodynamic response. In the present study, the strategy proposed in [61] has been applied to correct the quasi-steady rigid aerodynamic data. The effect of the quasi-static flexibility in the aircraft response due to low frequency gusts is shown in figures 3.49, 3.50, 3.51 and 3.52 for vertical and lateral. A general reduction of the quasi-steady aerodynamic gradients can be seen due to the effect of quasi-static deformation of the airframe. The response in the increment of lift force and rolling moment coefficients show the effect of

the wing deformation. The local angle of attack variation seen by the HTP also plays a role in pitch as well as the different sideslip at the VTP in yaw. The beneficial dihedral effect in roll is also shown in figure 3.51.

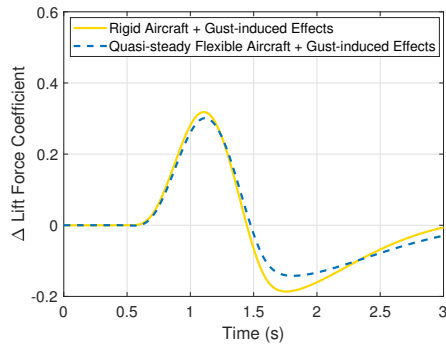


Figure 3.49: Lift coefficient of free flying rigid and quasi-steady flexible A/C due to vertical gust ($H=300\text{ft}$)

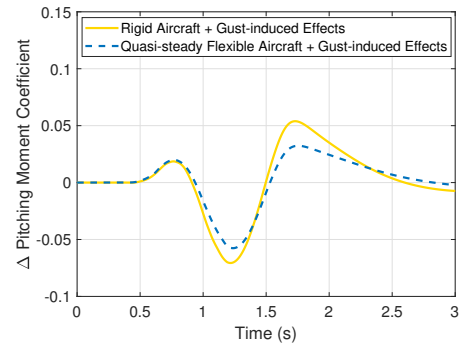


Figure 3.50: Pitching moment coefficient of free flying rigid and quasi-steady A/C due to vertical gust ($H=300\text{ft}$)

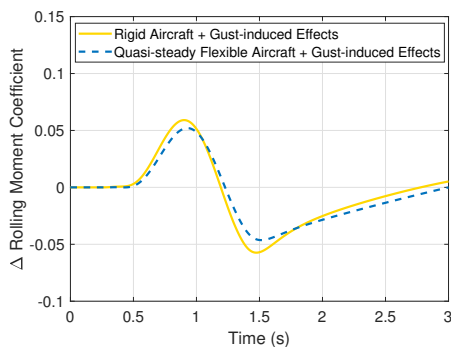


Figure 3.51: Rolling moment coefficient of free flying rigid and quasi-steady flexible A/C due to lateral gust ($H=300\text{ft}$)

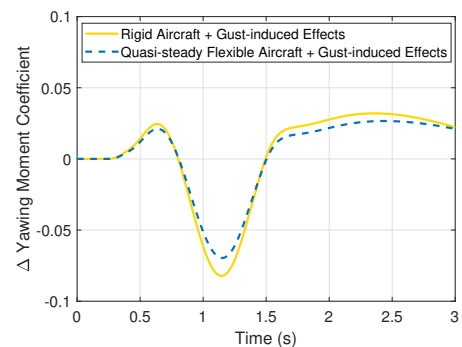


Figure 3.52: Yawing moment coefficient of free flying rigid and quasi-steady A/C due to lateral gust ($H=300\text{ft}$)

3.4 Free Flying Flexible Aircraft

In some cases, the correction of quasi-static flexibility is not enough to capture the response of the aircraft due to gust. Dynamic flexible effects can be added as detailed in the previous section. The previous assessed gust induced forces as well as residualized motion-induced forces of the elastic degrees of freedom are integrated in a flight mechanics model.

Different number of flexible modes can be retained. Quasi-steady flexible effects are already accounted for in the quasi-steady aerodynamics model. This allows considering less flexible modes reducing the overall number of states of the system. In this case, only the most energetic modes which are the ones at low frequencies are retained to capture the impact of dynamic flexibility on flight dynamics.

Vertical Response

Figures 3.53 and 3.54 show the aircraft response in lift and pitch for the vertical low frequency gust profile considered ($H=300\text{ft}$ in figures 3.1 and 3.2) with and without dynamic flexible effects. The good agreement between both responses shows that the hypothesis of quasi-static flexibility is sufficient to capture the same response as the approach which takes into account dynamic flexible effects. The impact of dynamic flexibility for this aircraft and this frequency range is low and it could be neglected.

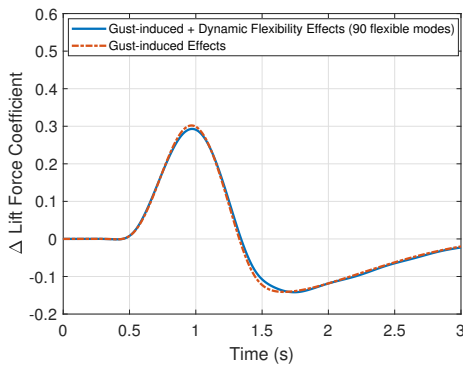


Figure 3.53: Lift coefficient of free flexible A/C due to vertical gust ($H=300\text{ft}$)

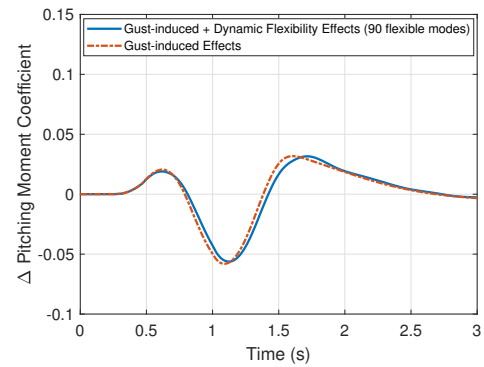


Figure 3.54: Pitching moment coefficient of free flexible A/C due to vertical gust ($H=300\text{ft}$)

For the gust profile which covers a higher frequency range ($H=150\text{ft}$ in figures 3.1 and 3.2), additional modes are excited and higher differences are observed if the dynamic contribution of the low frequency modes is neglected. This shows the impact of dynamic flexibility on aircraft flight dynamics. Part of the gust energy is absorbed by the structure, which excitation is visible through low amplitude oscillations. An example of the low frequency modes excited is included in figure 3.57. Wing bending mode impacts the lift force coefficient by absorbing part of the gust energy through its deformation. The fuselage bending mode modifies the angle of attack at the HTP which has an effect in pitch. In this case, the contribution of the gust to the flexible motion is considered, neglecting the impact of the rigid motion on the dynamic flexible response. Its effect could be also included as detailed in [38].

Different number of low frequency modes have been tested and as shown in figures 3.55 and 3.56, keeping 3 symmetric flexible modes (the ones shown in figure 3.57) allows capturing a response very close to the one obtained by the same model with 90 flexible modes. This offers the possibility to reduce the model computation cost which is interesting for flight dynamics needs of real-time simulation.

The predicted response of the model with dynamic flexible effects has been compared with high fidelity simulations taking into account 90 flexible modes in both cases in order to validate the approach. The predicted responses show a very good agreement between the model-based and the high fidelity simulation approach at the considered flight condition ($M=0.5$, $h=0ft$) as shown in figures 3.58 and 3.59. Further investigations at different flight conditions are shown at the end of this section.

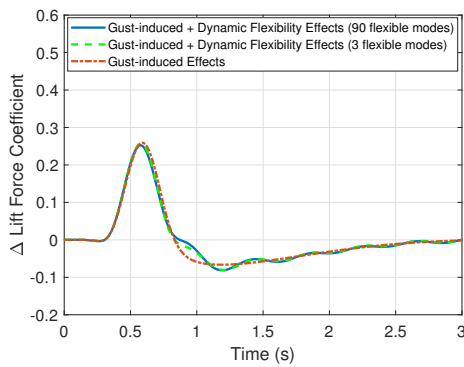


Figure 3.55: Lift coefficient of free flexible A/C due to vertical gust ($H=150ft$)

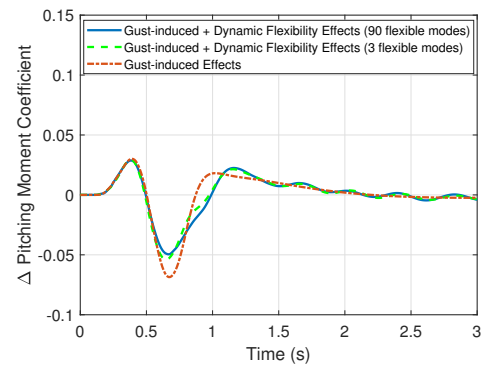


Figure 3.56: Pitching moment coefficient of free flexible A/C due to vertical gust ($H=150ft$)

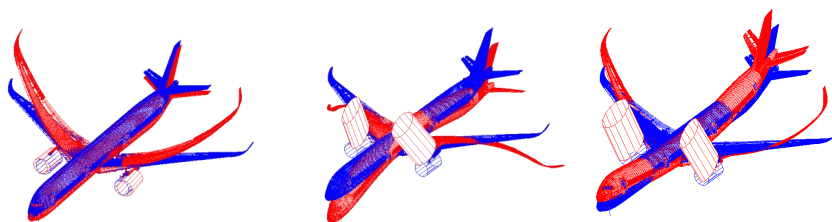


Figure 3.57: Low frequency modes which impact lift force and pitching moment coefficients (Wing and fuselage bending and symmetric engine modes with amplification factor)

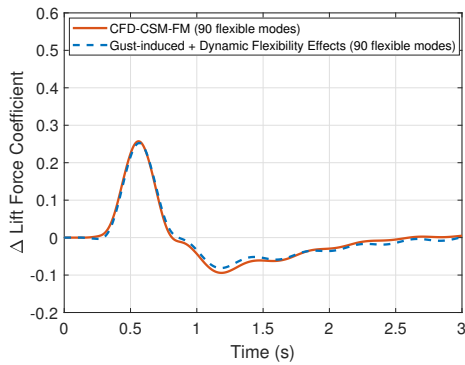


Figure 3.58: Lift coefficient of free flexible A/C due to vertical gust (H=150ft)

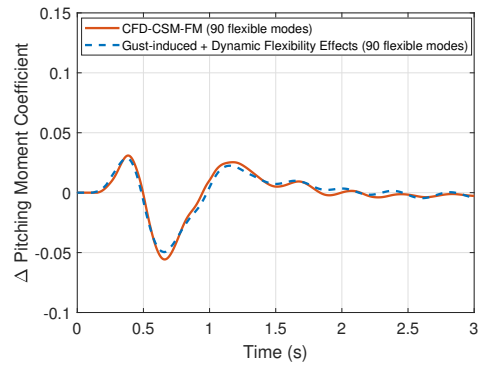


Figure 3.59: Pitching moment coefficient of free flexible A/C due to vertical gust (H=150ft)

Lateral Response

The impact of dynamic flexibility is also addressed in lateral. For the low frequency gust profile (H=300ft in figures 3.1 and 3.2), it is observed in figures 3.60 and 3.61 that very similar predicted responses are obtained both in roll and yaw with and without dynamic flexible effects. In this case, dynamic flexible effects could be neglected to reduce the number of states and computation cost of the model.

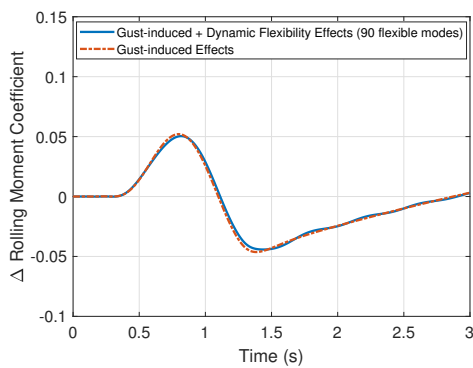


Figure 3.60: Rolling moment coefficient of free flexible A/C due to lateral gust (H=300ft)

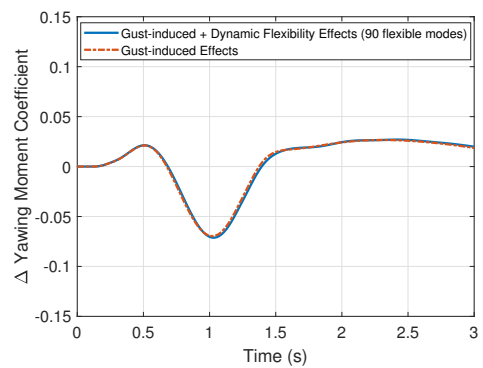


Figure 3.61: Yawing moment coefficient of free flexible A/C due to lateral gust (H=300ft)

The response for the gust profile which covers a higher frequency range (H=150ft in figures 3.1 and 3.2) shows higher differences between both approaches. The predicted response retaining different number of low frequency modes is compared with the same model with 90 flexible modes. In this case, 3 antisymmetric flexible modes are sufficient

to capture the dynamic flexible effect as shown in figures 3.62 and 3.63. The response in roll and yaw is attenuated due to the energy absorbed by the flexible modes.

Typical modes excited at low frequencies which have an impact on yawing and rolling moment coefficients are included in figure 3.64. Antisymmetric modes have an impact on the rolling moment by changing the lift force distribution on both sides of the wing. The antisymmetric bending of the fuselage modifies the sideslip of the VTP creating variations in the yawing moment coefficient in addition to the ones induced by the lateral gust profile. Attenuated responses and low amplitude oscillations are observed due to the excitation of these modes for the considered lateral gust. In this case, the impact of the rigid motion on the dynamic flexible response is also neglected.

The predicted responses included in figures 3.65 and 3.66 also show a very good agreement between the model-based and the high fidelity simulation approach at the considered flight condition.

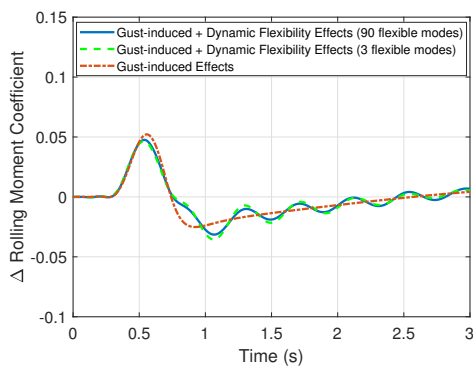


Figure 3.62: Rolling moment coefficient of free flexible A/C due to lateral gust (H=150ft)

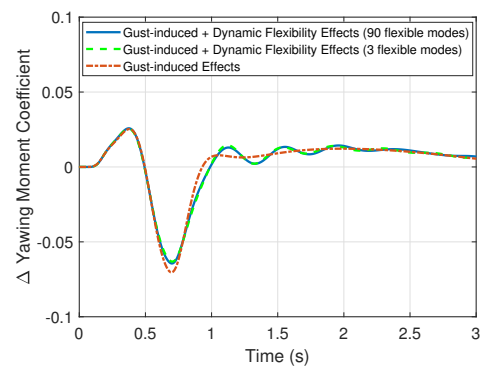


Figure 3.63: Yawing moment coefficient of free flexible A/C due to lateral gust (H=150ft)

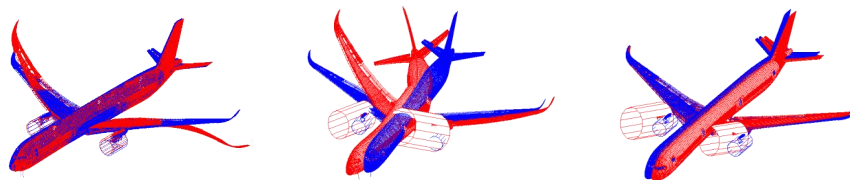


Figure 3.64: Low frequency modes which impact rolling and yawing moment coefficients (Wing and fuselage antisymmetric bending and engine antisymmetric modes with amplification factor)

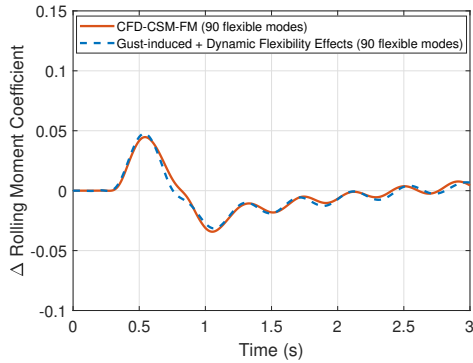


Figure 3.65: Rolling moment coefficient of free flexible A/C due to lateral gust (H=150ft)

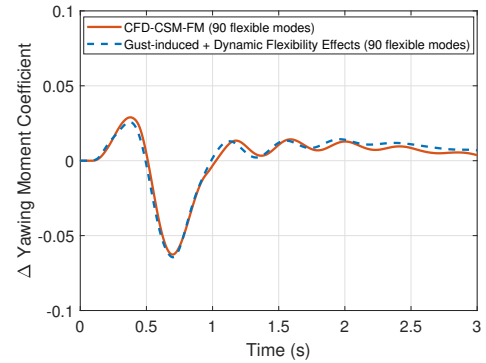


Figure 3.66: Yawing moment coefficient of free flexible A/C due to lateral gust (H=150ft)

Gust Frequency Analysis

Once the gust-induced and dynamic flexible effects are integrated in the flight dynamics equations of motion, the aircraft response can be evaluated for different frequencies. The aircraft response to gust is strongly dependent on the frequency range excited. In this part, the gust frequency effect on the overall aircraft response is analysed.

As shown in the previous section, dynamic flexible effects can be neglected at low frequencies and the hypothesis of quasi-static flexible aerodynamics is enough to capture the main effects. The gust profiles shown in the time and frequency domain in figures 3.67 and 3.68 are used to simulate the response of a quasi-steady flexible aircraft. These gust profiles are applied in vertical as angle of attack variations and in lateral as sideslip effect along the aircraft.

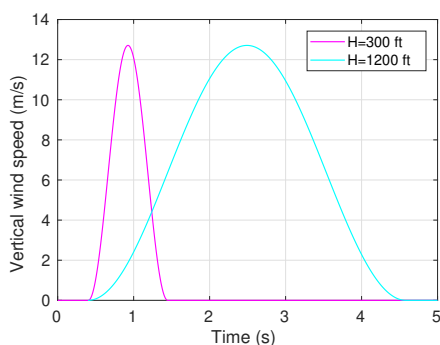


Figure 3.67: Gust profiles in time domain

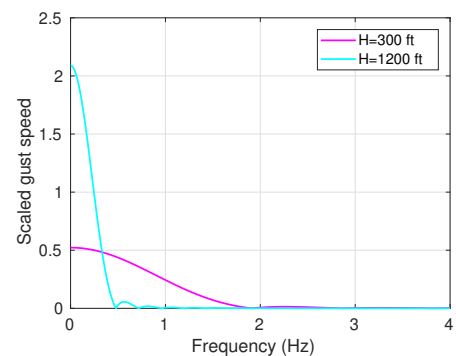


Figure 3.68: Gust profiles in frequency domain

The predicted response in vertical is shown in figures 3.69 and 3.70. Both gust profiles have the same amplitude as shown in figure 3.67. However, it can be observed that the increment of lift force coefficient and pitching moment is lower for the gust profile exciting the lower frequencies. At frequencies closer to the flight dynamics modes, the aircraft has enough time to react to the gust by attenuating part of the gust energy [65]. This energy absorbed in the aircraft response alleviate the gust loads transmitted to the structure.

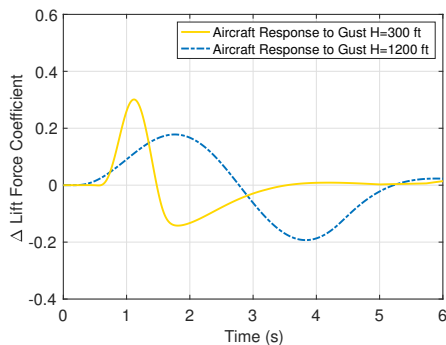


Figure 3.69: Lift coefficient of quasi-steady flexible A/C due to different vertical gust profiles

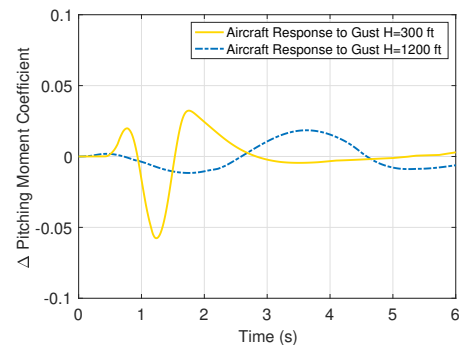


Figure 3.70: Pitching moment coefficient of quasi-steady flexible A/C due to different vertical gust profiles

Inertial effects are added to illustrate the difference. The vertical load factor and the pitch angle are shown in figures 3.71 and 3.72. The response in vertical load factor show the same behaviour as the increment of lift force coefficient, as both are directly related. The response in pitch show how the aircraft is able to follow in pitch the gust profile absorbing part of the gust energy.

Even if the aircraft response is more important at low frequencies, the level of loads seen by the structure which is linked with the vertical load factor is attenuated as seen in figure 3.71 by the reduction of the first peak. This illustrates the different load alleviation and flight dynamics objectives and the compromise required to achieve them. The aircraft motion is interesting for load alleviation to attenuate part of the energy transmitted by the gust. However, if the aircraft is controlled in a way to avoid motion due to gust, higher loads are to be expected. At higher gust frequencies, the aircraft has less time to react to the gust excitation and higher aerodynamic loads due to the gust effect are transmitted to the structure. This does not involve that higher loads appear at higher frequencies. As seen in the previous section, at higher frequencies, the excitation of the flexible modes also absorbs part of the energy reducing the level of loads. Furthermore, certification regulations establish lower gust amplitudes at higher frequencies based on experience.

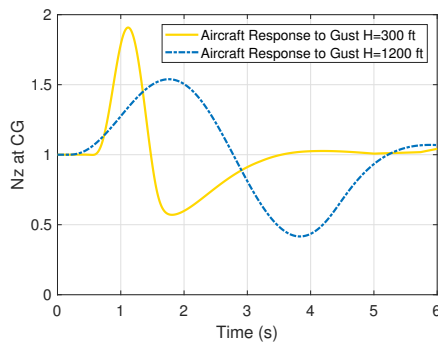


Figure 3.71: Vertical load factor of quasi-steady flexible A/C due to different vertical gust profiles

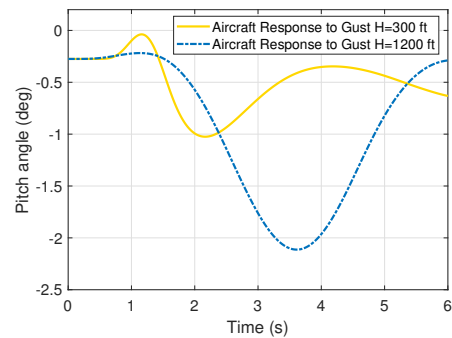


Figure 3.72: Pitch angle of quasi-steady flexible A/C due to different vertical gust profiles

The same conclusion can be observed in lateral. The initial peak of the lateral load factor due to the gust effect shown in figure 3.73 is lower for the response due to the gust profile exciting lower frequencies. At the same time, the aircraft response is more important as seen through the roll angle in figure 3.74.

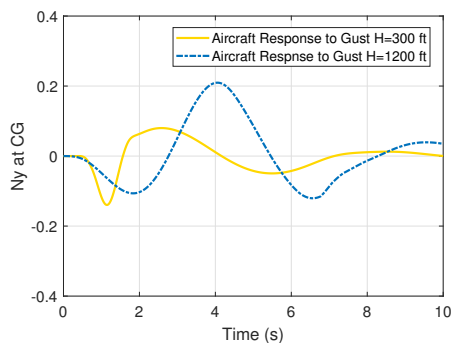


Figure 3.73: Lateral load factor of quasi-steady flexible A/C due to different lateral gust profiles

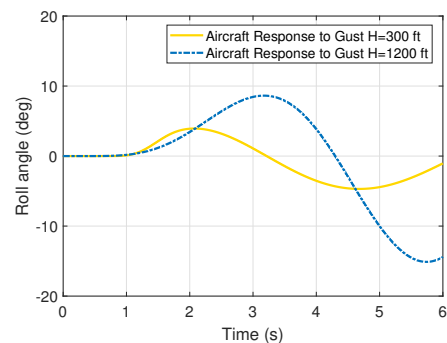


Figure 3.74: Roll angle of quasi-steady flexible A/C due to different lateral gust profiles

In this case, the excited mode which is able to follow the gust excitation and reduce the lateral loads due to the gust is the dutch roll, which affects both roll and yaw as shown in figures 3.75 and 3.76 through the oscillations in roll and yaw rate. These oscillations occur due to the yaw stability which tends to bring back the aircraft to zero sideslip for a given variation. This motion is periodic and also affects roll due to the strong coupling between both axes. For a given harmonic yaw motion, the local velocity and incidence in both sides of the wing changes creating roll motion. These oscillations can be controlled and reduced through a yaw damper consisting of rudder deflections according to measures in yaw rate.

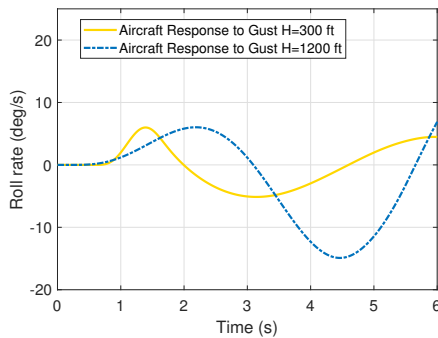


Figure 3.75: Roll rate of quasi-steady flexible A/C due to different vertical gust profile

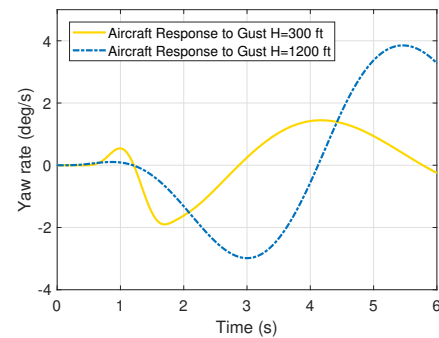


Figure 3.76: Yaw rate of quasi-steady flexible A/C due to different vertical gust profile

When exciting higher frequencies, dynamic flexible effects become important as some flexible modes are excited. However, the main effect on the overall aircraft response can be captured by keeping a low number of flexible modes. In this part, the frequency range excited in the previous section is increased as shown in figures 3.77 and 3.78.

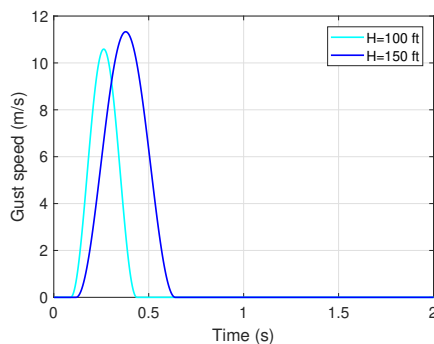


Figure 3.77: Gust profiles in time domain

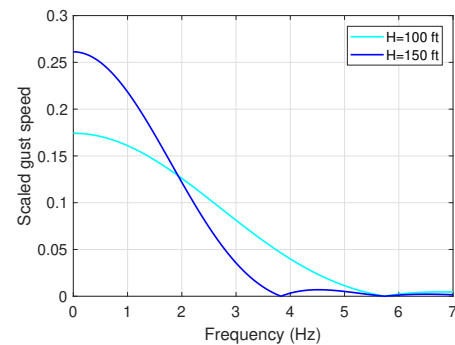


Figure 3.78: Gust profiles in frequency domain

The predicted response in vertical and lateral is shown in figures 3.79, 3.80, 3.81 and 3.82. Even if additional flexible modes are excited, its effect on the overall aircraft response is low. Keeping the flexible modes shown in figure 3.57 for vertical and 3.64 for lateral is enough to capture a response very close to the same model with 90 flexible modes. As the frequency increases, the flexible modes are less energetic and more concentrated on local parts affecting only specific components. As the aircraft is less sensitive to atmospheric disturbances at high frequencies, the range studied in this case seems sufficient to conclude that for the aircraft configuration considered, keeping these 6 flexible modes (3 symmetric in vertical and 3 antisymmetric in lateral) is enough to capture the aircraft response due

to gust and turbulence for different kind of flight dynamics investigations. This needs to be evaluated for each aircraft configuration studied.

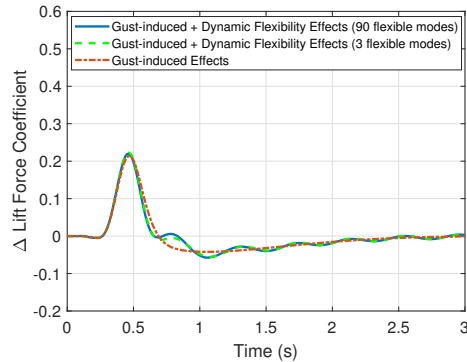


Figure 3.79: Lift coefficient of free flexible A/C due to vertical gust (H=100ft)

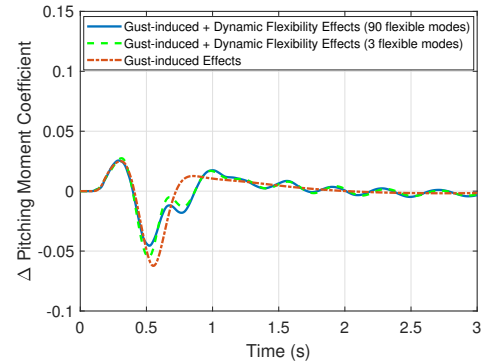


Figure 3.80: Pitching moment coefficient of free flexible A/C due to vertical gust (H=100ft)

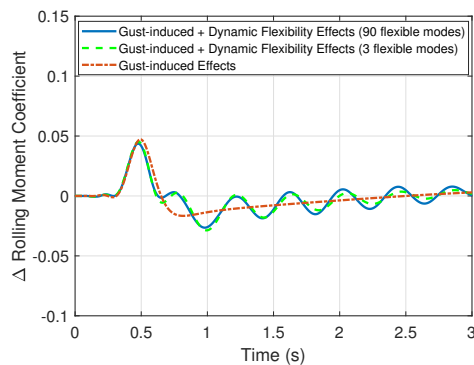


Figure 3.81: Rolling moment coefficient of free flexible A/C due to lateral gust (H=100ft)

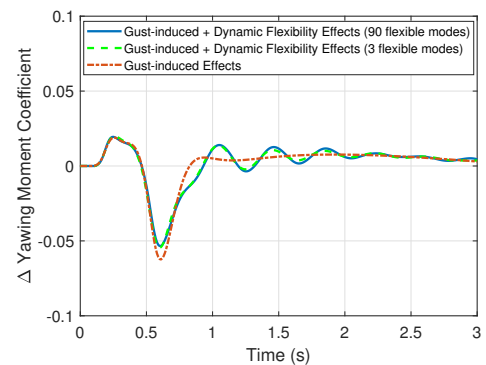


Figure 3.82: Yawing moment coefficient of free flexible A/C due to lateral gust (H=100ft)

3.5 Transonic Conditions

All the previous results are shown at the same flight condition, at low Mach and altitude ($M=0.5$, $h=0\text{ft}$). This section extends the analysis of the aircraft response to theoretical gusts to different conditions. In particular, closer to cruise at higher Mach numbers in which transonic effects such as shock motion during the gust encounter can affect the overall predicted aerodynamic response. The results in this section show some differences with respect to the previous analysis done at lower Mach numbers.

Vertical Response

The same process as the one detailed previously is followed in order to generate the model in the different flight condition. In this case, the flight point studied is $M=0.836$ and altitude 27000ft. Figure 3.83 and 3.84 shows the GAF in lift and pitch. A rational function approximation is also applied to express the unsteady aerodynamic forces from CFD-LFD in the time domain, with 10 delay coefficients. The differences between DLM and CFD-LFD depend on the DLM correction. In this case, DLM has been corrected to match the values of CFD-LFD at low frequencies. Higher accuracy is expected with CFD-LFD which takes into account the steady condition including steady shocks and low amplitude shock motion around the nonlinear steady state.

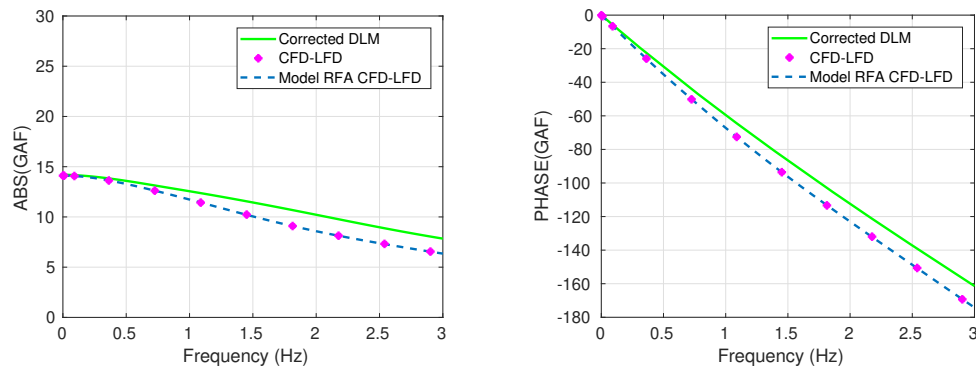


Figure 3.83: GAF in lift due to vertical gust

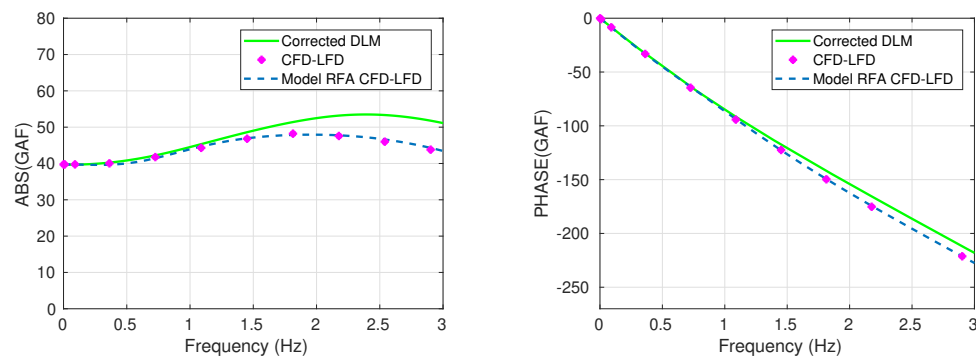


Figure 3.84: GAF in pitch due to vertical gust

The increment of pitch and lift due to a theoretical gust predicted by the model is also compared with nonlinear CFD in the time domain for a fixed rigid aircraft. The gust profile

considered is the one exciting the low frequency range ($H=300\text{ft}$ in figures 3.1 and 3.2). The amplitude used for the nonlinear simulation in the time domain has been reduced by a factor of 10^3 and the results obtained have been scaled to avoid any aerodynamic nonlinear effect. Figures 3.85 and 3.86 show a very good agreement in the predictions of increment of lift and pitch. Aerodynamic nonlinear effects are not expected when exciting the aircraft at these conditions with low amplitude atmospheric disturbances and CFD-LFD is able to capture a response very close to nonlinear CFD in the time domain.

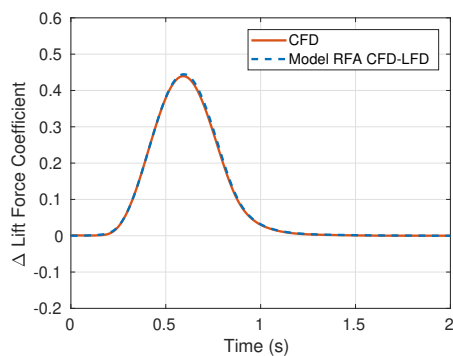


Figure 3.85: Lift coefficient of fixed rigid A/C due to vertical gust ($H=300\text{ft}$)

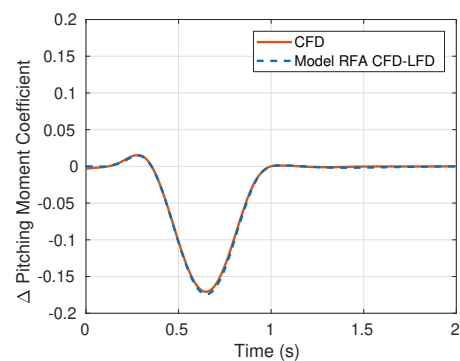


Figure 3.86: Pitching moment coefficient of fixed rigid A/C due to vertical gust ($H=300\text{ft}$)

The increment of pressure coefficient distribution (ΔC_p) is calculated at the wing station of figure 3.87 through nonlinear CFD at different time steps. Results are shown in figure 3.88. The steady pressure coefficient is removed and the increment with respect to the initial conditions is shown. Even if the steady condition includes a shock, the gust effect can be considered as linear as observed by the ΔC_p distributions at the different time steps.

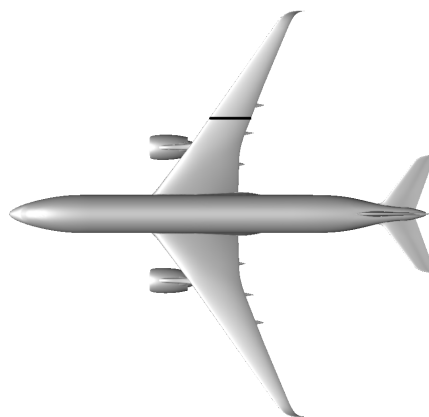


Figure 3.87: Wing station at which the increment of pressure coefficient (ΔC_p) is calculated

A similar linear distribution is obtained in the previous flight condition ($M=0.5$, $h=0\text{ft}$) with the nominal gust amplitude as shown in figure 3.89. It can be observed that the gust effect is linearly scaled taking into account the steady condition which differs in both cases, even if the gust excitation is the same.

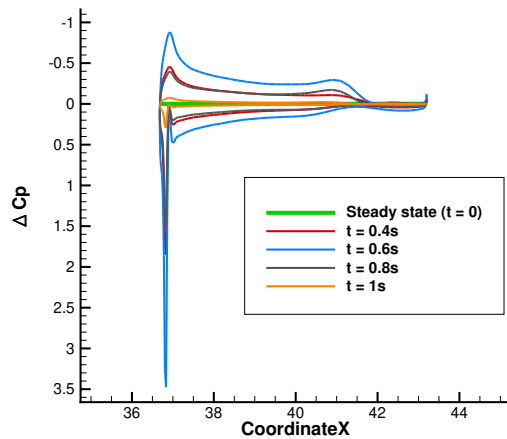


Figure 3.88: Increment of C_p distribution due to a low amplitude gust profile (scaled) with respect to the steady condition at different time steps for a fixed rigid A/C ($M=0.836$, $h=27000\text{ft}$)

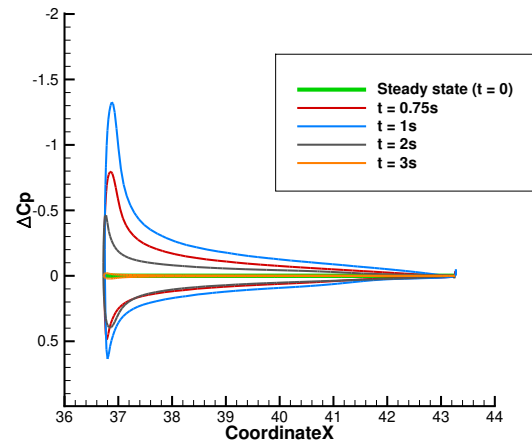


Figure 3.89: Increment of C_p distribution with respect to the steady condition at different time steps for a fixed rigid A/C ($M=0.5$, $h=0\text{ft}$)

Aerodynamic Nonlinear Assessment

At high Mach conditions, aerodynamic nonlinear effects may appear at low angle of attack variations. The same gust profile as the one used to predict the response in figures 3.85 and 3.86 at the nominal amplitude is applied at the same flight conditions ($M=0.836$, $h=27000\text{ft}$). The same increment of pressure coefficient (ΔC_p) distribution at the wing station of figure 3.87 is shown in figure 3.90. The nonlinear behaviour in the gust effect can be observed. It is mainly governed by the shock motion along the chord. This effect cannot be predicted by CFD-LFD as previously published [49]. In this case, the impact on the predicted loads is not quantified.

The effect of the nonlinearity on the overall aircraft response is evaluated. Even if the shock motion is not captured by CFD-LFD, the model is able to predict an overall aircraft response close to nonlinear CFD as shown in figures 3.91 and 3.92 for lift and pitch. Small differences can be observed in the predicted increment of pitching moment coefficient.

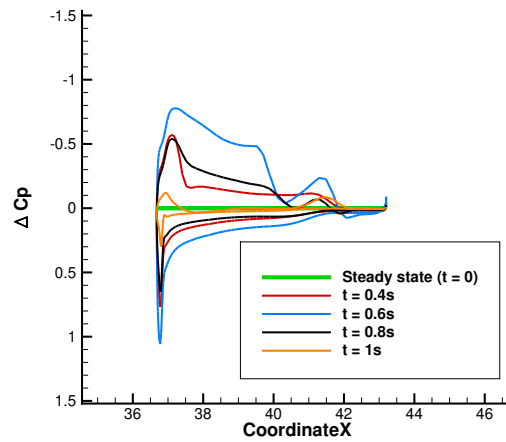


Figure 3.90: Increment of C_p distribution with respect to the steady condition at different time steps for a fixed rigid A/C ($M=0.836$, $h=27000\text{ft}$)

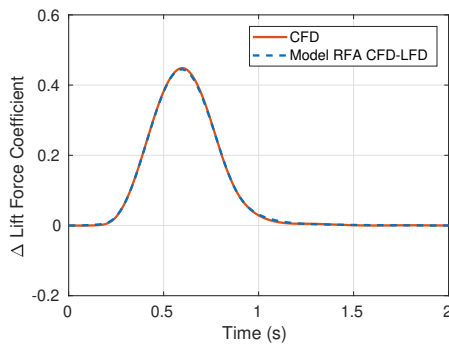


Figure 3.91: Lift coefficient of fixed rigid A/C due to vertical gust ($H=300\text{ft}$)

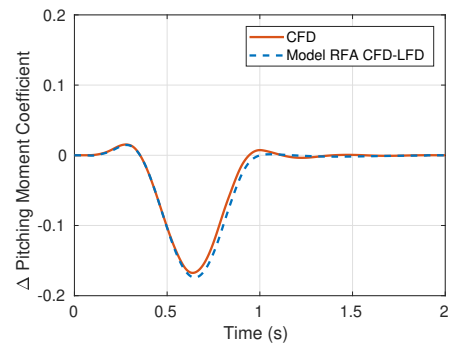


Figure 3.92: Pitching moment coefficient of fixed rigid A/C due to vertical gust ($H=300\text{ft}$)

In this case, the shock motion and strong adverse gradient of pressure, weakens the flow at the wing outer region without reaching separation as shown in figure 3.93 through the streamlines in the affected region. This behaviour cannot be predicted by the model, but the differences in the response are small and could be neglected.

As the curve of the lift force coefficient as a function of steady angle of attack shows in figure 3.94, the nonlinear behaviour appears at relatively small angles of attack when compared to flight conditions at lower Mach numbers. However, in this case, there is no separation as the increment of angle of attack due to the gust is of 3.6° and the steady angle of attack is of 0.25° .

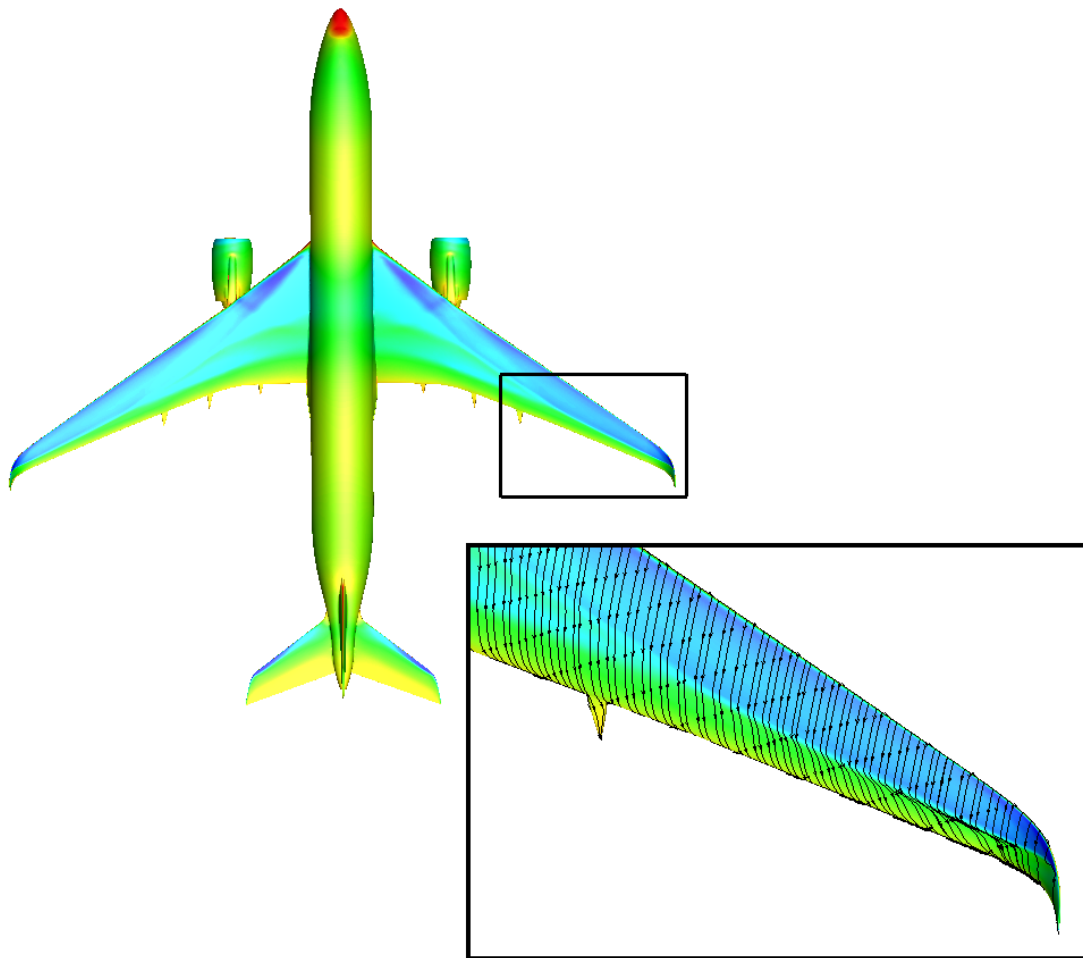


Figure 3.93: Pressure distribution when the maximum amplitude of the gust disturbance reaches the wing and zoom to the outer wing region where flow weakens

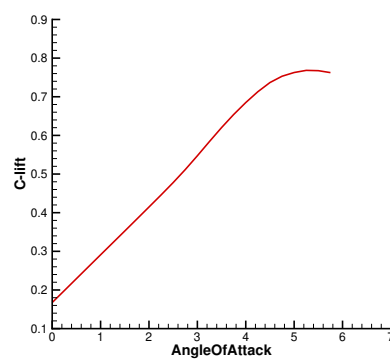


Figure 3.94: Lift force coefficient as a function of the steady angle of attack ($M=0.836$, $h=27000\text{ft}$)

When increasing the amplitude of the excitation, nonlinear effects become more important. The previous gust amplitude has been slightly increased to evaluate the effect of the nonlinearity on the overall aircraft response. Figures 3.96 and 3.97 show the predicted increment of lift force and pitching moment coefficient in these conditions. Differences between the model generated from CFD-LFD simulations and nonlinear CFD are higher than in previous cases for both in lift and pitch. In this case, the increment of angle of attack due to the gust is of 5° reaching the nonlinear region as shown in figure 3.94. In particular, a local separation appears at the outer wing region as a consequence of the strong shock and adverse gradient of pressure created by the increase of angle of attack due to the gust. This effect is shown in figure 3.95 through the streamlines in the separated region.

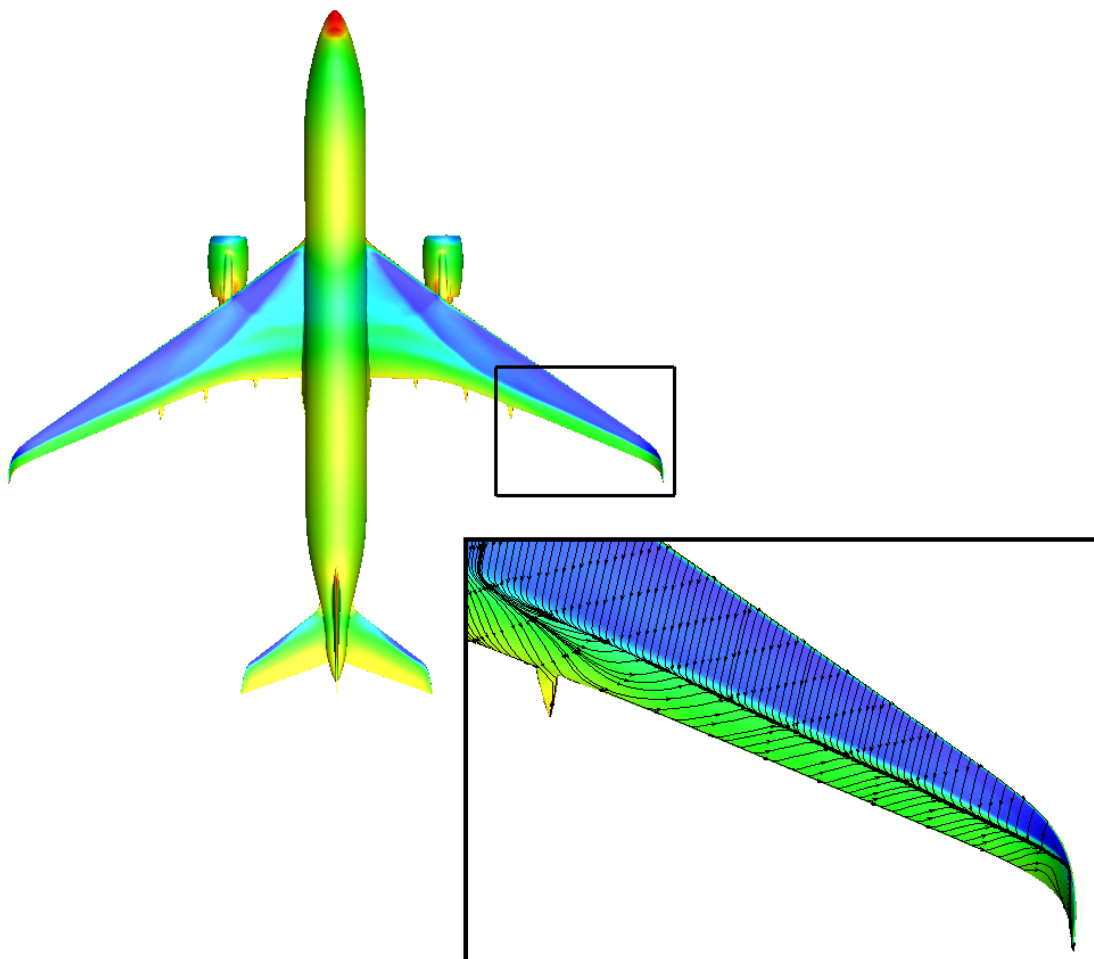


Figure 3.95: Pressure distribution when the maximum amplitude of the gust disturbance reaches the wing and zoom to the outer wing region where local stall appears

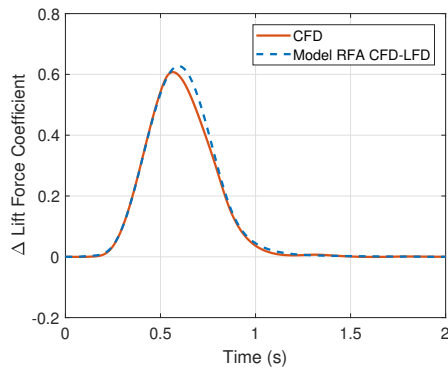


Figure 3.96: Lift coefficient of fixed rigid A/C due to vertical gust (H=300ft)

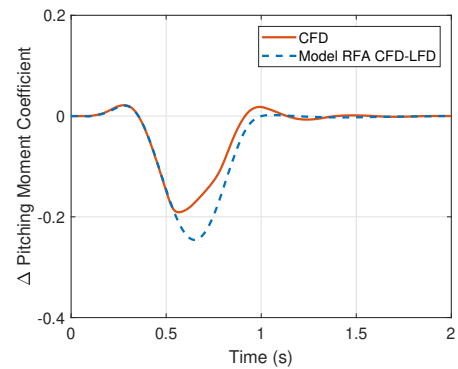


Figure 3.97: Pitching moment coefficient of fixed rigid A/C due to vertical gust (H=300ft)

The frequency of the excitation also influences the nonlinear response. At low frequencies, the response is close to the one predicted by nonlinear quasi-steady nonlinearities as shown in figure 3.94. At higher frequencies, the aerodynamic flow takes some time to establish increasing the unsteady lags in the response. In these cases, local separation or stall occurs at higher angles of attack than the ones predicted by the quasi-steady theory. This effect can be observed in figures 3.98 and 3.99. The same gust amplitude as the one creating an increment of angle of attack of 5° is applied with a reduced wavelength in order to excite higher frequencies (H=150ft in figures 3.1 and 3.2). In this case, local separation does not appear for the same angle of attack variation as the previous one. As shown in figures 3.98 and 3.99, the model from CFD-LFD and nonlinear CFD have a good agreement in the predicted lift force and pitching moment coefficient. This shows that the aerodynamic nonlinear response depends both on the gust amplitude and frequency.

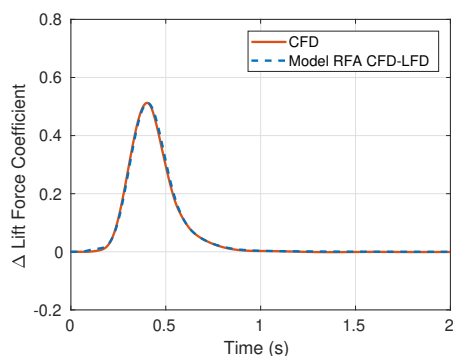


Figure 3.98: Lift coefficient of fixed rigid A/C due to vertical gust (H=150ft)

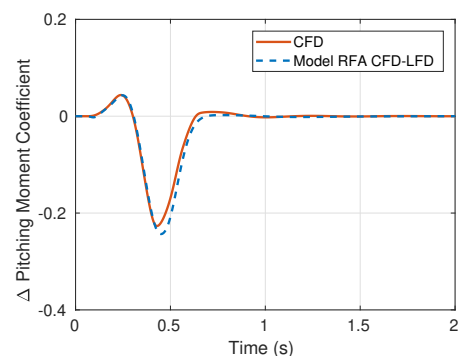


Figure 3.99: Pitching moment coefficient of fixed rigid A/C due to vertical gust (H=150ft)

The effect of nonlinearities is stronger for a fixed rigid aircraft than for a free flexible aircraft. The same cases are simulated for a free flexible aircraft in order to evaluate the effect of the damping of the aircraft reaction through the rigid and flexible motion. Figures 3.100 and 3.101 show the increment of predicted lift force coefficient and pitching moment coefficient due to the gust profile which creates an increase of angle of attack of 3.6° and the same excitation with the amplitude divided by a factor of 10^3 and then scaled to avoid aerodynamic nonlinear effects. The good agreement between both responses confirm the possibility to capture the gust-induced effects in the overall aircraft response with a model from linearized CFD in cases where shock motion appears without separation.

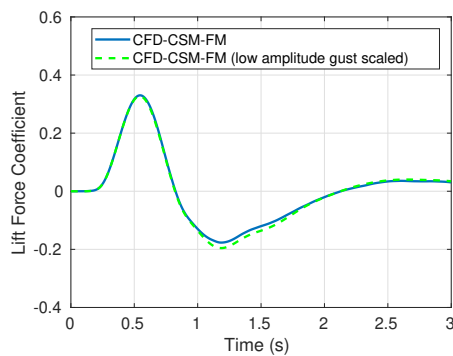


Figure 3.100: Lift coefficient of free flexible A/C due to vertical gust (H=300ft)

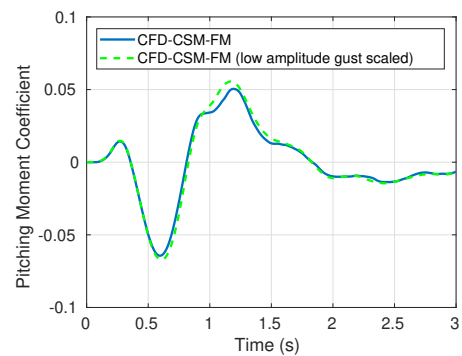


Figure 3.101: Pitching moment coefficient of free flexible A/C due to vertical gust (H=300ft)

Figures 3.102 and 3.103 show the pressure coefficient increment from the steady condition at the same wing station of the free flying flexible aircraft with a gust amplitude creating an angle of attack variation of 3.6° and the same excitation divided by a factor of 10^3 and then scaled. The response is attenuated and the maximum values are reduced when compared to the same case for a fixed rigid aircraft in figure 3.90. The shock motion and adverse gradient of pressure is less severe and the flow weakening shown in figure 3.95 is less important in this case.

The previous case in which local separation in the outer wing region appears has been also simulated for a free flying flexible aircraft. The aircraft rigid and flexible motion due to the gust excitation attenuate the increment of angle of attack due to the gust and there is no separation in this case. Figures 3.104 and 3.105 show the increment of lift force and pitching moment coefficient due to the gust creating an angle of attack variation of 5° and the same excitation divided by a factor of 10^3 and then scaled to avoid any nonlinear aerodynamic effect. The good agreement shows that aerodynamic nonlinearities do not appear during the gust encounter. Weak local separation appears due to the flexible motion at the outer wing section once the gust has gone as shown by the small differences

in the pitching moment coefficient. This shows that in nonlinear cases, the effect of the gust and the aircraft motion cannot be superimposed and both need to be taken into account simultaneously.

In conclusion, the model built from CFD-LFD results is expected to capture the gust-induced effects in cases where shock motion does not appear creating local stalls. As long as the shock motion is not important enough, LFD and nonlinear CFD are expected to predict similar responses at high Mach numbers for different gust disturbances.

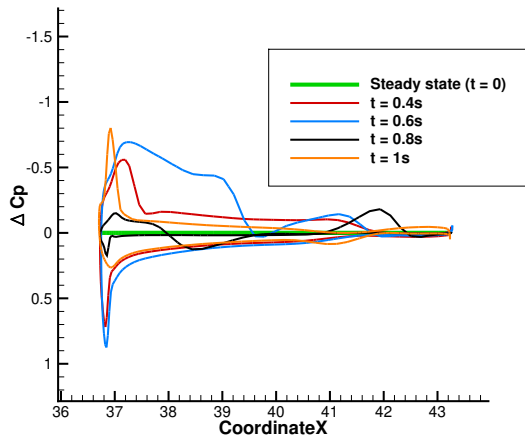


Figure 3.102: Increment of C_p distribution with respect to the steady condition at different time steps for a free flexible A/C ($M=0.836$, $h=27000ft$)

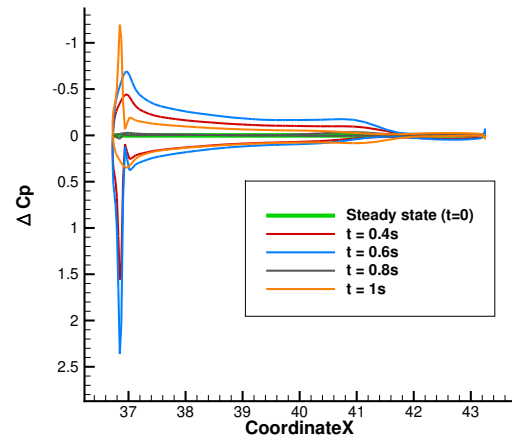


Figure 3.103: Increment of C_p distribution due to a low amplitude gust profile (scaled) with respect to the steady condition at different time steps for a free flexible A/C ($M=0.836$, $h=27000ft$)

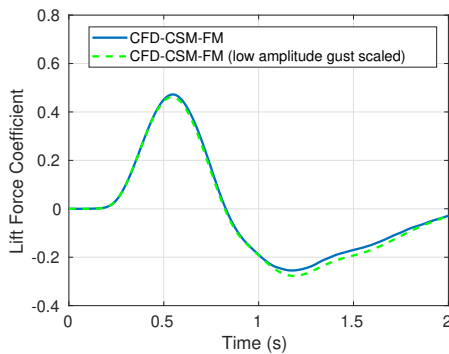


Figure 3.104: Lift coefficient of free flexible A/C due to vertical gust ($H=150ft$)

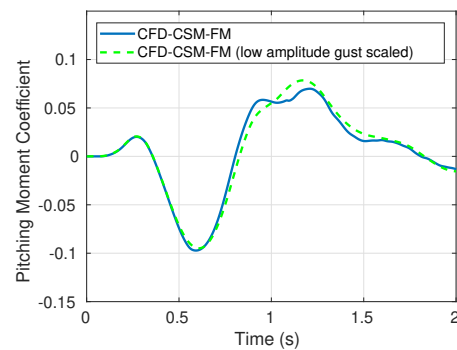


Figure 3.105: Pitching moment coefficient of free flexible A/C due to vertical gust ($H=150ft$)

Mach Effect

In Mach cases in-between the analysed values, the GAF has been also calculated in order to parametrise the model. At higher Mach numbers and keeping the altitude constant, the speed increases and the gust propagation effect becomes less important. This can be seen in figure 3.106.

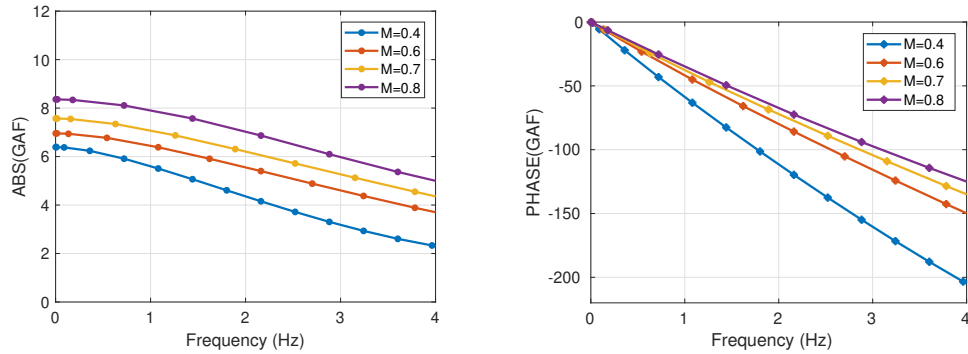


Figure 3.106: GAF in lift due to vertical gust for different Mach

In order to show the Mach effect without the influence of changes in speed, the GAF is plotted against reduced frequency (with an alternative definition in this case: $k = \frac{\pi l_{ref} f}{V_\infty}$, with l_{ref} being the mean aerodynamic chord, V_∞ the true airspeed and f the physical frequency). As shown in figure 3.107, the aerodynamic lags due to unsteady aerodynamic effects increase at high Mach. The Mach effect in pitch can also be taken into account as shown in figure 3.108. It can be observed that the main differences between the plots come from the Mach effect on the quasi-steady gradients at low frequencies.

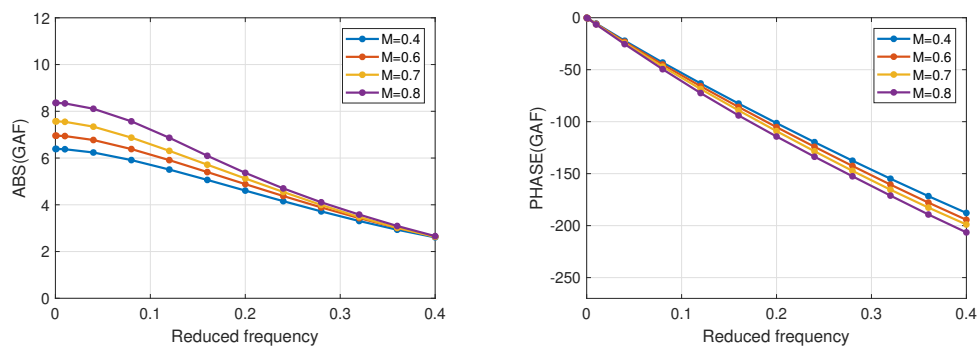


Figure 3.107: GAF in lift due to vertical gust for different Mach

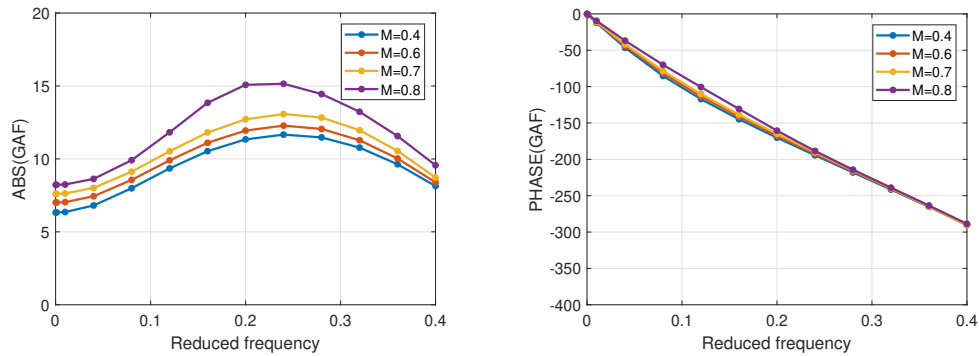


Figure 3.108: GAF in pitch due to vertical gust for different Mach

The previous presented model can be adapted with different data files for different Mach numbers as shown in figures 3.106, 3.107 and 3.108 in the Mach validity range of the model by taking into account the effects previously mentioned. The possibility to increase the accuracy of a model based approach at higher Mach conditions close to nonlinear conditions is a recommended point for future work. The goal of this section was to evaluate possible model limitations at different flight conditions. Further convergence studies and evaluation of different turbulence models would be required for accurate prediction of nonlinear effects with CFD. Wind tunnel tests could also be useful for a further study.

Chapter 4

Atmospheric Turbulence

In this chapter, the same approach is applied to simulate the response of the previous generic aircraft configuration to different atmospheric turbulence. The analysis is initially focused on theoretical spectrum before testing the model with turbulence reconstructed from flight test measures. This study is not focused on reconstruction techniques to estimate the turbulence input. Uncertainties are expected in the measured turbulence as well as the predicted response from this input. The effect of possible turbulence variations along the wingspan is discussed at the end.

In this section, the aircraft response is analysed in terms of accelerations and angular motions and speeds instead of aerodynamic force and moment coefficients. This takes into account the mass and inertia effects on the aircraft response, apart from the aerodynamic contribution. Inertial outputs such as accelerations and angular speeds can be directly extracted from flight test measures.

4.1 Theoretical Turbulence

Appart from the theoretical discrete gust profile presented in the previous section, there are other possibilities to characterise atmospheric disturbances. Another input is proposed in certification requirements [3] in order to account for continuous and irregular turbulence effects. The atmospheric disturbance in this part is idealized as a stationary Gaussian random process [4]. The term stationary means that the profile is considered to be infinite with constant statistical properties. Gaussian profile refers to the fact that when sampling the excitation defined in the time domain, the resulting probability distribution is Gaussian, or also referred to as normal distribution. The turbulence profile is also random because it does not follow any pattern and it can only be defined by its statistical characteristics. Additional details are provided in [4].

In this part, the previous presented modelling strategy is applied to predict the aircraft response to theoretical turbulence and different possible assumptions are evaluated. In this case, it is assumed that aerodynamic nonlinearities are not expected. The flight condition studied is the one at low Mach and altitude ($M=0.5$, $h=0\text{ft}$) and the turbulence amplitude is low in order to remain at the linear region. The assumption of unidimensional turbulence profile is done. However, the effect of possible vertical variations along the wingspan is evaluated at the end of this chapter.

Von Karman Turbulence Spectrum

A commonly used theoretical turbulence spectrum is the Von Karman. The mathematical expression of the power spectral density (PSD) of the Von Karman velocity profile is given in equation 4.1, with σ_t being the root-mean-square turbulence velocity in m/s (gust intensity), L the characteristic scale wavelength of the turbulence and ω the frequency in rad/s. The power spectral density provides the information of the frequency content of the turbulence input [4].

$$\Phi_k(\omega) = \sigma_t^2 \frac{L}{V_\infty} \frac{1 + \frac{8}{3} 1.339^2 (\frac{L}{V_\infty})^2 \omega^2}{(1 + 1.339^2 (\frac{L}{V_\infty})^2 \omega^2)^{\frac{11}{6}}} \quad (4.1)$$

The considered input in the frequency and time domain is given in figures 4.1 and 4.2. The turbulence scale wavelength (L) is set to 2500ft according to norm MIL-F-8785C [66]. The norm also gives the turbulence intensities (σ_t) as a function of altitude and probability of exceedance. In this case, σ_t is set to 3 m/s corresponding to moderate turbulence (with a probability of exceedance of 10^{-3}) at low altitudes. It can be observed that the turbulence energy decreases as the frequency increases. This kind of behaviour has been verified with respect to measured data in flight [4].

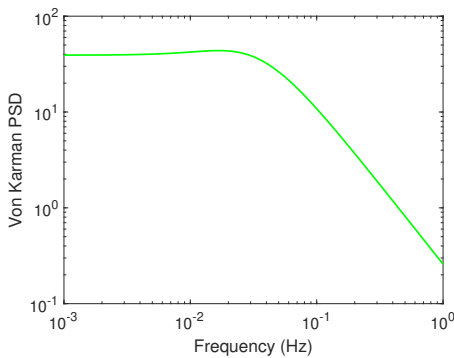


Figure 4.1: PSD Von Karman turbulence spectrum

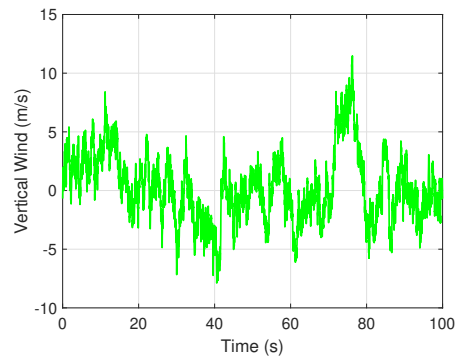


Figure 4.2: Continuous wind turbulence in the time domain given by the Von Karman spectrum

Vertical Response

The disturbance given by the Von Karman spectrum is applied as vertical turbulence input in the simulation. The model is evaluated in this section in order to predict the vertical response in these conditions. In this case, the aircraft is in open loop, which means that flight control laws do not react to control the response. The aircraft motion is only affected by the turbulence effect and natural aircraft response. Flight dynamic and flexible modes can be identified in the frequency domain by analysing the aircraft response in open loop. In this case, the effect of dynamic flexibility is also analysed.

The identification process to capture gust-induced effects proposed in [10] uses the frequency response functions due to turbulence around the peaks of the flight dynamics modes. The disadvantage of this approach is that the identified model becomes dependent on the turbulence scale length and aircraft mass properties. As it is also pointed out in [10], this can be overcome by identifying the model directly from the aerodynamic frequency responses as shown in chapter 3.

The predicted response is shown both in time and frequency domain. The solution in the time domain is obtained by imposing as input the turbulence profile expressed in the time domain as shown in figure 4.2. Different possibilities exist to calculate the power spectral density of the response. In this case, it is estimated from the solution in the time domain with 100s of simulation. The method of averaged periodograms is used. The response in the time domain is divided in different parts with a specific overlap between sections and a window is applied. Further details on the approach to estimate the power spectral density from samples in the time domain can be found in [67].

Another possibility typically used for loads analysis consist of calculating the power spectral density of the response from the frequency response function and the turbulence spectrum with the expression given in equation 4.2, with $|H_y(\omega)|^2$ being the modulus squared value of the aircraft frequency response in turbulence and $\Phi_k(\omega)$ the turbulence PSD as defined in the case of the Von Karman spectrum with the expression given in equation 4.1.

$$\Phi_y(\omega) = H_y(\omega)\overline{H_y(\omega)}\Phi_k(\omega) = |H_y(\omega)|^2 \Phi_k(\omega) \quad (4.2)$$

The loads level in turbulence can be estimated by calculating the root-mean-square value of the response (σ_y), which is the area under the power spectral density of the response, given in equation 4.3.

$$\sigma_y = \sqrt{\int \Phi_y(\omega)d\omega} \quad (4.3)$$

The predicted response in pitch rate is shown in figures 4.3 and 4.4 in both the time and frequency domain through the power spectral density of the response. The same

model with the gust-induced effect limited to an angle of attack effect at low frequencies is also shown. As shown previously in figure 3.32, taking into account the gust-induced effect in pitch allows capturing the gust propagation effect along the aircraft which plays an important role in pitch. This is translated in the aircraft response due to turbulence by capturing higher frequencies as shown both in the time and frequency domain. The shape of the power spectral density is consistent with the one of the turbulence excitation as shown in figure 4.1. The peak shown in the response corresponds to the short period mode of the aircraft which is excited by the turbulence spectrum covering mainly the low frequency range.

The propagation effect can be also seen in the predicted vertical load factor in figure 4.5 through the delay between the nose and the wing, as previously shown in figure 3.31.

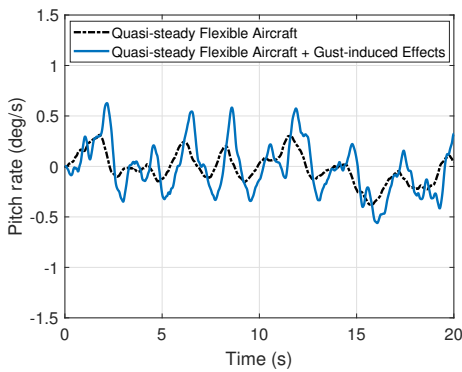


Figure 4.3: Pitch rate due to Von Karman turbulence spectrum ($L=2500\text{ft}$, $\sigma_t=3$)

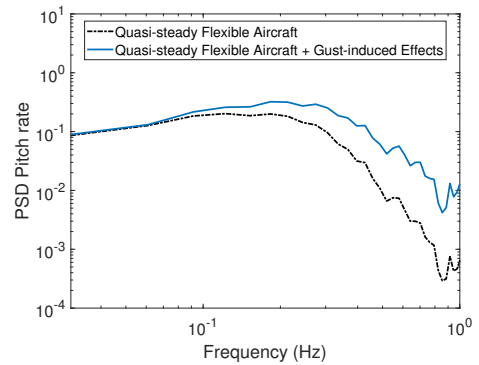


Figure 4.4: PSD pitch rate due to Von Karman turbulence spectrum ($L=2500\text{ft}$, $\sigma_t=3$)

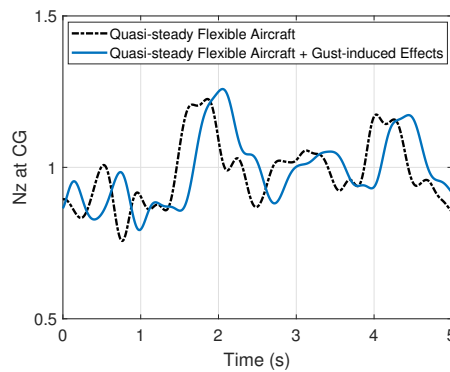


Figure 4.5: Vertical load factor due to Von Karman turbulence spectrum ($L=2500\text{ft}$, $\sigma_t=3$)

Lateral Response

The Von Karman spectrum is also applied as a lateral disturbance. The predicted response in lateral due to the turbulence induced effect can be seen for roll and yaw rate in figures 4.6, 4.7 and 4.8. Similarly to pitch, the turbulence effect in yaw allows taking into account higher frequencies in the response as seen both in the time and frequency domain. The predominant physics captured is the propagation effect which takes into account the delay between the nose and the VTP. The peak seen at low frequencies on the power spectral density corresponds to the dutch roll mode. The effect in roll is similar as in pitch as shown previously in figure 3.35. The wing is the main contribution in roll and the delay between the nose and the wing is captured when taking into account the turbulence effect as shown in figure 4.8.

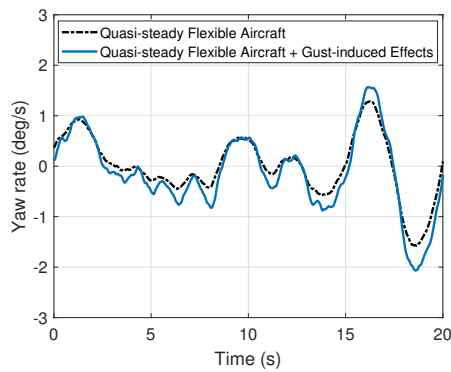


Figure 4.6: Yaw rate due to Von Karman turbulence spectrum ($L=2500\text{ft}$, $\sigma_t=3$)

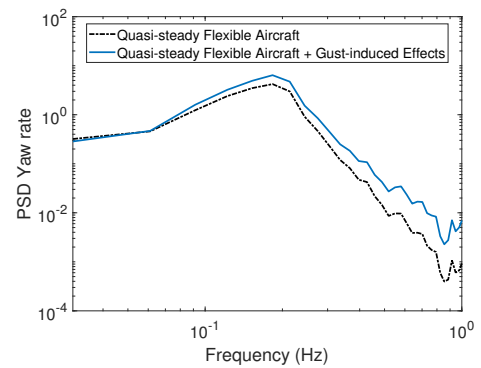


Figure 4.7: PSD yaw rate due to Von Karman turbulence spectrum ($L=2500\text{ft}$, $\sigma_t=3$)

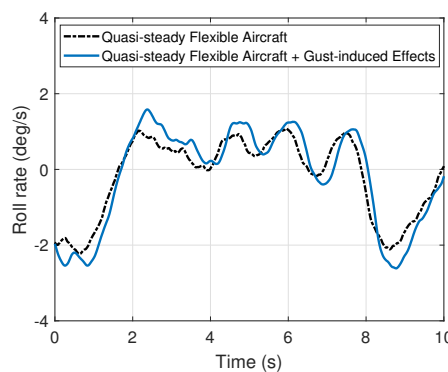


Figure 4.8: Roll rate due to Von Karman turbulence spectrum ($L=2500\text{ft}$, $\sigma_t=3$)

Dynamic Flexibility Effect

As shown previously, dynamic flexibility can have an impact on flight dynamics. For the previous turbulence profile given in figures 4.1 and 4.2, the effect of dynamic flexibility can be neglected. It can be observed that the frequency range excited given by the PSD of figure 4.1 is similar to the low frequency gust profile ($H=300\text{ft}$) given in figures 3.1 and 3.2. Quasi-static flexibility effects are sufficient to capture the response for the aircraft configuration studied and the frequency range excited, as shown in figures 3.53 and 3.54.

The frequency of the turbulence is increased in order to excite frequencies close to the low frequency flexible modes. The turbulence scale length (L) is reduced in order to excite a higher frequency range. The considered profile is not meant to represent any turbulence spectrum close to realistic ones. Figures 4.9 and 4.10 show the previous turbulence spectrum and the one with a lower scale length exciting higher frequencies. The turbulence intensity (σ_t) is kept constant in both cases (3 m/s).

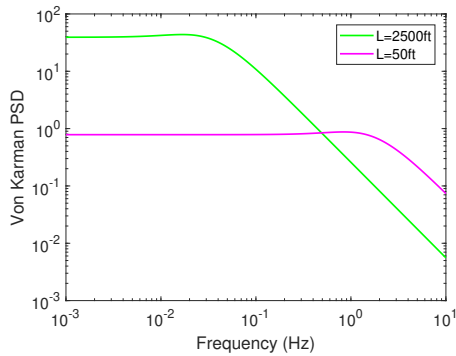


Figure 4.9: PSD Von Karman turbulence spectrum

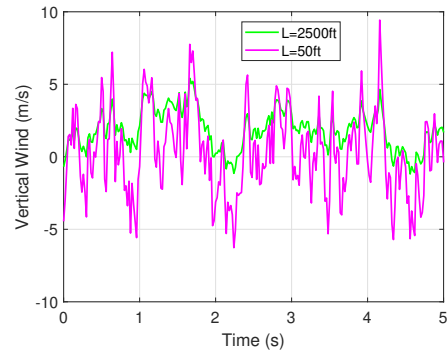


Figure 4.10: Continuous wind turbulence in the time domain given by the Von Karman spectrum

The predicted response in pitch in the time domain is shown in figures 4.11. Even when exciting higher frequencies, the response due to turbulence is still dominated by the low frequency flight dynamics, in particular the short period mode for the vertical response. The time step of the simulation in the time domain is of 0.01s, which is sufficient for flight dynamics analysis. This time step filters part of the response and lower time steps would be required to study effects at high frequencies.

The response in vertical load factor in the time domain is shown in 4.12. The excitation of low frequency flexible modes has an impact on the level of loads in turbulence calculated through the root-mean-square value of the PSD response (σ_y) with equation 4.3. Even if the impact of dynamic flexibility is higher in this case, the effect in the predicted response in the time domain for flight dynamics investigations can be neglected. The vertical load

factor at the centre of gravity is directly correlated with the gust or turbulence input. When comparing the predicted response in figure 4.12 and the excited profile in 4.10, it can be seen that the aircraft filters part of the turbulence frequencies through its flight dynamics response.

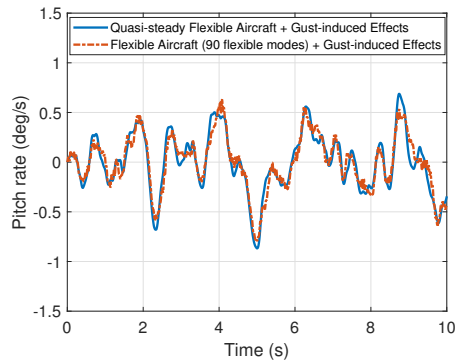


Figure 4.11: Pitch rate due to Von Karman turbulence spectrum ($L=50\text{ft}$, $\sigma_t=3$)

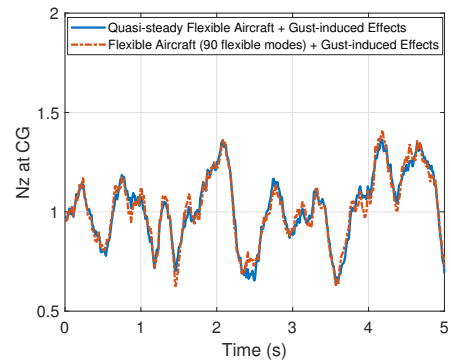


Figure 4.12: Vertical load factor due to Von Karman turbulence spectrum ($L=50\text{ft}$, $\sigma_t=3$)

The response in lateral due to the same turbulence profile has been calculated and is shown in figures 4.13 and 4.14 for roll and yaw in the time domain. Some high frequency oscillations at low amplitudes are observed in roll. However, the impact of dynamic flexibility on the global aircraft response is low and it could also be neglected as the response is mainly governed by the flight dynamics response. It is concluded that for flight dynamics investigations in continuous turbulence for typical profiles and the studied configuration, dynamic flexible effects can be neglected.

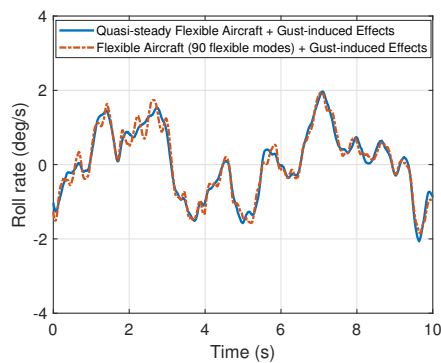


Figure 4.13: Roll rate due to Von Karman turbulence spectrum ($L=50\text{ft}$, $\sigma_t=3$)

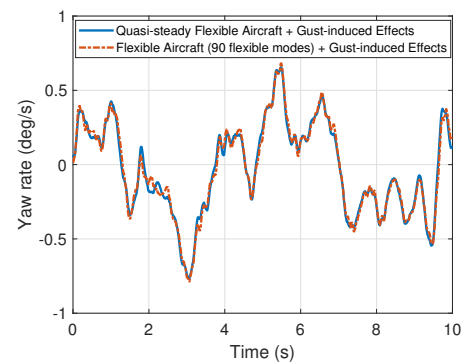


Figure 4.14: Yaw rate due to Von Karman turbulence spectrum ($L=50\text{ft}$, $\sigma_t=3$)

4.2 Realistic Atmospheric Turbulence

In this section, the aircraft response due to realistic atmospheric turbulence measured in flight is predicted. The same approach to integrate gust-induced effects in a flight dynamics model is used to simulate the aircraft response to realistic turbulence. Simulation results are compared with flight test measures to assess the introduced gust-induced effects. The model is applied to capture the turbulence contribution at low amplitudes and low Mach, in conditions where aerodynamic nonlinear effects are not expected to be important. The different approaches previously presented to express the gust-induced forces in the time domain through a rational function approximation have been tested with similar results.

The measure of turbulence velocity relative to the aircraft can be obtained by different methods. One of them consists of removing the effect of the aircraft motion to the measure from an angle of attack vane to separate the aircraft contribution due to its manoeuvre and the turbulence effect from the angle of attack variation. At frequencies higher to the frequency range of the flight dynamics modes, the aircraft motions are small and can be removed accurately. However, the separation of the effects at lower frequencies is more difficult and the amount of uncertainty in the turbulence measure is higher [4].

The turbulence profile is estimated in three different directions (aft, vertical and lateral) in geodetic reference frame. The profiles are measured in a specific point of the aircraft and the hypothesis that the profiles are constant along the wingspan is made. The predicted response is affected by the uncertainties related to this assumption. Figures 4.15 and 4.16 show an example of measured turbulence profile in the vertical direction in the time and frequency domain. It can be observed the similarities in terms of the frequency range excited with the von Karman turbulence spectrum in figures 4.1 and 4.2. The frequency range of interest in this case is between 0-1Hz. The impact of dynamic flexibility as observed in the previous section is low in this frequency range and it is neglected for this particular case.

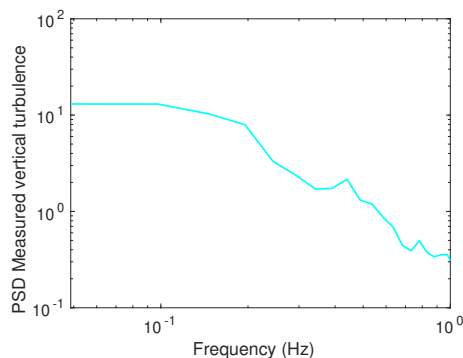


Figure 4.15: PSD vertical measured turbulence spectrum

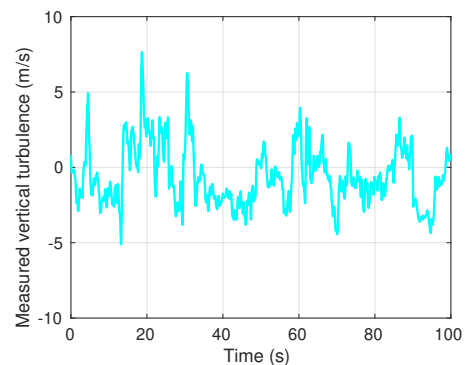


Figure 4.16: Vertical measured turbulence in the time domain

Vertical Response

The simulation results in the time domain are compared with flight test measures in figures 4.17 and 4.19. Results from the same model limited to low frequencies without gust propagation and unsteady aerodynamic effects are also shown. The predominant physics captured is the gust propagation effect along the aircraft, which plays an important role in pitch as previously shown. The turbulence profile has an effect on the different parts of the aircraft at different times. The predicted response in vertical load factor at the centre of gravity (figure 4.19) also shows the propagation effect through the delay between the nose and the wing. The wing is the main contributor to lift and therefore to the vertical load factor.

The power spectral density in pitch (PSD) is included as well showing a good agreement between the model prediction and the flight test data in the frequency range of interest for flight dynamics investigations (Figure 4.18).

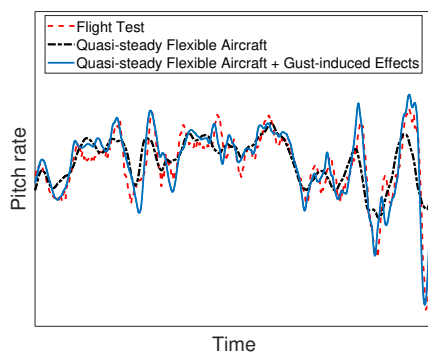


Figure 4.17: Pitch rate due to turbulence

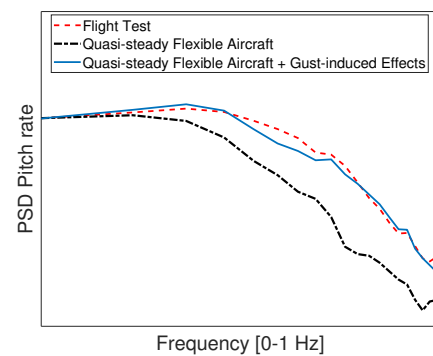


Figure 4.18: PSD pitch rate due to turbulence

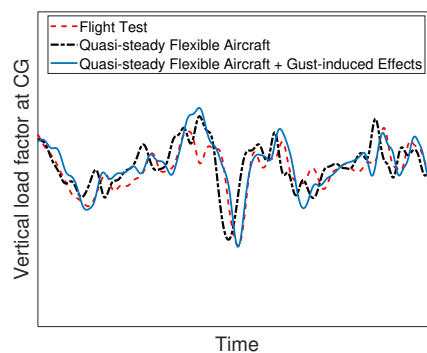


Figure 4.19: Vertical load factor at CG due to turbulence

Lateral Response

The lateral aircraft response to realistic turbulence is also simulated as shown in figure 4.20. The input is the same as the one considered previously for the vertical response. However, the relevant component in this case is the lateral turbulence measure.

Similarly to pitch, the predominant physics captured is the gust propagation effect between the nose and the aircraft VTP. As occurs with the HTP in pitch, the VTP provides the main effect in yaw. The delay between the nose and VTP need to be captured for accurate responses. The power spectral density in yaw (PSD) also shows a good agreement in the frequency range of interest (Figure 4.21).

The uncertainties related to the measure of turbulence have a stronger impact on lateral than vertical, mainly due to the important effect of the turbulence variation along the wingspan on roll. The response in roll due to realistic turbulence is analysed in the next section with the impact of turbulence variations along the wingspan.

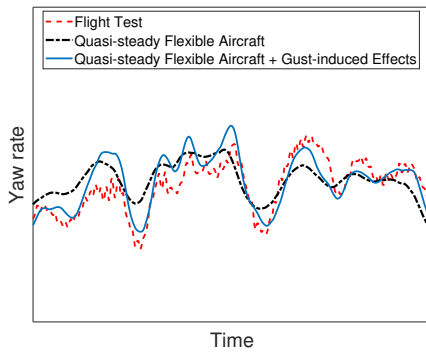


Figure 4.20: Yaw rate due to turbulence

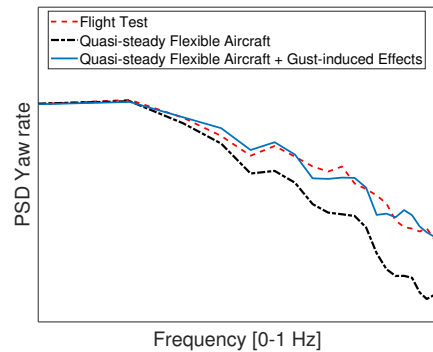


Figure 4.21: PSD yaw rate due to turbulence

4.3 Effect of Turbulence Variation Along the Wingspan

The gust and turbulence profiles in previous sections are considered to vary only along the flight path, being the so called one-dimensional profiles. However, as turbulence is considered to be isotropic, the lateral or vertical variation along the wingspan is supposed to be consistent with the variation along the flight path. Different possibilities are available to take into account multidimensional turbulence profiles through the aircraft models [10, 11, 42]. The complexity comes when trying to extract the multidimensional wind profile from flight measures to be used as input for the model. Uncertainties with respect to the measure of turbulence variation along the wingspan have a strong impact in the predicted response in roll as previously published [68, 69]. The spanwise variation of the vertical turbulence

contributes to the aircraft rolling moment although the predominant contribution is the lateral gust component [4].

The parameter λ/b is proposed by Hoblit [4] to evaluate the importance of spanwise effects when using one-dimensional profiles, where λ is the gust wavelength ($\lambda = 2\pi/\Omega = V_\infty/f$) and b is the aircraft wingspan. At low speeds, spanwise effects become more relevant. The effect of spanwise variation can be neglected in cases where $\lambda/b \gg 1$. The strong impact of turbulence spanwise variations in loads for high aspect ratio wing configurations is detailed in [70].

A similar case of realistic atmospheric turbulence as the one presented in the previous section is considered in order to evaluate the uncertainties with respect to turbulence variation along the wingspan. This measure is not always available when analysing the aircraft response in flight. In this section, the effect of this variation is quantified. This shows the impact of the uncertainties when neglecting certain components in the measure of turbulence.

In this study, the angle of attack measure in a single point is used to estimate the turbulence disturbance in three different directions. Other measures in flight are available, such as the measure of vertical load factor at each wingtip. This measure is correlated with the roll rate and its variation can be explained by control surface deflection or external turbulence variations along the wingspan.

By making the assumption that the variation along the wingspan remains in the low frequency range, it is possible to define a gust angular speed defined as $\frac{\partial w_G}{\partial y} = P_{wind}$ and represented in figure 4.22. If this input is known, its effect in roll can be calculated as $Cl = Cl_{pwind} P_{wind} \frac{l_{ref}}{V_\infty}$ with the gust derivative being equal to aircraft stability derivative in roll due to roll rate ($Cl_{pwind} = Cl_p$) as proposed in [10].

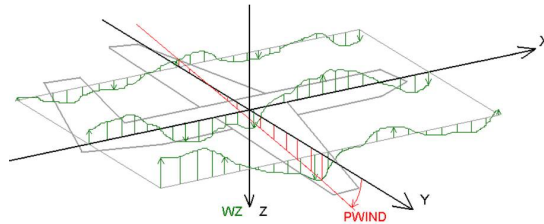


Figure 4.22: Illustration of gust angular speed induced by variations along the wingspan

The variation of this angular speed is correlated with the difference between the vertical load factor measured at both wingtips assuming that aileron or spoiler control surface are not deflected. An estimation from vertical load factor measures at the wingtip is made and the profile for a specific case is shown in figure 4.23. Control surface deflections are not shown in this analysis but its deflection need to be taken into account. In this case, the effect of turbulence variations along the wingspan and control surface deflections

impacting the response in roll (ailerons and spoilers) are mixed but zones with low control surface activity are selected. Possibilities to remove the control surface contribution could be further studied. The magnitude of the gust angular speed is scaled with respect to the amplitude ratio between the measured symmetric vertical turbulence and the vertical load factor ($\frac{wzG}{N_z}$ with $N_z = \frac{\frac{1}{2}\rho V_\infty C_{z\alpha}}{mg}$). The order of magnitude of the vertical turbulence variation at the wingtip is found to be consistent with the amplitude of the turbulence measured in a single point.

The gust angular speed is compared with the measured response in roll through the cross power spectral density, which is estimated in the same way as the power spectral density previously. Instead of comparing the measure with itself, two different measures are used to estimate the cross power spectral density which indicates the level of correlation between both signals as a function of frequency [67]. The cross power spectral density between both measures is shown in figure 4.24. A strong correlation at a frequency close to 0.5 Hz can be observed, indicating that a possible variation of turbulence along the wingspan at this frequency would explain the measured response in roll.

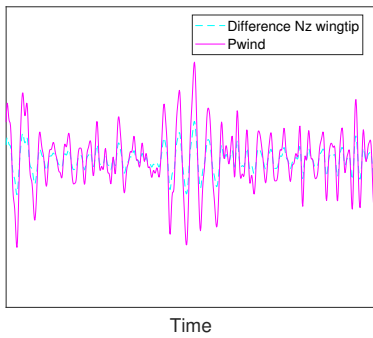


Figure 4.23: Gust angular speed in roll and difference of vertical load factor between both wingtips

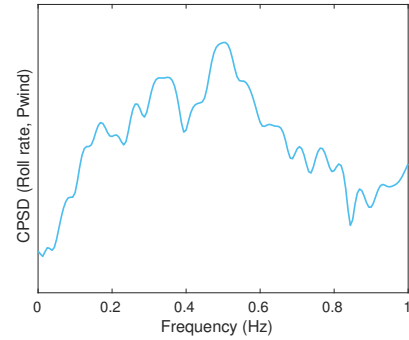


Figure 4.24: Cross-power spectral density estimate between Pwind and measured roll rate

The turbulence angular speed along the wingspan is also compared with the turbulence measured in a single point through the cross power spectral density. The coherence between both signals is also calculated through the expression $C_{xz}^2 = \frac{|\phi_{xz}^2|}{\phi_x \phi_z}$ (with ϕ_{xz} being the cross power spectral density between the measures x and z , ϕ_x and ϕ_z the power spectral density of x and z , respectively). This measure indicates the degree at which two signals (x , z) are linearly related. If a perfect linear relation exists, a value of coherence close to one is expected for all frequencies. If both signals are linearly independent or incoherent, the coherence measure would be close to zero [71].

The cross power spectral density and coherence between the gust angular speed in roll and the vertical turbulence measured in a single point are shown in figures 4.25 and 4.26,

respectively. It can be observed a coherence at different frequencies between both signals, including a component at 0.5Hz. The same analysis replacing the vertical for the lateral turbulence measure is shown in figures 4.27 and 4.28. In this case, the correlation and coherence between both signals at a frequency close to 0.5Hz can be clearly seen. This enforces the idea that a turbulence variation at this frequency would be physically feasible due to the isotropic nature of atmospheric turbulence. The same variation observed along the flight path could exist in other directions.

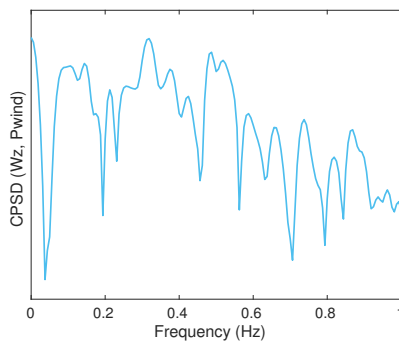


Figure 4.25: Cross-power spectral density estimate between Pwind and vertical turbulence measure

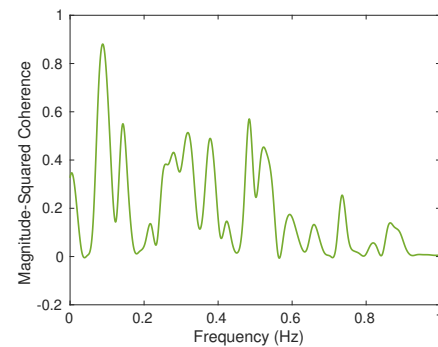


Figure 4.26: Magnitude-squared coherence estimate between Pwind and vertical turbulence measure

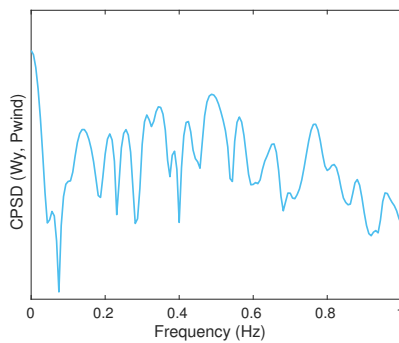


Figure 4.27: Cross-power spectral density estimate between Pwind and lateral turbulence measure

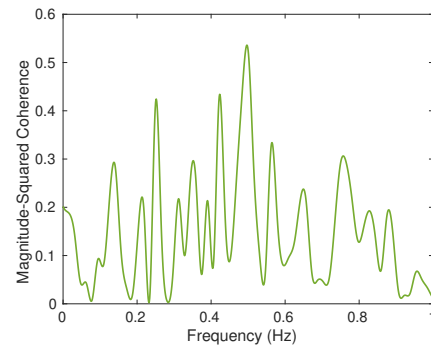


Figure 4.28: Magnitude-squared coherence estimate between Pwind and lateral turbulence measure

Figures 4.29 and 4.30 show the response in roll rate due to realistic turbulence with and without taking into account the angular gust speed in roll. The predicted response with the gust angular speed along the wingspan is closer to flight test measures both in the time and frequency domain. The response in yaw for the same time slice is also shown to illustrate the effect due to the coupling between both aircraft motions. The vertical

response is also shown in figures 4.33 and 4.34. A low impact of this uncertainty in vertical can be observed.

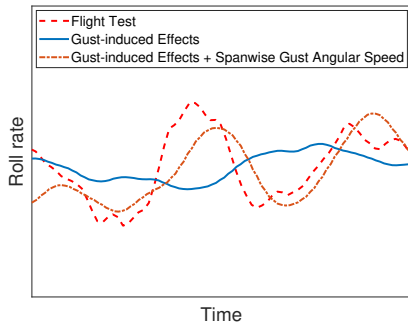


Figure 4.29: Roll rate due to turbulence

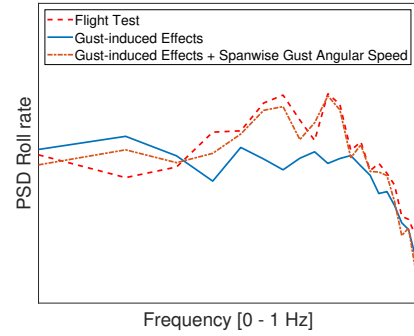


Figure 4.30: PSD roll rate due to turbulence

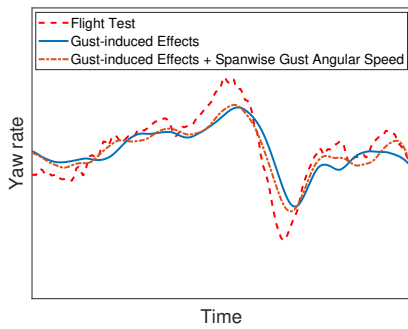


Figure 4.31: Yaw rate due to turbulence

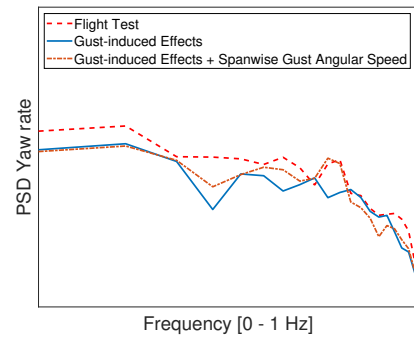


Figure 4.32: PSD yaw rate due to turbulence

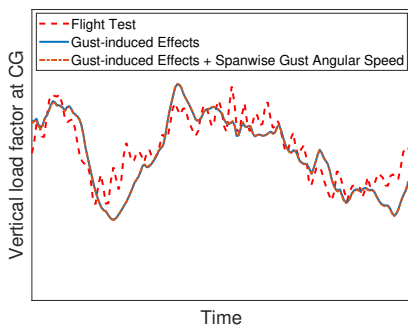


Figure 4.33: Vertical load factor at CG due to turbulence

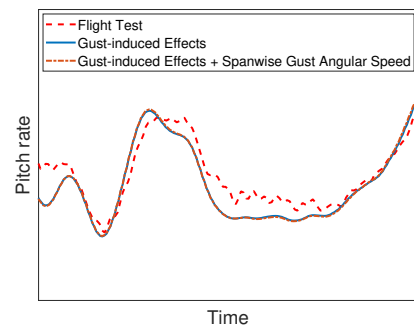


Figure 4.34: Pitch rate due to turbulence

This analysis does not intend to set a standard process to estimate the turbulence variations along the wingspan. It just shows the impact of the uncertainty associated with the variations of turbulence on the aircraft response, in particular in roll. Measurement means such as LIDAR could bring more insight in this uncertainty and different modelling possibilities could be assessed as the ones proposed in [10, 11]. Further insight in the reduction of uncertainties of the turbulence input for more accurate aircraft response predictions in roll is also recommended for future work.

Conclusions and perspectives

In this work, different possibilities to capture the aircraft response due to gust and turbulence for flight dynamics analysis are proposed, providing more accuracy in the prediction minimising the increase of computational cost. Relevant physics due to gust-induced or dynamic flexible effects are captured and included in the modelling approach. Consistency between flight dynamics investigations and gust loads calculations is possible enabling means to perform multidisciplinary analysis.

The integration between different aerodynamic models (quasi-steady and unsteady) provides a feasible solution to predict the gust and turbulence response for various vertical and lateral atmospheric disturbances. This allows for more accurate predictions in early design phases in order to evaluate and anticipate the aircraft response and flight control laws in different atmospheric conditions before flight test. This could enable flight test and lead time reductions.

Different strategies to capture the gust-induced effect are provided. Corrected DLM or CFD-LFD can be used to generate the gust-induced unsteady aerodynamic data for flight dynamics investigations in reasonable computational times. An accurate shape can be simulated in CFD and thickness and other geometrical parameters such as dihedral or wing torsion can be directly considered without corrections. Simulation results from DLM require corrections to account for geometry simplifications and other neglected physics such as viscosity. Both simulation approaches provide the gust-induced effect in the frequency domain assuming low amplitude disturbances which involves reduced computational times when comparing with nonlinear CFD simulations in the time domain. The gust-induced unsteady aerodynamic forces in the frequency domain are expressed in the time domain through a rational function approximation. Different strategies to reduce the number of states of the expression are possible such as adding an explicit delay and reducing the number of states associated with delay coefficients of the rationalisation. The approach can be adapted to additional unsteady aerodynamic modelling strategies, such as the generation of gust dynamic coefficients enabling real-time simulations. An analytical expression is also provided allowing the estimation of the effect in early design phases. Nonlinear CFD in the time domain has been used to validate the modelling approach and quantify possible limitations in the aerodynamic nonlinear region. In particular, when flying at

high Mach numbers in transonic conditions, where shock motions may appear due to gust and turbulence induced effects creating local stalls that are not captured by the proposed model.

The gust propagation effect is particularly important when simulating the aircraft response in such cases. Accurate predictions at different centre of gravity positions require an appropriate gust-induced effect including the propagation. Linearized multipoint unsteady aerodynamic models, such as the one obtained from DLM or CFD-LFD, can provide propagation along with unsteady aerodynamic effects due to the gust excitation. The phase of the response with respect to the gust input is important when using flight control laws to attenuate the aircraft response. If inaccurate responses are predicted through the models, attenuation strategies may produce the opposite effect in flight amplifying the response. Small aerodynamic nonlinear effects such as local stalls have an impact on the amplitude of the response but the phase is not impacted with respect to the input, as observed. Reducing the uncertainties with respect to the amplitude of the response is more important in order to calculate the gust loads for structural sizing. Nonlinear effects become then more relevant.

Motion-induced forces from the flexible degrees of freedom have been added to assess the impact of dynamic flexibility in the response due to vertical and lateral gust. The residualized model approach has been implemented to deal with the overlap of quasi-steady flexibility between the aeroelastic and flight dynamics models. Attenuation and low amplitude oscillations have been observed both in vertical and lateral responses by keeping a few low frequency flexible modes, reducing the overall states of the system requiring less computational time. The dynamic flexible effects have been analysed for a typical current passenger aircraft configuration. These effects and the coupling between flight dynamics and aeroelasticity become more important for more flexible configurations such as high aspect ratio wings. The residualization of the aeroelastic model assumes a certain frequency separation between rigid and flexible modes. This is satisfied for current passenger aircraft configurations but this aspect should be taken into account for more flexible designs.

The approach has also been applied to simulate the response of a generic aircraft in both theoretical and realistic atmospheric turbulent conditions. In most cases, the low frequency is more relevant than the high frequency response and dynamic flexibility can be neglected. The main physics captured is the propagation effect along the aircraft. Besides additional uncertainties such as the measured wind, comparisons of simulation results with flight test data show a good agreement in the frequency range of interest for flight dynamics investigations.

The turbulence profile is assumed to be constant along the wingspan. This has an important effect in the predicted response in roll as the variation of turbulence along the wingspan is not measured. The impact of this uncertainty in roll has been evaluated. The

estimation of this component through a gust angular speed (p_{wind}) suggests that a more accurate measure of this input would lead to more accurate predictions in the roll response.

In conclusion, this work offers the possibility to capture relevant aerodynamic effects due to gust and turbulence for different kind of flight dynamics investigations.

Perspectives

Further investigation on the topic can be focused on two main points:

- The investigation at transonic conditions show some limitations of the model to capture nonlinear unsteady effects, such as local stalls. Additional work could be focused on the possibility to capture these effects through a model based approach, as studied in [19, 21, 22]. Study of uncertainties with respect to the CFD mesh as well as turbulence modelling would be also required for accurate CFD predictions at these conditions. Experimental results from wind tunnel test can be also useful for this purpose.
- The reduction in the uncertainties of the measured turbulence input could lead to more accurate simulations. In this study, the turbulence measurements are reconstructed from angle of attack probes in a single point. The use of additional measurement techniques such as LIDAR in order to reduce the uncertainties of the turbulence input could be an option to estimate the variations of turbulence along the wingspan. The uncertainty reduction of the input could also allow evaluating the possibility to identify the gust and turbulence induced effects from flight test in order to adjust the model.

Bibliography

- [1] B. Etkin, “Turbulent Wind and Its Effect on Flight,” *Journal of Aircraft*, vol. 18, no. 5, pp. 327–345, 1981.
- [2] J. Wright and J. Cooper, *Introduction to Aircraft Aeroelasticity and Loads*. American Institute of Aeronautics and Astronautics, Inc., 2007.
- [3] European Aviation Safety Agency, “Certification Specifications for Large Aeroplanes (CS-25),” 2012.
- [4] F. M. Hoblit, *Gust Loads on Aircraft: Concepts and Applications*. AIAA Education Series, American Institute of Aeronautics and Astronautics, 1988.
- [5] B. Etkin, *Dynamics of Flight: Stability and Control*. John Wiley & Sons Australia, Limited, 1996.
- [6] E. Albano and W. P. Rodden, “A doublet-lattice method for calculating lift distributions on oscillating surfaces in subsonic flows,” *AIAA Journal*, vol. 7, no. 2, pp. 279–285, 1969.
- [7] C. Valente, Y. Lemmens, C. Wales, D. Jones, A. Gaitonde, and J. Cooper, “A Doublet-Lattice Method Correction Approach for High Fidelity Gust Loads Analysis,” *58th AIAA/ASCE/AHS/ASC Structures, Structural Dynamics, and Materials Conference*, 2017.
- [8] T. Kier, “Comparison of Unsteady Aerodynamic Modelling Methodologies with Respect to Flight Loads Analysis,” *AIAA Atmospheric Flight Mechanics Conference and Exhibit*, 2005.
- [9] T. Kier, “An Integrated Model for Lateral Gust Loads Analysis and Dutch Roll Flight Dynamics using a 3D Panel Method,” *International Forum on Aeroelasticity and Structural Dynamics (IFASD)*, 2017.
- [10] W. H. J. J. van Staveren, *Analyses of Aircraft Responses to Atmospheric Turbulence*. PhD thesis, Delft University of Technology, 2003.

-
- [11] P. A. van Gastel and W. H. J. J. van Staveren, "Aircraft responses to atmospheric turbulence. A comparative study," Tech. Rep. LR-778, Delft University of Technology, Faculty of Aerospace Engineering, 1994.
- [12] L. Reimer, M. Ritter, R. Heinrich, and W. Krüger, "CFD-based Gust Load Analysis for a Free-flying Flexible Passenger Aircraft in Comparison to a DLM-based Approach," *22nd AIAA Computational Fluid Dynamics Conference*, 2015.
- [13] R. Thormann and M. Widhalm, "Linear-Frequency-Domain Predictions of Dynamic-Response Data for Viscous Transonic Flows," *AIAA Journal*, vol. 51, no. 11, pp. 2540–2557, 2013.
- [14] M. Widhalm, A. R. Hübner, and R. Thormann, "Linear frequency domain predictions of dynamic derivatives for the DLR F12 wind tunnel model," *European Congress on Computational Methods in Applied Sciences and Engineering (ECCOMAS)*, 2012.
- [15] P. Bekemeyer and S. Timme, "Reduced Order Gust Response Simulation using Computational Fluid Dynamics," *57th AIAA/ASCE/AHS/ASC Structures, Structural Dynamics, and Materials Conference*, 2016.
- [16] P. Bekemeyer, R. Thormann, and S. Timme, "Linearised Frequency Domain Gust Analysis of Large Civil Aircraft," *European Congress on Computational Methods in Applied Sciences and Engineering (ECCOMAS)*, 2016.
- [17] W. Weigold, B. Stickan, I. Travieso-Alvarez, C. Kaiser, and P. Teufel, "Linearized Unsteady CFD for Gust Loads with TAU," *International Forum on Aeroelasticity and Structural Dynamics (IFASD)*, 2017.
- [18] P. Bekemeyer, R. Thormann, and S. Timme, "Investigation Into Gust Load Alleviation Using Computational Fluid Dynamics," *International Forum on Aeroelasticity and Structural Dynamics (IFASD)*, 2019.
- [19] R. Thormann and S. Timme, "Application of Harmonic Balance Method for Non-linear Gust Responses," *AIAA/ASCE/AHS/ASC Structures, Structural Dynamics and Materials Conference*, 2018.
- [20] M. Ripepi, *Model Order Reduction for Computational Aeroelasticity*. PhD thesis, Politecnico di Milano, 2014.
- [21] D. Quero and W. Krüger, "A Nonlinear Frequency Domain Aerodynamic Model for Continuous Turbulence Encounter based on Functional Series Expansion," *International Forum on Aeroelasticity and Structural Dynamics (IFASD)*, 2017.
- [22] P. Bekemeyer, M. Ripepi, R. Heinrich, and S. Görtz, "Nonlinear Unsteady Reduced-Order Modeling for Gust-Load Predictions," *AIAA Journal*, vol. 57, pp. 1–12, 2019.

- [23] K. L. Roger, "Airplane Math Modelling Methods for Active Control Design," *Structural Aspects of Active Control*, vol. 9, no. AGARD-CP-228, 1977.
- [24] M. Karpel, "Time-Domain Aeroservoelastic Modeling Using Weighted Unsteady Aerodynamic Forces," *Journal of Guidance, Control, and Dynamics*, vol. 13, no. 1, pp. 30–37, 1990.
- [25] P. Goggin, "A general gust and maneuver load analysis method to account for the effects of active control saturation and nonlinear aerodynamics," *AIAA Dynamics Specialists Conference*, 1992.
- [26] M. Karpel, B. Moulin, and P. C. Chen, "Dynamic Response of Aeroservoelastic Systems to Gust Excitation," *Journal of Aircraft*, vol. 42, no. 5, pp. 1264–1272, 2005.
- [27] T. Kier and G. Looye, "Unifying Manoeuvre and Gust Loads Analysis," *International Forum on Aeroelasticity and Structural Dynamics (IFASD)*, 2009.
- [28] H. G. Giessler, M. Kopf, T. Faulwasser, P. Varutti, and R. Findeisen, "Gust Load Alleviation Based on Model Predictive Control," *International Forum on Aeroelasticity and Structural Dynamics (IFASD)*, 2013.
- [29] D. Quero, P. Vuillemin, and C. Poussot-Vassal, "A Generalized State-Space Aeroservoelastic Model Based on Tangential Interpolation," *Aerospace*, vol. 6, no. 1, p. 9, 2019.
- [30] M. R. Waszak and D. K. Schmidt, "On the Flight Dynamics of Aeroelastic Vehicles," *AIAA Atmospheric Flight Mechanics Conference*, 1986.
- [31] M. R. Waszak and D. K. Schmidt, "Flight Dynamics of Aeroelastic Vehicles," *Journal of Aircraft*, vol. 25, no. 6, pp. 563–571, 1988.
- [32] C. Buttrill, P. Arbuckle, and T. Zeiler, "Nonlinear simulation of a flexible aircraft in maneuvering flight," *AIAA Flight Simulation Technologies Conference*, 1987.
- [33] M. Waszak, C. S. Buttrill, and D. Schmidt, "Modeling and Model Simplification of Aeroelastic Vehicles: An Overview," Tech. Rep. NASA-TM-107691, NASA Langley Research Center, 1992.
- [34] C. Reschke, *Integrated Flight Loads Modelling and Analysis for Flexible Transport Aircraft*. PhD thesis, TU Stuttgart, 2006.
- [35] J. Hofstee, T. Kier, C. Cerulli, and G. Looye, "A Variable, Fully Flexible Dynamic Response Tool for Special Investigations (VarLoads)," *International Forum on Aeroelasticity and Structural Dynamics (IFASD)*, 2003.

- [36] K. K. Gupta, M. J. Brenner, and L. S. Voelker, “Development of an integrated aeroservoelastic analysis program and correlation with test data,” Tech. Rep. NASA-TP-3120, NASA Dryden Flight Research Facility, 1991.
- [37] B. A. Winther, P. J. Goggin, and J. R. Dykman, “Reduced-Order Dynamic Aeroelastic Model Development and Integration with Nonlinear Simulation,” *Journal of Aircraft*, vol. 37, no. 5, pp. 833–839, 2000.
- [38] G. Looye, *An Integrated Approach to Aircraft Modelling and Flight Control Law Design*. PhD thesis, Delft University of Technology, 2008.
- [39] K. Koenig and J. Schuler, “Integral Control of Large Flexible Aircraft,” *RTO AVD Specialists Meeting on Structural Aspects of Flexible Aircraft Control*, 2000.
- [40] G. Puyou, *Conception multi-objectifs de lois de pilotage pour un avion de transport civil*. PhD thesis, École nationale supérieure de l’aéronautique et de l’espace, 2005.
- [41] C. Reschke and G. Looye, “Comparison of Model Integration Approaches for Flexible Aircraft Flight Dynamics Modelling,” *International Forum on Aeroelasticity and Structural Dynamics (IFASD)*, 2005.
- [42] P. Teufel, M. Hanel, and K. H. Well, “Integrated flight mechanic and aeroelastic modelling and control of a flexible aircraft considering multidimensional gust input,” *RTO AVD Specialists Meeting on Structural Aspects of Flexible Aircraft Control*, 2000.
- [43] D. Quero, *An Aeroelastic Reduced Order Model for Dynamic Response Prediction to Gust Encounters*. PhD thesis, Technischen Universität Berlin, 2017.
- [44] J. D. Anderson, *Computational Fluid Dynamics: The Basics with Applications*. McGraw-Hill, 1995.
- [45] U. Piomelli, “Large-eddy simulation: achievements and challenges,” *Progress in Aerospace Sciences*, vol. 35, no. 4, pp. 335–362, 1999.
- [46] B. Stickan, J. Dillinger, and G. Schewe, “Computational aeroelastic investigation of a transonic limit-cycle-oscillation experiment at a transport aircraft wing model,” *Journal of Fluids and Structures*, vol. 49, pp. 223–241, 2014.
- [47] P. Spalart and S. Allmaras, “A one-equation turbulence model for aerodynamic flows,” *AIAA 30th Aerospace Sciences Meeting and Exhibit*, 1992.
- [48] *TAU-Code User Guide*. DLR Institute of Aerodynamics and Flow Technology, 2017.
- [49] C. Kaiser, D. Quero, and J. Nitzsche, “Quantification of nonlinear effects in gust load prediction,” *International Forum on Aeroelasticity and Structural Dynamics (IFASD)*, 2019.

-
- [50] R. Heinrich and L. Reimer, “Comparison of different approaches for modeling atmospheric effects like gusts and wake-vortices in the CFD code TAU,” *International Forum on Aeroelasticity and Structural Dynamics (IFASD)*, 2017.
- [51] M. Meinel and G. O. Einarsson, “The FlowSimulator framework for massively parallel CFD applications,” *PARA: International Workshop on Applied Parallel Computing*, 2010.
- [52] N. M. Newmark, “A Method of Computation for Structural Dynamics,” *Journal of the Engineering Mechanics Division*, vol. 85, no. 3, pp. 67–94, 1959.
- [53] H. Barnewitz and B. Stickan, “Improved Mesh Deformation,” *Management and Minimisation of Uncertainties and Errors in Numerical Aerodynamics*, vol. 122, pp. 219–243, 2013.
- [54] A. Michler, “Aircraft control surface deflection using RBF-based mesh deformation,” *International Journal for Numerical Methods in Engineering*, vol. 88, pp. 986–1007, 2011.
- [55] M. Ritter, “Nonlinear Numerical Flight Dynamics of Flexible Aircraft in the Time Domain by Coupling of CFD, Flight Mechanics, and Structural Mechanics,” *Notes on Numerical Fluid Mechanics and Multidisciplinary Design*, 2013.
- [56] P. Bekemeyer, *Rapid Computational Aerodynamics for Aircraft Gust Response Analysis*. PhD thesis, University of Liverpool, 2018.
- [57] R. Dwight, *Efficiency Improvements of RANS-Based Analysis and Optimization using Implicit and Adjoint Methods on Unstructured Grids*. PhD thesis, University of Manchester, 2006.
- [58] Y. Saad and M. H. Schultz, “GMRES: A Generalized Minimal Residual Algorithm for Solving Nonsymmetric Linear Systems,” *SIAM Journal on Scientific and Statistical Computing*, vol. 7, no. 3, pp. 856–869, 1986.
- [59] M. Blair, “A Compilation of the Mathematics Leading to the Doublet Lattice Method,” Tech. Rep. WL-TR-92-3028, Air Force Wright Laboratory, 1992.
- [60] R. Stengel, *Flight Dynamics*. Princeton University Press, 2003.
- [61] B. Barriety, J. P. Boin, O. Chandre-Vila, and T. Mauermann, “Fast Fluid-Structure Computational Method Taking Into Account Non-linear Aerodynamic,” *International Forum on Aeroelasticity and Structural Dynamics (IFASD)*, 2019.
- [62] R. J. Guyan, “Reduction of stiffness and mass matrices,” *AIAA Journal*, vol. 3, no. 2, p. 380, 1965.

-
- [63] *MSC.Nastran User's Guide*. MSC.Software, 2001.
- [64] A. A. Shabana, "Flexible Multibody Dynamics: Review of Past and Recent Developments," *Journal of Multibody System Dynamics*, pp. 189–222, 1997.
- [65] C. P. Bourissou, *Performances d'un avion souple : application aux gnoptères Hales*. PhD thesis, Ecole Nationale Supérieure de l'Aéronautique et de l'Espace, Toulouse, 1999.
- [66] "MIL-F-8785C - Military Specification Flying Qualities of Piloted Airplanes," 1980.
- [67] P. Welch, "The use of fast Fourier transform for the estimation of power spectra: A method based on time averaging over short, modified periodograms," *IEEE Transactions on Audio and Electroacoustics*, vol. 15, no. 2, pp. 70–73, 1967.
- [68] E. A. F. Ringnes, "Analysis of aerodynamic coefficients using gradient data: Spanwise turbulence effects on airplane response," Tech. Rep. NASA-CR-3961, FWG Associates, Inc., 1986.
- [69] R. Kumar, "Spanwise Turbulence Effects on Airplane Response," tech. rep., Aerospace Engineering Department, University of Texas, 2016.
- [70] A. D. Carre, G. Deskos, and R. Palacios, "Realistic Turbulence Effects in Low Altitude Dynamics of Very Flexible Aircraft," *AIAA Scitech Forum*, 2020.
- [71] J. F. Johnston, "Accelerated Development and Flight Evaluation of Active Controls Concepts for Subsonic Transport Aircraft: Load Alleviation/Extended Span Development and Flight Tests," Tech. Rep. NASA-CR-159148, Lockheed-California Co., 1979.

